ION HEATING AND MHD DYNAMO FLUCTUATIONS IN THE REVERSED FIELD PINCH

by

EARL EDWARD SCIME

A thesis submitted in partial fulfillment of the
requirements for the degree of

Doctor of Philosophy
(Physics)

at the
UNIVERSITY OF WISCONSIN - MADISON
1992

ABSTRACT

Ion temperature measurements, time resolved to 10 μs, have been made in the Madison Symmetric Torus (MST) reversed field pinch (RFP) with a five channel charge exchange analyzer. The characteristic anomalously high ion temperature of RFP discharges has been observed in the MST. The evolution of the ion and electron temperature, as well as density and charge exchange power loss, were measured for a series of reproducible discharges. The ion heating expected from collisional processes with the electrons is calculated and shown too small to explain the measured ion temperatures. The charge exchange determined ion temperature is also compared to measurements of the thermally broadened CV 227.1 nm line.

The ion temperature, $T_i \approx 250$ eV for $I = 360$ kA, increases by more than 100% during discrete dynamo bursts in MST discharges. Magnetic field fluctuations in the range 0.5 - 5 MHz were also measured during the dynamo bursts. Structure in the fluctuation frequency spectrum at the ion cyclotron frequency appears as the bursts terminate, suggesting that the mechanism of ion heating involves the dissipation of dynamo fluctuations at ion cyclotron frequencies. Theoretical models for ion heating are reviewed and discussed in light of the experimental results.

Similar electron heating mechanisms may be responsible for the discrepancy between measured and expected loop voltages in the RFP. The electrons, as well as the ions, may be heated by turbulent mechanisms, and a RFP energy budget including such phenomena is described.

ACKNOWLEDGMENTS

"The heavens declare the glory of God; and the firmament sheweth his handiwork. Day unto day uttereth speech, and night until night sheweth knowledge. There is no speech nor language, where their voice is not heard. Their line is gone out through all the earth, and their words to the end of the world. In them hath he set a tabernacle for the sun. Which is as a bridegroom coming out of his chamber, and rejoiceth as a strong man to run a race. His going forth is from the end of the heaven, and his circuit unto the ends of it: and there is nothing hid from the heat thereof."

Psalms 19:1-6 KJV

First let me start by thanking some of those people whose hard work, dedication, donations of equipment and talent helped create the devices used to obtain the data for this thesis: Mike Cudzinovic, Curt Edmonds, Bill Foster, Jerry Frank, Mike Gerber, Ed Haines, Vern Herr, Paul Isley, John Laufenberg, and Tom Lovell. No modern scientist can honestly say that his work has been a solo effort. I am grateful for the additional measurements, guidance, and theoretical support I have received from Saeed Assadi, Miodrag Cekic, Daniel Den Hartog, Sam Hokin, Nathan Mattor, Paul Terry, and Christopher Watts. I would also like to thank my office mates for making graduate school endurable by injecting a little humor into a otherwise arduous affair: Brett Chapman, Jim Hollenberg, David Newman, Gene Riggs, Matt Stoneking, and Chris Watts.

On the financial side I would like to express my appreciation to Oak Ridge Associated Universities Magnetic Fusion Science Fellowship program, the Wisconsin Alumni Research Fellowship program and the College of Letters and Science (UW-Madison) for funding my graduate studies.

There are so many people that have made my career in physics possible. Through their love and support I have been able to follow my dreams, however unrealistic and improbable they seemed at the time. Thank

you Carmen Austin, Dr. Alberto Devoto, Dr. Jacob Kimel, Jim and Ellen Sizemore, my in-laws Jon and Delite Piper, and most of all, my grandmother Concetta Migliore.

Lastly, I would like to dedicate this thesis to my wife Joy. Thank you for enduring nearly five years of sub-arctic weather. I cannot promise that the weather will be warmer wherever life takes us, but we will always be together.

> *"Because that which may be known of God is manifest in them; for God hath showed it unto them. For the invisible things of him since the creation of the world are clearly seen, being understood by the things that are made, even his eternal power and Deity; so that they are without excuse"*
>
> Romans 1:19-20 KJV

Earl Scime, 1992

Inertial Ranger, N.F.D. Founder, Oids Master,
and Arena Spectre Champion

P.S. [illegible] [illegible] [illegible] !

P.P.S. The MST experiment is supported by the United States Department of Energy.

TABLE OF CONTENTS

2. APPARATUS

3. CHARGE EXCHANGE MEASUREMENTS

4. HIGH FREQUENCY MAGNETIC FLUCTUATION MEASUREMENTS

5. EQUILIBRIUM ION TEMPERATURE MEASUREMENTS

6. THE MHD DYNAMO, MAGNETIC ENERGY BALANCE AND HELICITY CONSERVATION IN THE RFP

7. FLUCTUATING ION TEMPERATURE MEASUREMENTS

CHAPTER 1

INTRODUCTION

Despite the progress in magnetic confinement fusion since the first reversed field pinch (RFP) discharge was accidently formed in the ZETA experiment in 1960,[1] many of the fundamental questions regarding reversed field pinch plasmas at that time remain unanswered today. What is the physical mechanism that produces and sustains the toroidal field (the dynamo effect)? What is the driving force behind the modest energy confinement of the reversed field pinch? Why are the ions often as hot, if not hotter, than the electrons in Ohmically heated plasmas? This thesis will attempt to answer the third question, i.e. why are the ions so hot, by presenting experimental measurements of the ion temperature in the Madison Symmetric Torus (MST) that indicate that the first and third questions are, if not identical, very closely related. These results demonstrate a clear correlation between the mechanism responsible for generating the toroidal magnetic field and ion heating in the RFP.

For some years reversed field pinch experiments with ion temperature diagnostics have reported ion temperatures clearly exceeding that which would be expected from simple collisional equilibration with the Ohmically heated electrons.[2] In fact, ion temperatures greater than electron temperatures have been observed for both majority and minority ions in many RFPs.[2,3,4] Because of the large magnetic fluctuations in the RFP,[5] on the order of a few percent, a number of researchers have proposed that somehow the energy stored in the fluctuations is transfered to the ions as the fluctuations are dissipated. Although concrete evidence for such a scenario has been sorely lacking, this basic concept has become the *de facto* explanation for ion heating in the RFP community. There has been considerable evidence that not all of the energy flowing into Ohmically heated RFP plasmas heats the electrons or is emitted as radiation.[6] The energy stored in the ions must come from the external circuit, and the required energy appears to increase when plasma conditions are altered in such a way as to *supposedly* increase the level of dynamo fluctuations (usually by modifications of the plasma edge).[6,7] No direct measurements of increases in dynamo activity due to alterations of the edge conditions in RFP plasmas have been reported.[6] The increase in dynamo activity has been *inferred* from the measured increase in ion temperatures in conjunction with theories concerning limiter-magnetic field interactions in the plasma edge.[8] Clearly this puts the metaphorical cart before the horse. The series of experiments presented in this thesis investigate the correlation between *measured* increases in dynamo activity and *measured* increases in the plasma ion temperature.

The concept of the magnetohydrodynamic (MHD) dynamo is crucial to the understanding of the RFP. The coarse features of the equilibrium of the RFP are explained by Taylor's helicity conserving, minimum energy state theory.[9] However, Taylor's theory relies on a mysterious energy loss mechanism that enables the plasma to relax to a minimum energy state. The sustainment and partial reversal of the toroidal field is also unexplained by the Taylor model; Taylor's theory only proves that the reversed field state is a minimum energy state. To explain the field sustainment, a dynamo mechanism, similar to the one proposed to explain the Earth's magnetic field,[10] is often invoked. The MHD dynamo model describes a process whereby equilibrium magnetic field can be generated via correlated magnetic and flow velocity fluctuations; the fluctuations themselves become the energy relaxation mechanism needed by Taylor's theory.[11] The basics of MHD dynamo theory are reviewed in chapter 6 of this thesis.

The toroidal flux in the MST reversed field pinch is generated in both a continuous fashion and during discrete events (Fig. 1.1).[5] The discrete flux generating events in the MST are, by definition, periods of increased dynamo activity. These dynamo events present an unparalleled opportunity for a careful examination of the correlation between ion heating and dynamo fluctuations in the RFP. In fact, analysis of the frequency spectrum of the magnetic fluctuations suggests that ion cyclotron resonances may be the physical mechanism responsible for transfering energy from the fluctuations to the ions.

This thesis is divided into eight chapters. Chapters 2 through 4 review the diagnostics used and developed for ion temperature and magnetic fluctuation measurements. Chapter 5 compares equilibrium ion temperature measurements to temperatures expected from ion-electron collisional heating. Chapter 6 is a review of MHD dynamo theory. Measurements of ion temperature and magnetic field fluctuations are presented in chapter 7.

In the concluding chapter of this thesis the ion heating experimental results are summarized. An attempt is also made to explain inconsistencies between RFP electron temperatures and measured plasma resistivities in terms of turbulent electron heating mechanisms similar to those postulated to explain the ion heating.

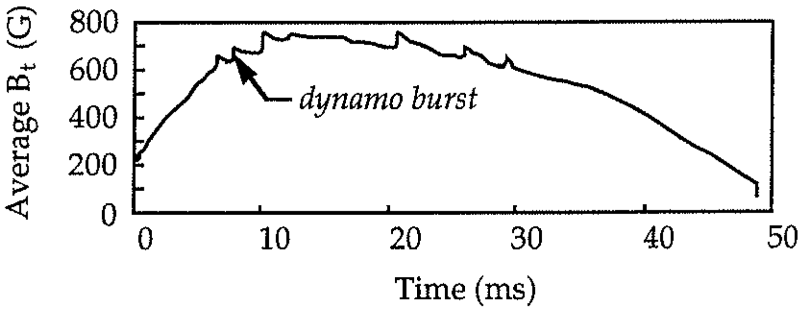

Figure 1.1 *Discrete and continuous generation of toroidal field in the MST*

References

1 M. G. Rusbridge, '*A model of field reversal in the diffuse pinch,*' Plasma Physics **19**, 499 (1977).

2 Robert B. Howell, and Yoshio Nagayama,' *Ion energy measurements on a reversed-field pinch experiment using Doppler broadening,*' Phys. Fluids **28**, 734 (1985).

3 T. Fujita, K. Saito, J. Matusi, Y. Kamada, H. Morimoto, Z. Yoshida, and N. Inoue,'*Anomalous Ion Heating in Repute-1 Ultra-Low q and Reversed Field Pinch Plasmas,*' Nucl. Fusion **31**, 3 (1991).

4 G. A. Wurden, P. G. Weber, K. F. Schoenberg, A. E. Schofield, J. A. Phillips, C. P. Munson, G. Miller, J. C. Ingraham, R. B. Howell, J. N. Downing, R. R. Chrien, T. E. Cayton, L. C. Burkhardt, R. J. Bastasz, S. E. Walker, A. M. Prezler, P. G. Carolan, and C. A. Bunting, '*Ion heating studies in the ZT-40M Reversed Field Pinch*', in Proceedings of the 15th European Conference on Controlled Fusion and Plasma Physics, Dubrovnik (European Physical Society, 1988), 533.

5 S. Hokin, et al., '*Global Confinement and Discrete Dynamo Activity in the MST Reversed Field Pinch,*' Phys. Fluids B **3**, 2241 (1991).

6 P. G. Carolan, A. R. Field, A. Lazaros, M. G. Rusbridge, H. Y. W. Tsui, and M. V. Bevir, in Proceedings of the 14th European Conference on Controlled Fusion and Plasma Physics, Madrid (European Physical Society, 1987) vol. II, 469.

7 Kurt F. Schoenberg, Ron W. Moses Jr., and Randy L. Hagenson,'*Plasma resistivity in the presence of a reversed-field pinch dynamo,*' Phys. Fluids **27**, 1671 (1984).

8 B. Alper, H. A. Bodin, C. A. Bunting, P. G. Carolan, J. Cunnane, D. E. Evans, A. R. Field, R. J. Hayden, A. Lazaros, A. A. Newton, P. G. Noonan, A. Patel, H. Y. W. Tsui and P. D. Wilcock, '*Improved confinement in HBTX with removal of tile limiters,*' Plasma Phys. and Contr. Nucl. Fusion **30**, 843 (1988).

9 J. B. Taylor, '*Relaxation of Toroidal Plasma and Generation of Reverse Magnetic Fields,*' Phys. Rev. Lett. **33**, 1139 (1974).

10 David Rittenhouse Inglis, '*Dynamo theory of the earth's varying magnetic field,*' Rev. Mod. Physics **53**, 481 (1981).

11 J. B. Taylor, '*Relaxation and magnetic reconnection in plasmas,*' Rev. Mod. Phys. **58**, 741 (1986).

CHAPTER 2

APPARATUS

2.1 The Madison Symmetric Torus.

The temperature and fluctuation measurements discussed in this thesis were performed on the University of Wisconsin's Madison Symmetric Torus (MST). The MST is a modern, large, toroidal confinement device that is typically operated in a reversed field pinch configuration. The MST has been described in considerable detail elsewhere[1,2,3,4] and only those features of the MST that have a direct bearing on the ion temperature and magnetic fluctuation measurements will be examined here.

The MST is a 1.5 meter major radius, .52 meter minor radius, toroidal confinement device (Fig. 2.1.1). The plasma is the secondary winding of a 2.0 volt-second transformer, and a thick conducting shell provides passive equilibrium control and stability. A novel feature of the MST is that the shell is both the vacuum vessel and a single turn toroidal field coil (Fig. 2.1.2). This results in a very low ripple toroidal field;[1] however, it may also be responsible for the dramatic changes in toroidal flux, hereafter called dynamo bursts, that occur throughout reversed field pinch discharges in the MST (Fig. 2.1.3). When run as a RFP, the toroidal field in MST is almost entirely self-generated. Losses of toroidal flux must be replaced by the internal dynamo mechanism and the dramatic increases in toroidal flux are indicative of sharp increases in the level of dynamo activity. The non-zero resistance and inductance of the toroidal field circuit prevents the shell from responding quickly enough to act as a perfect flux conserver, which would suppress rapid toroidal flux changes. Changes in the external circuit impedance may affect the level of internal dynamo activity by altering the amount of toroidal flux lost during the discharge.[5] Other RFP's: ZT-40M,[6] Repute-1,[7] Eta-Beta II,[8] and HBTX[9] have reported cyclic fluctuations in reversal and pinch parameters (F and Θ), but only the oscillations reported by ZT-40M during high pinch parameter operation are similar to the distinct bursts of dynamo activity in the MST.[10]

A thick conducting shell or a vertical magnetic field is needed to maintain a RFP plasma in MHD equilibrium.[11] A thick conducting shell is also required for MHD stability.[11] To minimize field errors the MST was designed with very small access ports and the vacuum pumping is carried out

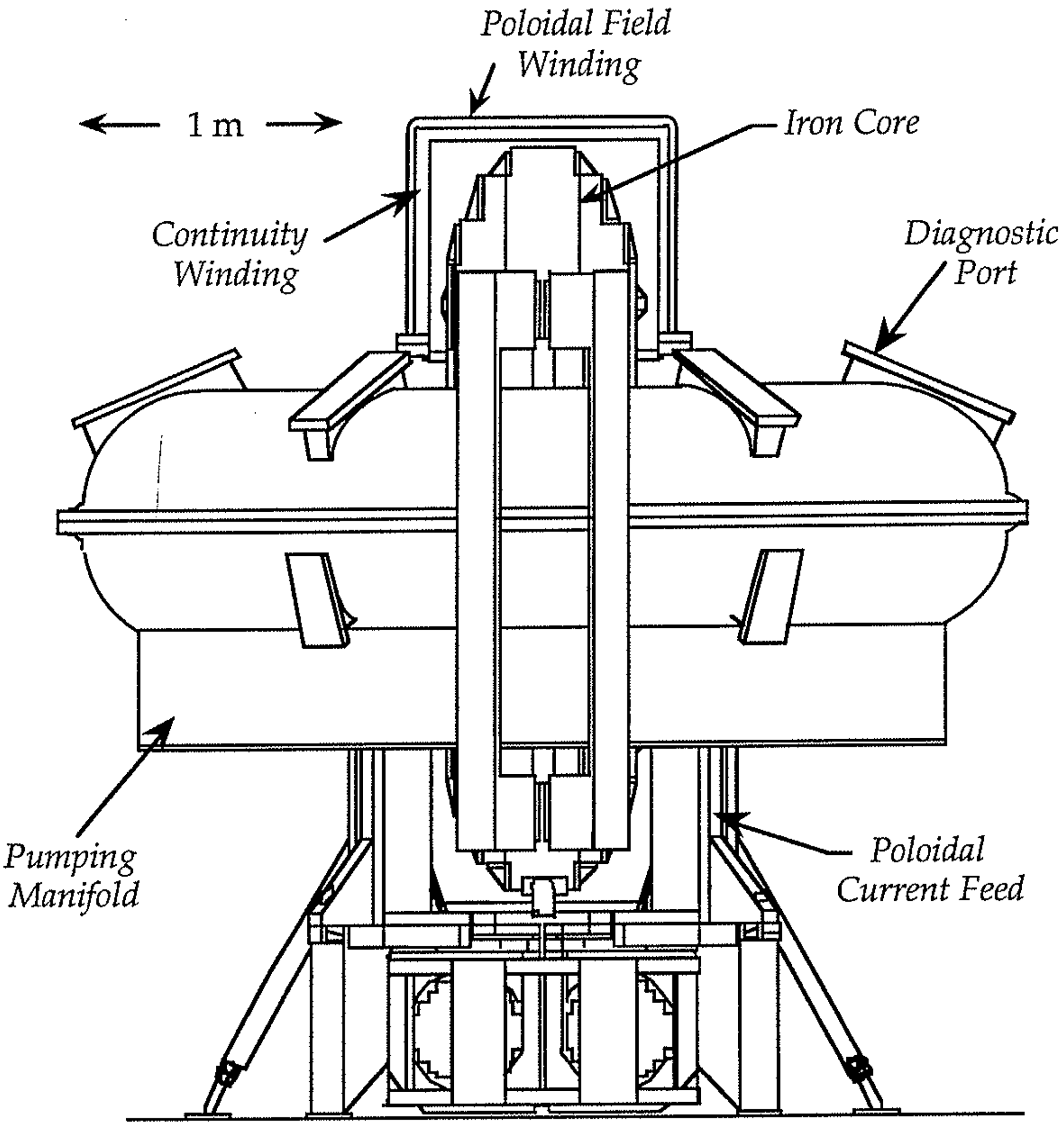

Figure 2.1.1 *The Madison Symmetric Torus*

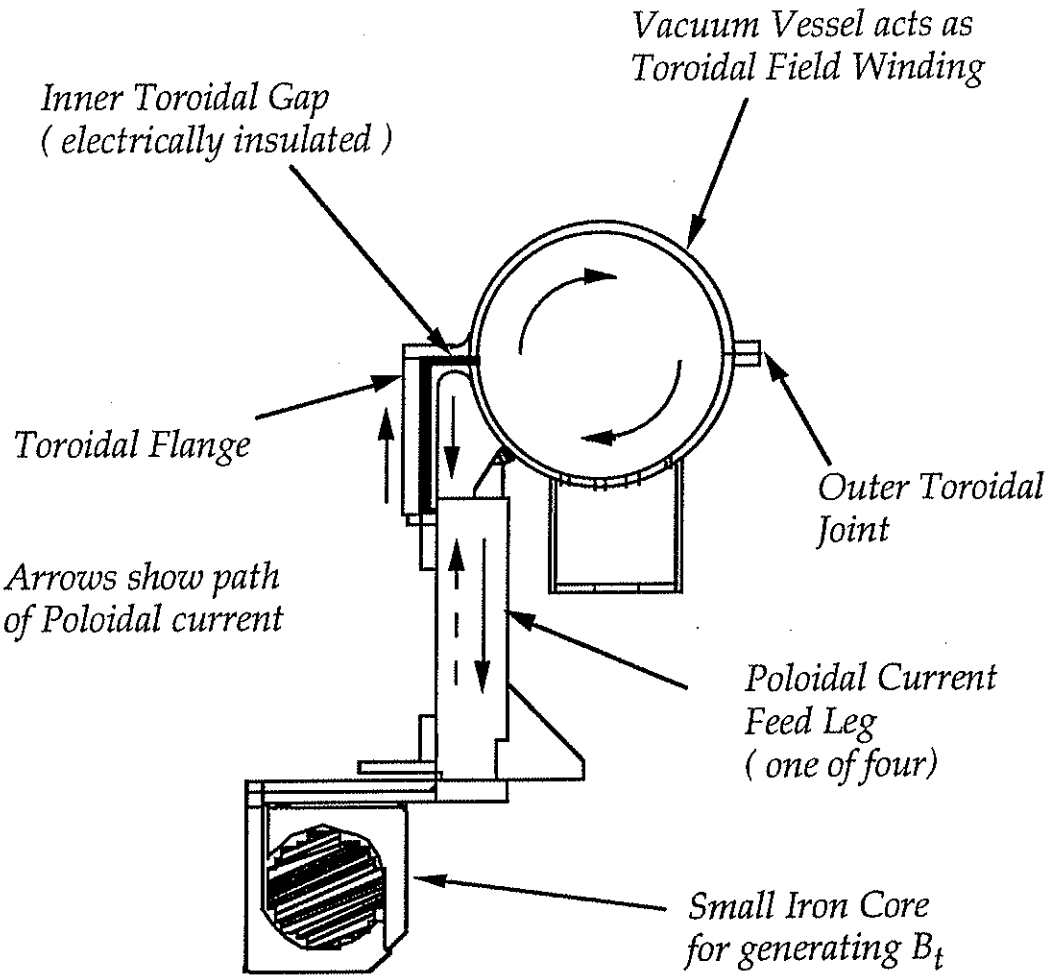

Figure 2.1.2 *The MST toroidal field circuit*

through 175 1.5″ holes in the base of the vacuum vessel. The small portholes hamper attempts to measure profiles with line of sight diagnostics, a technical difficulty that constrained the design of the five channel charge exchange analyzer.

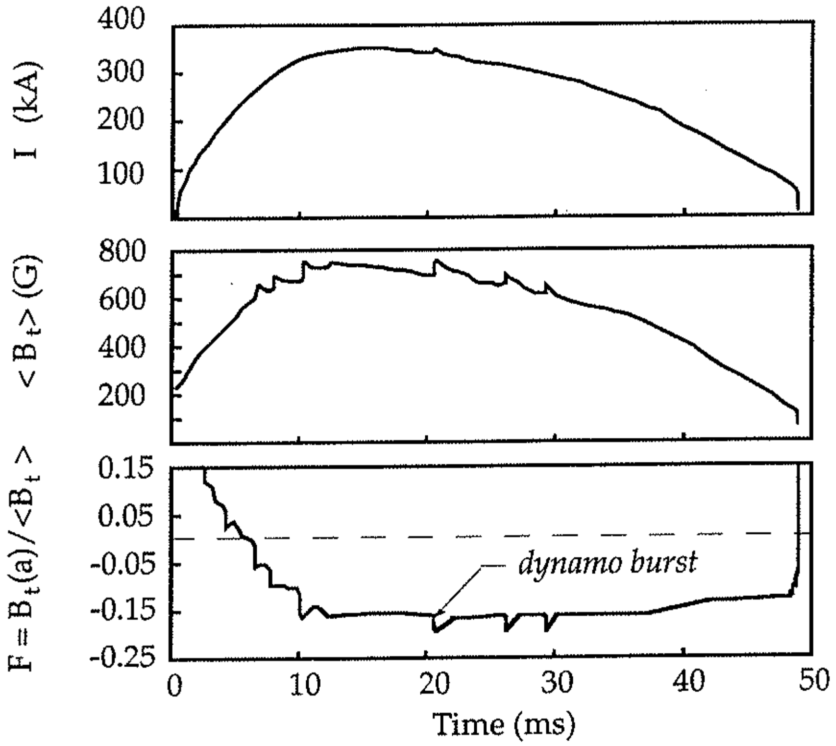

Figure 2.1.3 *Dynamo bursts during a MST discharge*

2.2 MST Diagnostics.

The principle diagnostics used for the experiments described in this thesis were a five channel charge exchange analyzer and a high frequency magnetic fluctuation probe. Before the five channel analyzer was constructed, a single channel charge exchange analyzer built in the 1960's was reconditioned and used for ion temperature measurements on the MST. Both of the charge exchange analyzers are discussed at length in chapter 3 and the magnetic probe is discussed in chapter 4. Additional diagnostics also used for these experiments included: a Thomson scattering diagnostic, a seven-channel vacuum ultraviolet spectrometer, conventional flux and Rogowski loops, and a two color laser interferometer.

Electron temperatures in MST were measured with a Thomson scattering diagnostic consisting of a 10J, Q-switched ruby laser and a Cross-Czerny-Turner spectrometer coupled to a multichannel plate.[3] The single pulse laser's firing time was varied on a shot-to-shot basis to determine the evolution of the electron temperature during a series of reproducible discharges.

Doppler ion temperatures were measured with a seven channel vacuum ultraviolet spectrometer, originally used on ZT-40M, tuned to the 227.1 nm CV line. The Doppler ion temperature measurements provided a quantitative benchmark for comparison with the charge exchange ion temperatures. However, the charge exchange ion temperature is a core temperature and measurements of CV X-ray lines indicate that the region of CV emission may extend well beyond the plasma core.[12] For descriptions of Rogowski and flux loops see reference 13.

Probably the greatest disappointment during these experiments was the lack of a consistent density diagnostic. What little density information that was available was obtained with a two color laser interferometer on loan from the Isituto Gas Ionizzati in Padova, Italy[14] and a recently constructed far-infrared interferometer.[15]

A compilation of the typical plasma parameters obtained during these experiments is given in Table 2.2.1.

Parameter	Value
Plasma Current (kAmp)	350
Loop Voltage (Volts)	15
Central Electron Temperature (eV)	325
Central Ion Temperature (eV) -- CXA	300
Central Electron Density (cm^{-3})	$\sim 1 \times 10^{13}$
Energy Confinement Time (msec) -- estim.	≤ 1.0
Plasma Duration (msec)	60

Table 2.2.1 *Typical plasma parameters for the experiments of chapters 5 and 7.*

References

[1] R. N. Dexter, D. W. Kerst, T. W. Lovell, S. C. Prager and J. C. Sprott, *'The Madison Symmetric Torus,'* Fusion Tech. **19**, 131 (1991).

[2] A. F. Alamgri, *'The Effects of Magnetic Field Errors on Reversed Field Pinch Plasmas,'* Ph.D. Thesis, University of Wisconsin-Madison (1990).

[3] D. J. Den Hartog, *'An Energy Confinement Study of the MST Reversed Field Pinch using a Thomson Scattering Diagnostic,'* Ph. D. Thesis, University of Wisconsin-Madison (1989).

[4] J. A. Beckstead, *'Sawteeth in the MST Reversed Field Pinch,'* Ph. D. Thesis, University of Wisconsin-Madison (1990).

[5] John Sarff, private communication.

[6] G. A. Wurden, et. al., *'Ion heating studies in the ZT-40M Reversed Field Pinch'*, in Proceedings of the 15th European Conference on Controlled Fusion and Plasma Physics, Dubrovnik (European Physical Society, 1988), 533.

[7] A. Fujisawa, H. Ji, K. Yamagishi, S. Shinohara, H. Toyama, K. Miyamoto, *'Anomalous Ion Temperature and Plasma Resistance due to MHD Fluctuations in Repute-1 Reversed Field Pinch Plasmas,'* Nucl.. Fusion **31**, 1443 (1991).

[8] M. Giubbilei, P. Martin, and S. Ortolani, *'A Mechanism for Plasma Heating in Driven Relaxing Magnetic Field Configurations,'* Plasma Phys. and Contr. Fusion **32**, 405 (1990).

[9] P. G. Carolan, A. R. Field, A. Lazaros, M. G. Rusbridge, H. Y. Tsui and M. K. Bevir, *'Power Balance of Ions in the HBTX Reversed Field Pinch,'* in Proceedings of the 14th European Conference on Controlled Fusion and Plasma Physics, Madrid (European Physical Society, 1987), vol. II, 469.

[10] R. A. Nebel, K. A. Werley, and M. M. Pickrell, Los Alamos National Laboratory Report LA-10653-MS (1986).

[11] H. Bodin and A. Newton, *'Reversed-Field Pinch Research,'* Nucl. Fusion **20**, 1255 (1980).

[12] Samuel Hokin, private communication.

[13] I. H. Hutchinson, Principles of Plasma Diagnostics (Cambridge Univeristy Press, Cambridge 1987).

[14] P. Innocente, S. Martini, A. Schio, Ch. Ferrer Roca, Rev. Sci. Instr. **61**, 2885 (1990).

[15] S. R. Burns, W. A. Peebles, D. Holly, T. Lovell, *'Madison Symmetric Torus Far-Infrared Interferometer,'* to be published in Rev. Sci. Instrum. October (1992).

CHAPTER 3

CHARGE EXCHANGE MEASUREMENTS IN THE MST

3.1 Neutral flux measurements

The first ion temperature measurements made on the MST utilized a reconditioned single channel charge exchange analyzer (SCCXA) that was built in the 1960's. The original designers of the SCCXA combined a 127° curved plate electrostatic energy spectrometer with a Daly[1] current amplifier to create a rugged, high gain neutral flux detector.[2,3,4] Before examining the specifics of the SCCXA design, the fundamentals of charge exchange analysis are worth reviewing.

In a plasma, a population of neutral atoms can coexist with the hot ions and electrons. The relative density of this neutral component is a strong function of electron and ion temperature, as well as electron and ion density. In the MST, cold neutral hydrogen atoms exist in abundance at the edge of the plasma. Typically these neutral atoms are created by the dissociation of the molecular hydrogen fueling gas via collisions with energetic electrons:

$$H_2 + e \rightarrow H^* + p + 2e.$$

Little energy is transferred in the collision, and the Franck-Condon neutral hydrogen atom is born with most of the 4 eV binding energy of the hydrogen molecule. The neutral then travels through the hot plasma with some small probability of reaching the core of the plasma without being ionized. To calculate the fraction of neutrals reaching the core, complete density and temperatures profiles are needed. Apart from measurements of the H_α emission profile,[5] little profile information for the MST is available. Simulations of the neutral transport have had to rely on theoretical profiles fixed by single point temperature and density measurements at the core and edge, and by line integrated density measurements (Fig. 3.1.1).

Once a neutral atom enters the plasma, it can undergo a charge exchanging collision with a hot ion. The electron from the neutral is transferred to the ion and the resulting neutral atom can traverse the plasma unaffected by electric or magnetic fields. The dominant mechanism for conversion of the neutral back into an ion is charge exchange (Fig. 3.1.2). Because of a smaller cross section and a larger mean free path, the probability

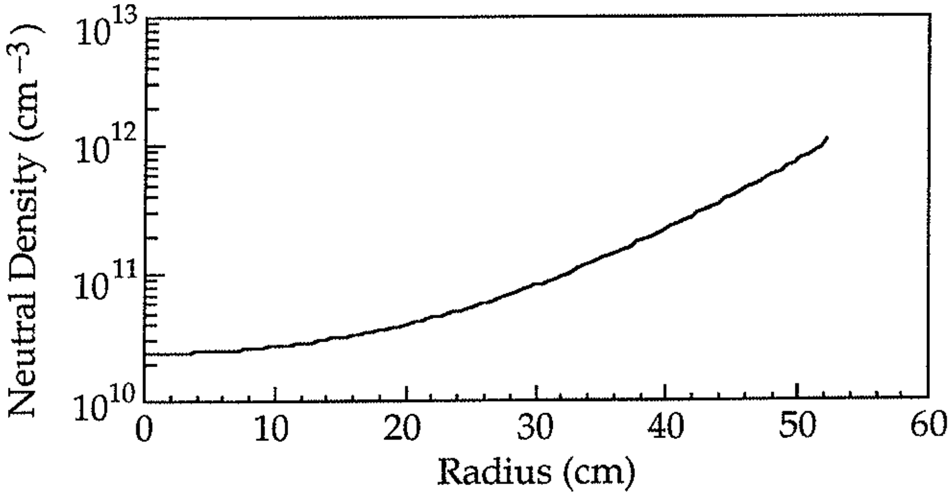

Figure 3.1.1 *Neutral density profile for MST as calculated by the neutral transport code NEUCG* [8,9] *using parabolic profiles for density and temperature.*

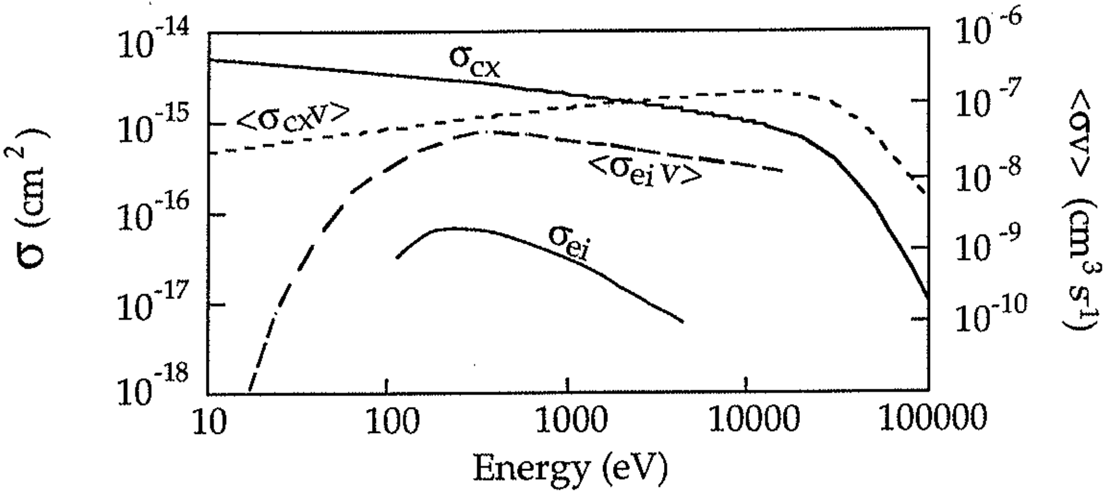

Figure 3.1.2 *Measured charge exchange,* σ_{cx}, *and electron impact ionization,* σ_{ei} *cross sections and production rates for protons on neutral hydrogen assuming a thermal distribution of ion velocities and cold neutrals.*[6] σ_{ei} *and* $<\sigma_{ei}v>$ *are plotted versus relative neutral and electron velocity (energy). The contribution of proton impact ionization to neutral ionization is negligible and charge exchange is the dominant process over the energy range shown.*[6]

of ionizing an energetic neutral decreases with increasing neutral energy. Thus an energetic neutral can often emerge from the plasma. The plasma's opacity does increase at higher densities and then only a fraction of the energetic neutrals can escape. Armed with a method of detecting energetic neutrals and measurements of the cross sections for charge exchange[7] (Fig. 3.1.2), an observer can determine a great deal about the ion energy distribution of a hot plasma. This is the *essence* of charge exchange analysis.

The isotropically emitted neutral rate [#/s] of energy E in the energy interval dE collected by a detector subtending the solid angle Ω_s at the plasma surface (Fig. 3.1.3) is given by[7]

$$F(E)dE = v^2 dv\, \Omega_s \int \exp\left[-\int_z^a \alpha(l)dl\right] S(\vec{x},\vec{v})\, d^3\vec{x} \ ,$$

where

$$\exp\left[-\int_z^a \alpha(l)dl\right]$$

is the probability that a neutral atom at position $\vec{x}$ in the interior travels along the detector's line of sight to the edge without undergoing a collision and

$$\alpha = \frac{1}{v}\left[\langle \sigma_{ei} v_e \rangle_v n_e + \left(\langle \sigma_{pi} v_i \rangle_v + \langle \sigma_{cx} v_i \rangle_v \right) n_i \right]$$

is the attenuation coefficient for the neutrals. σ_{ei}, σ_{pi}, and σ_{cx} are, respectively, the electron ionization, proton ionization, and charge exchange cross sections. $S(\vec{x},\vec{v})d\vec{v}$ is the total birth rate of neutrals of velocity $\vec{v}$ in the velocity element $d\vec{v}$ at a position $\vec{x}$. Although S includes recombination, charge exchange is the dominant process at typical MST plasma densities and temperatures.

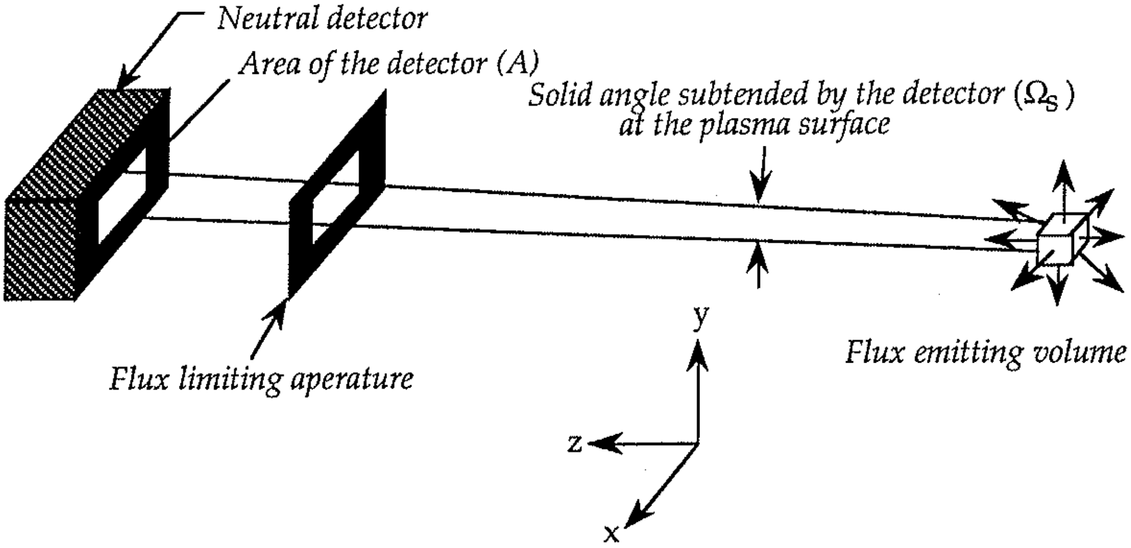

Figure 3.1.3 *View of the plasma obtained with a neutral flux detector.*

The production rate [#/s] of energetic neutral hydrogen atoms due to collisions between the neutral distribution, $f_H(\vec{x},\vec{v}_H)$, and an ion moving with velocity $\vec{v}_i$ is[7]

$$\text{production rate} = \int \sigma_{cx}(|\vec{v}_H - \vec{v}_i|)|\vec{v}_H - \vec{v}_i| f_H(\vec{x},\vec{v}_H)\, d^3\vec{v}_H \,.$$

The total birth rate of neutrals of velocity $\vec{v}$ at a position $\vec{x}$ is the product of the production rate and the ion distribution at that position. Ignoring recombination,[7]

$$S(\vec{x},\vec{v}_i) = f_i(\vec{x},\vec{v}_i) \int \sigma_{cx}(|\vec{v}_H-\vec{v}_i|)\,|\vec{v}_H-\vec{v}_i|\, f_H(\vec{x},\vec{v}_H)\, d^3\vec{v}_H.$$

where f_i is the ion distribution function and the energetic neutrals are created at the same energy as the ion, $v = v_i$. If recombination is unimportant, the initial Franck-Condon (edge molecular dissociation) neutral velocity distribution is only modified by the collisional interaction of the neutrals with the background plasma ions. Because of the complex interactions within the plasma, the resulting neutral distribution is difficult, if not impossible, to calculate. However, if the original neutral before the charge exchange collision is much less energetic than the ion, the specifics of the neutral velocity distribution can be ignored and S approximated:

$$\left|\vec{v}_H - \vec{v}_i\right| \approx v_i = v$$

$$S(\vec{x},\vec{v}) \approx f_i(\vec{x},\vec{v})\ \sigma_{cx}(v)\ v \int f_H(\vec{x},\vec{v}_H)\ d^3\vec{v}_H.$$

The remaining integral is just the first moment of the neutral distribution function, the neutral density,

$$S(\vec{x},\vec{v}) \approx f_i(\vec{x},\vec{v})\ \sigma_{cx}(v)\ v\ n_H(\vec{x}).$$

The neutral flux can then be written as,

$$F(E)dE \approx v^2 dv \Omega_s[\sigma_{cx}(E)v(E)] \int \exp[-\int_z^a \alpha(l)dl] n_H(\vec{x}) f_i(\vec{x},\vec{v})\ d^3\vec{x}\ .$$

The extent of the spatial integration is determined by the volume of the plasma viewed by the neutral flux detector. Using the coordinate system of figure 3.1.3, the volume is bounded in the $\hat{x}$ and $\hat{y}$ directions by the collimation of the detector and by the extent of the plasma (-a to a in a toroidal device) in the $\hat{z}$ direction. Assuming uniform flux emission in the portion of the xy plane viewed by the detector, the neutral flux integral becomes,

$$F(E)dE \approx v^2 dv (\Delta x \Delta y) \Omega_s[\sigma_{cx}(E)v] \left\{ \int_{-a}^{a} \exp[-\int_z^a \alpha(l)dl]\ n_H(z) f_i(z,\vec{v})\ dz \right\}.$$

Assuming the ion distribution is Maxwellian,

$$f_i(z, v_i) = n_i(z)\left(\frac{m_i}{2\pi T(z)}\right)^{3/2} \exp\left(-\frac{E}{T(z)}\right)\ ,$$

the maximum contribution to the spatial integral (last term in brackets) can be determined by differentiating the integrand with respect to z and setting the result to zero,

$$\alpha + \frac{n_H'}{n_H} + \frac{n_i'}{n_i} - \frac{3T'}{2T} + \frac{ET'}{T^2} = 0 \, .$$

For neutral flux measured at energies such that $E \gg T$, the maximum of the integrand along the line of sight (along $\hat{x}$) occurs at $T'=0$ (where T is a maximum). For parabolic electron temperature and plasma density profiles, a theoretical neutral density profile was self-consistently calculated with the neutral transport code NEUCG.[8,9] The radial profile of the resultant spatial integrand for a ***specific energy*** is shown in figure 3.1.4. The integrand is peaked where the ion temperature is a maximum.

The source profile is different for different neutral energies. For very large energies, $E \gg T$, it becomes more peaked. For low energies, it is quite broad. It might seem that unless the neutral flux is measured at extremely large energies, it is impossible to use a single approximation of the spatial integral for different energy fluxes. Fortunately, a broad, low energy source profile does not necessarily correspond to a large emitted flux. The attenuation, re-ionization, of low energy neutral flux is much larger than for high energy flux (Fig. 3.1.2). The combination of these two effects permits a single approximation of the spatial integral for moderate to high energy neutral flux.

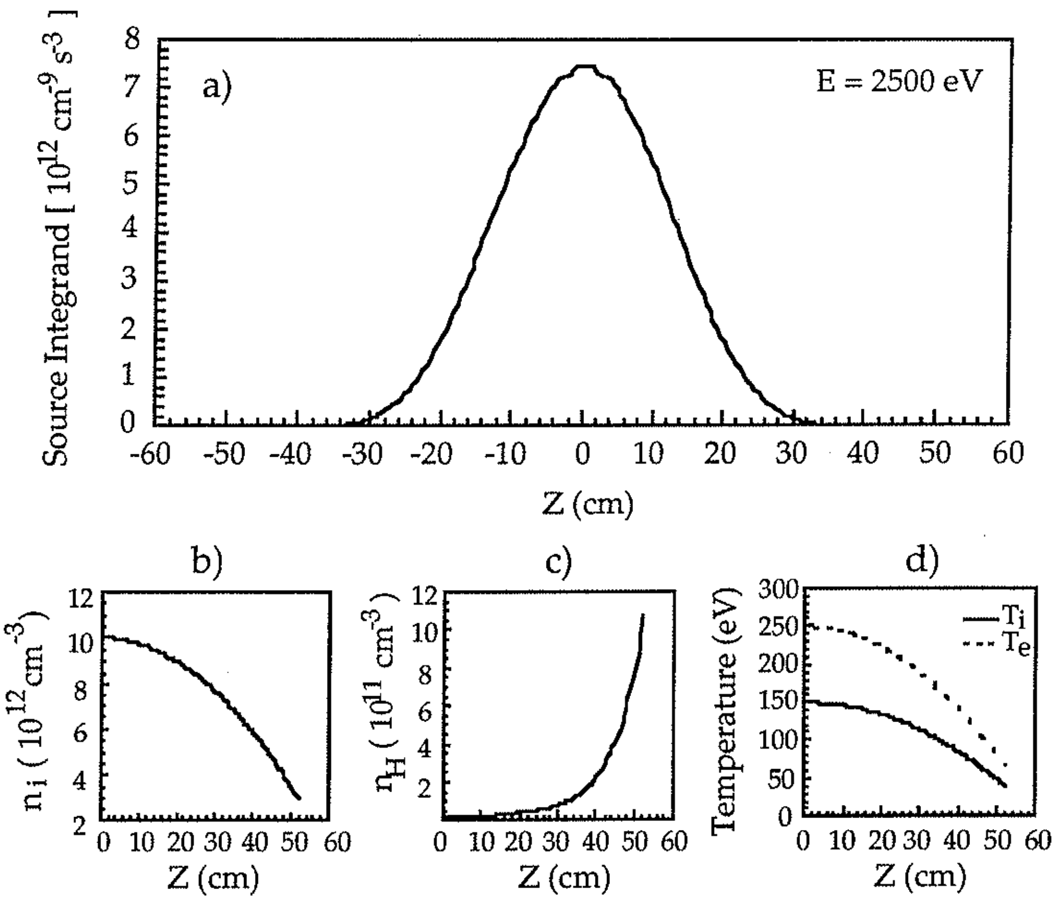

Figure 3.1.4 *a) Spatial integrand for 2500 eV neutral flux. b) Ion and electron density profile used to obtain spatial integrand. c) Neutral density profile. d) Ion and electron temperature profiles.*

Using the ***assumed*** parabolic profiles, the spatial integral for all energy neutrals is approximated by a single characteristic width times the central value throughout this thesis. Letting A = ΔxΔy, and changing variables the neutral flux equation becomes

$$F(E)dE \approx \xi A \Omega_s \sigma_{cx} E \, dE \left(\frac{n_H(z^*)\, n_i(z^*)}{\sqrt{2m_i}(\pi T(z^*))^{3/2}} \right) \exp\left(-\frac{E}{T(z^*)}\right) \exp\left[-\int_{z^*}^{a} \alpha(l)dl\right],$$

where z* = point of maximum temperature along line of sight and ξ is the characteristic width of the spatial integrand (ξ = 38 ± 10 cm for these particular ***assumed*** profiles).

For low density plasmas,

$$\int_{-a}^{a} n_i dl \leq 10^{19}\ \mathrm{m}^{-2}\ ,$$

the attenuation term is nearly unity; giving:

$$\frac{F(E)}{A\Omega_s \xi \sigma_{cx}(E)E} \approx \left(\frac{n_H(z^*)\, n_i(z^*)}{\sqrt{2m_i}(\pi T(z^*))^{3/2}}\right) \exp\left(-\frac{E}{T(z^*)}\right) . \qquad (3.1.1)$$

and the ion temperature can be determined from the inverse slope of a logarithmic plot of the corrected flux

$$\ln\left(\frac{F(E)}{A\Omega_s \xi \sigma_{cx}(E)E}\right) = \ln\left(\frac{n_H(z^*)\, n_i(z^*)}{\sqrt{2m_i}(\pi T(z^*))^{3/2}}\right) - \frac{E}{T(z^*)} .$$

The central temperature of a MST plasma with parabolic density and temperature profiles determined from the slope of the neutral flux spectrum at a particular energy is displayed in figure 3.1.5. These results include the full source profile integral and attenuation effects. The true central ion temperature for the case shown in figure 3.15 is 150 eV. At neutral energies of 2000 eV the weighting of lower energy neutral flux by the broad source profile causes the simple temperature calculation to underestimate the central ion temperature by 10-20%.

For the ion temperature fluctuation measurements of chapter 7, the possibility of profile induced changes in the calculated ion temperature is a critical question. To affect the calculated ion temperature by more than 20% while keeping the central ion temperature fixed requires substantial changes in the plasma density and density profile. The simulation results indicate that to change the calculated ion temperature by 30% requires a change in the line averaged plasma density, $<\bar{n}_e>$ of more than 100%. The measured fluctuations of $<\bar{n}_e>$ are less than 30% and the ion temperature fluctuations often exceed 100%.[10,11]

In summary, the simple approximation of the source profile integral yields reasonably accurate measurements of the central ion temperature and is sufficiently insensitive to profile effects. The energy dependence of the source profile width, ξ, results in a slight underestimation of the true central ion temperature.

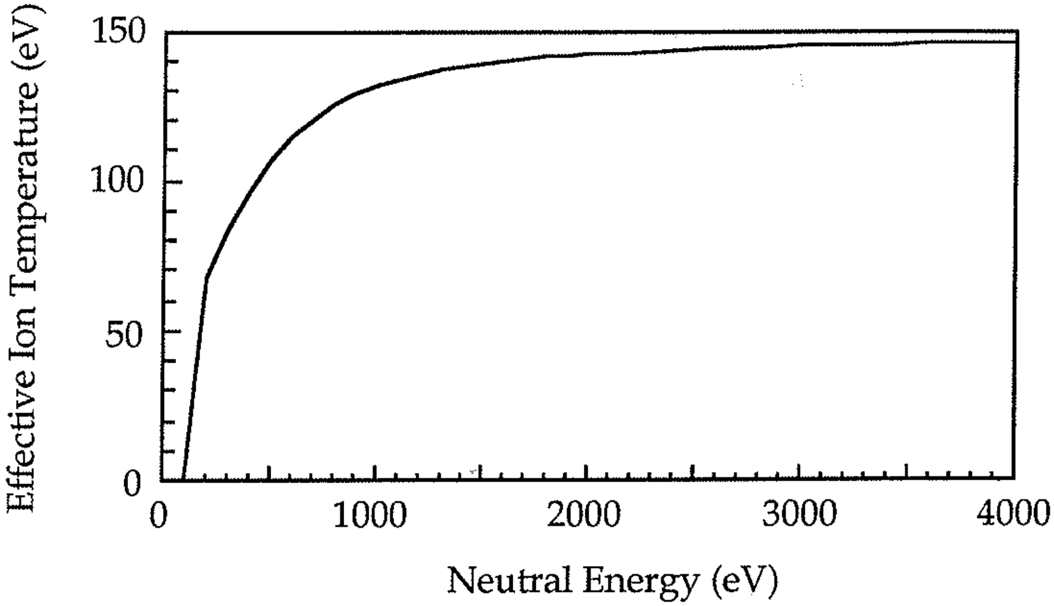

Figure 3.1.5 *Ion temperature calculated from slope of log plot of corrected flux at a particular neutral energy. Actual central ion temperature is 150 eV, so the simple calculation slightly underestimates the central ion temperature. Results are from the NEUCG*[8,9] *neutral transport code.*

3.2 The single channel charge exchange analyzer.

As with most charge exchange analyzers, the SCCXA measured the neutral hydrogen flux by first converting it into an ion flux. The neutral atoms from the plasma passed through a nitrogen filled stripping cell, where a fraction of the neutrals were converted into ions (Fig. 3.2.1). In the case of the SCCXA, the ionized neutrals then entered a $\pi/\sqrt{2}$ (~ 127.28°) pair of curved conducting plates. The potential between the plates has a logarithmic dependence,

$$\phi(r) \sim -\Delta V \ln(r) ,$$

creating a r^{-1} electric field

$$\mathcal{E}(r) = \frac{(V_1 - V_2)}{r \ln\left(\frac{R_2}{R_1}\right)} \quad .$$

The transmission condition for ions of energy E is found by balancing the centripetal and electric forces

$$q\mathcal{E}(R_0) = m\frac{v_0^2}{R_0} \quad ,$$

which gives

$$E = q(V_1 - V_2)\left(\frac{1}{2\ln\left(\frac{R_2}{R_1}\right)}\right) .$$

Ideally, the ions should enter the analyzer along an equipotential surface at the same potential as the entrance slit. If the slit is at a different potential the potential gradient near the slit will begin deflecting the incident ions as they enter the analyzer. In the SCCXA the entrance slit was at ground, and therefore an equipotential surface of V=0 midway between the plates was required. Balancing the applied voltages by placing ± ΔV/2 on each plate does not necessarily produce V=0 along the geometric center of the analyzer. The logarithmic dependence of the potential requires

$$V_{outer} = V_{inner} \ln\frac{R_1}{R_2}$$

to center the V=0 surface between the plates. Using SCCXA parameters this equation becomes $V_{outer} = -.94\ V_{inner}$. For a total potential difference of V, no significant problems were observed when $V_{outer} = -V_{inner} = \Delta V/2$ was used and the ions were injected along the centerline (Fig. 3.2.2). First order focusing is obtained for a 127° deflection[12,13] and to first order, the energy resolution of the 127° configuration is[14]

$$\frac{\Delta E}{E} \approx \frac{w}{R_0} ,$$

for $w \ll \Delta R$; w is the average of the entrance and exit slit radial extent.

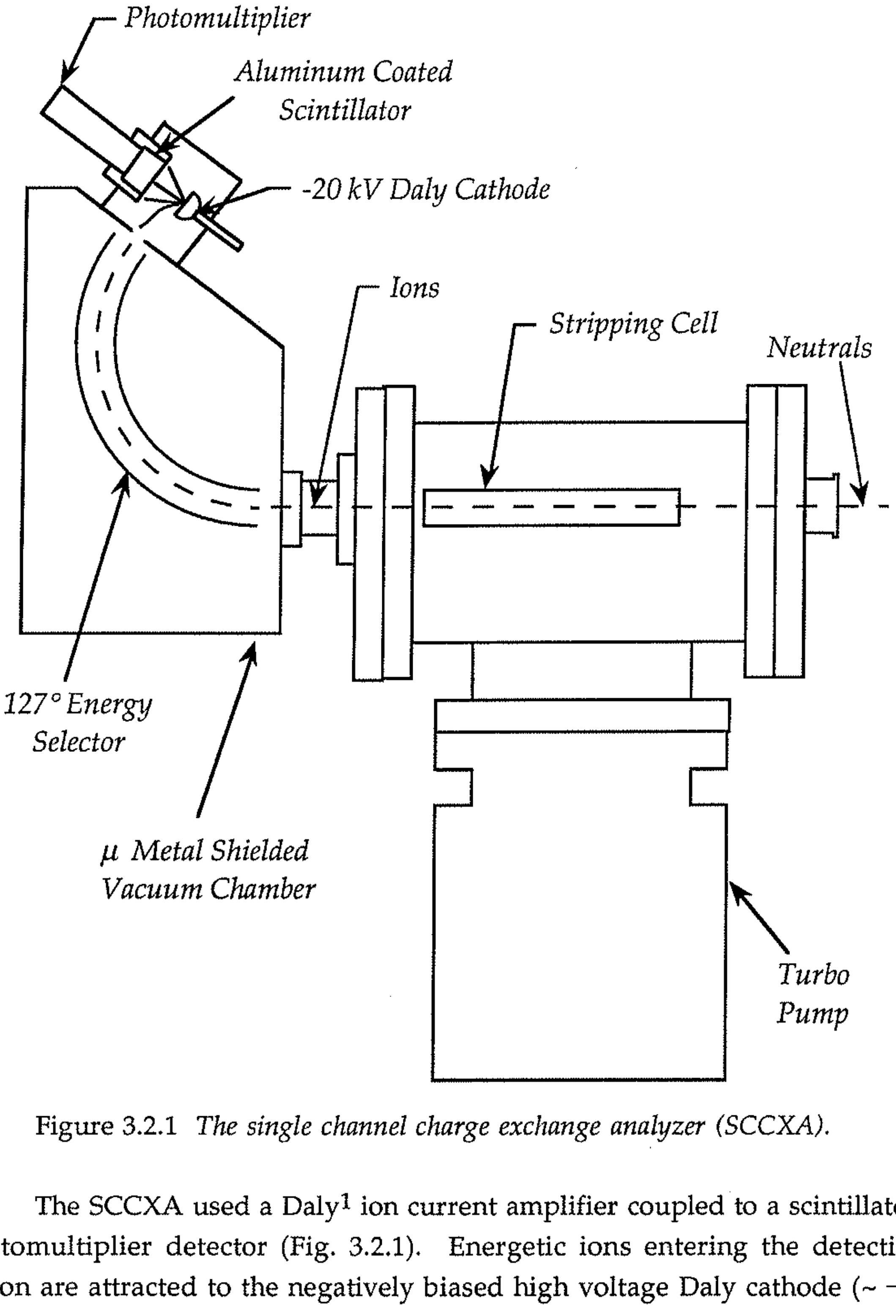

Figure 3.2.1 *The single channel charge exchange analyzer (SCCXA).*

The SCCXA used a Daly[1] ion current amplifier coupled to a scintillator-photomultiplier detector (Fig. 3.2.1). Energetic ions entering the detection region are attracted to the negatively biased high voltage Daly cathode (~ −20 kV). Upon striking the cathode, the ions induce an electron shower that is repelled from the cathode and attracted by the thin, grounded, aluminum film coating the front surface of the scintillator. The high energy electrons easily penetrate the aluminum film and deposit their energy in the scintillator. The scintillation photons released in the energy deposition process are then detected by the photomultiplier. The end result of the entire process is a current gain of approximately 10^6. The aluminum coating (~ 150 nm thick) on the scintillator also served to block the background plasma light from reaching the photomultiplier.

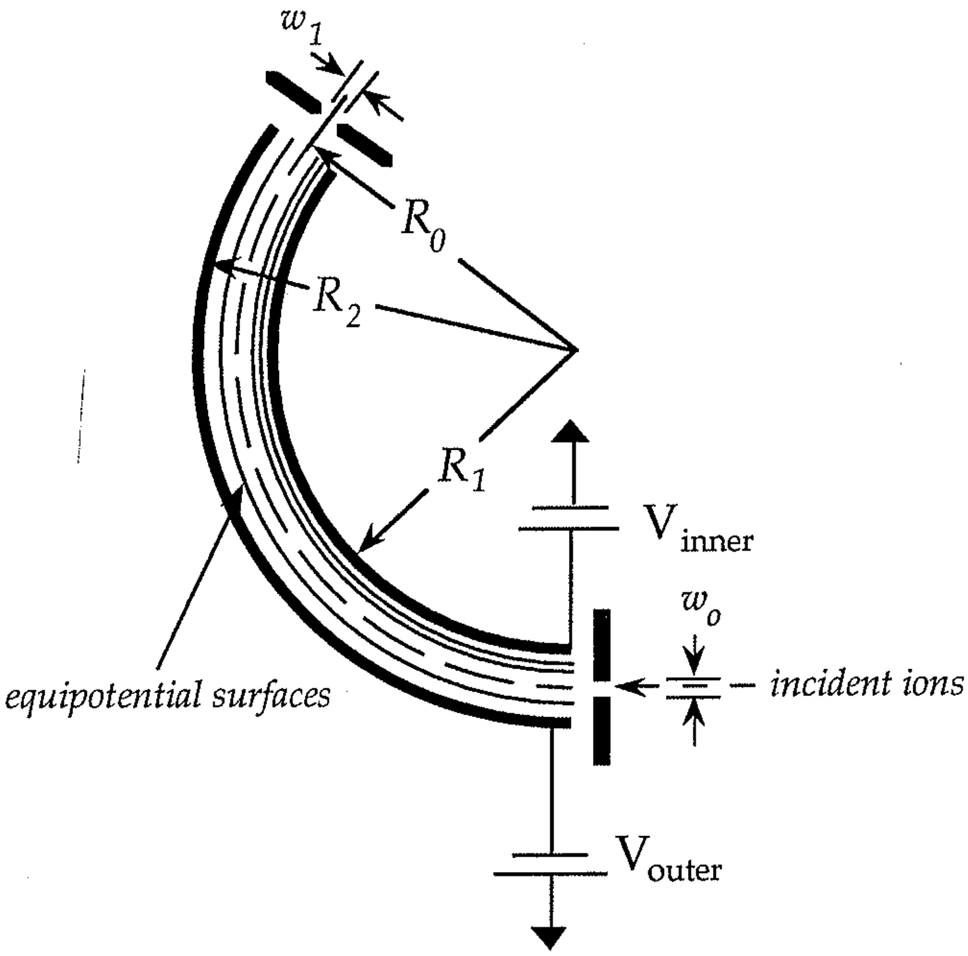

Figure 3.2.2 *Equipotential surfaces in the curved plate analyzer.*

The SCCXA functioned quite well, and was used to measure ion temperatures in the MST for nearly a year.[11,15] Because only one point in the energy distribution could be measured on each shot, measurements of the neutral energy distribution required many reproducible discharges. Consequently the ion temperature calculations were devoid of any fast time scale information and merely provided equilibrium ion temperatures (Fig. 3.2.3). The neutral flux spectrum was examined over a wide range of energies and its general character agreed with expectations for a moderate to low density plasma (Fig. 3.2.4). An ion beam was used in an attempt to calibrate the SCCXA, but because of geometrical uncertainties it was not possible to determine what fraction of the beam actually reached the Daly cathode. Extensive and unwarranted structural modifications would have been necessary to place a current monitor in front of the Daly cathode for an absolute calibration. Large, rapid (~ 10 μs) fluctuations in the neutral flux eliminated the option of sweeping the plate voltage and scanning the neutral energy distribution during a single discharge. The desire to measure the ion temperature during these fluctuations motivated the design of the current five channel charge exchange analyzer.

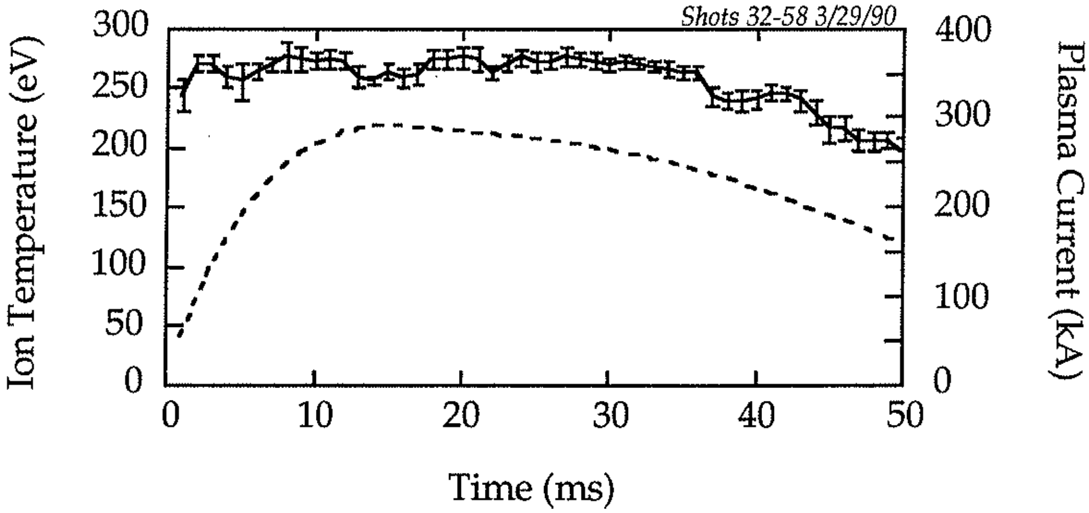

Figure 3.2.3 *Equilibrium ion temperatures, error bars from fits to flux.*

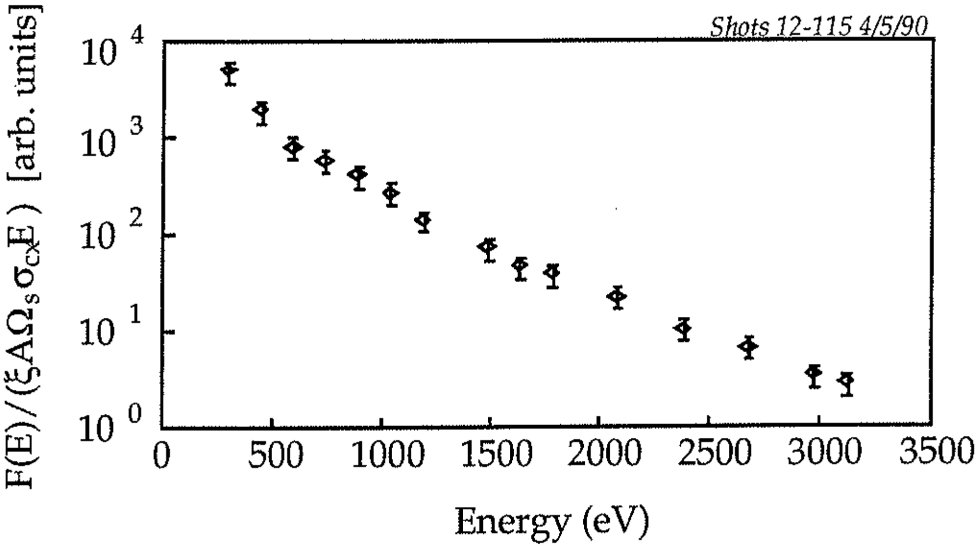

Figure 3.2.4 *Neutral flux emission, error bars indicate shot-to-shot variations.*

3.3 Fundamentals of the five channel charge exchange analyzer.

The obvious scientific advantage of a multichannel analyzer over a single channel analyzer is the capability for single shot temperature measurements. The design of the five channel charge exchange analyzer (FCCXA) for MST also incorporates a number of other features: 10 μs resolution ion temperature measurements during dynamo bursts, expandability to a analyzer with more detector channels, absolute calibration, simplicity of design, ease of assembly and disassembly, ion temperature profile measurements, and low cost. Most of the design goals were met, although some might argue that "ease of assembly and disassembly" is somewhat of an exaggeration.

The analyzer consists of two primary structures: the FCCXA (Fig. 3.3.1) and the support structure (Fig. 3.3.2). The support structure was designed to take advantage of the limited field of view through one of the small, 1.5" ports in the MST. Once the FCCXA is mounted on the support structure it can slide along an arc centered within the MST wall and view about 40% of the minor radius. Minor modifications of the port could increase the

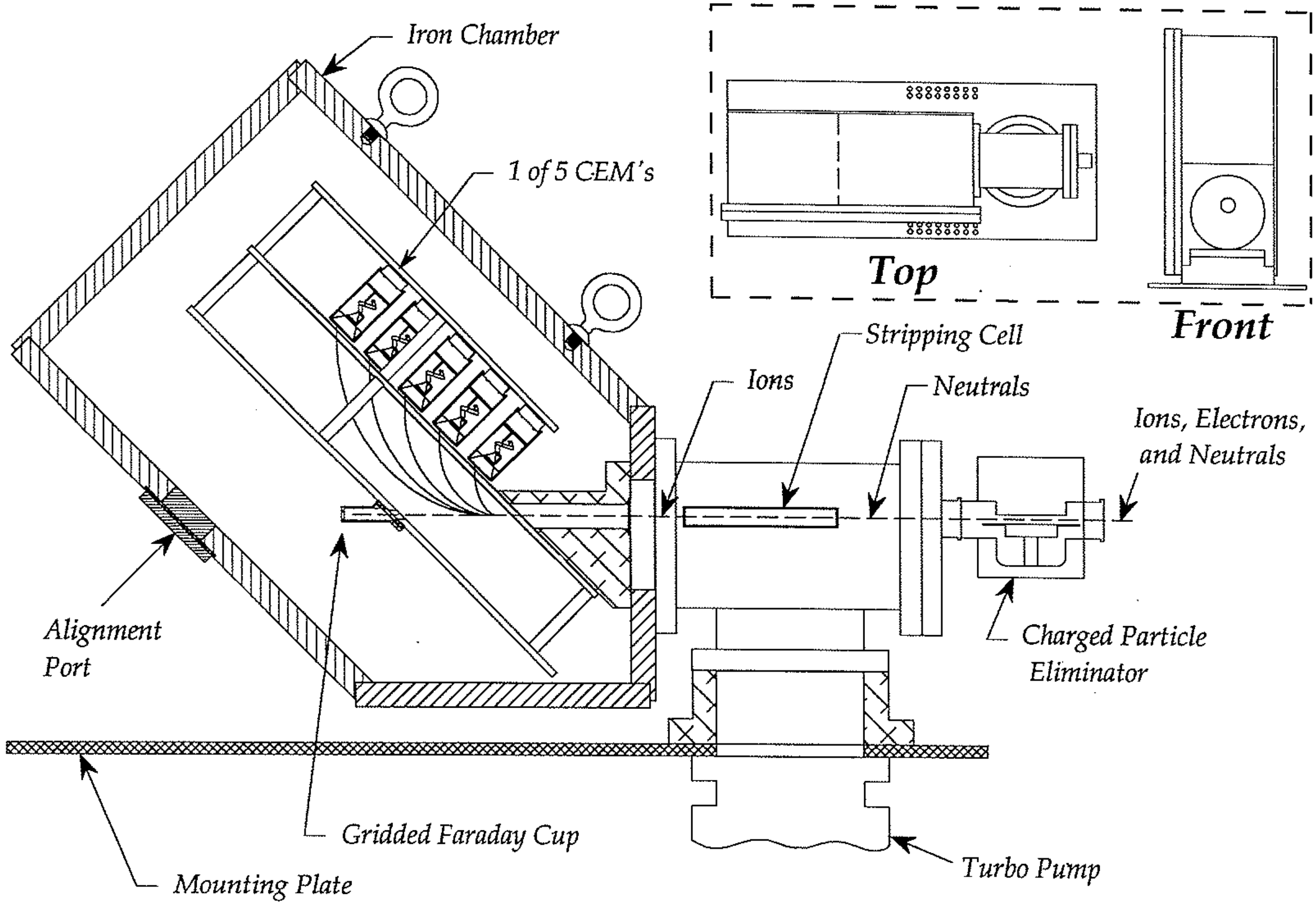

Figure 3.3.1 *Components of the five channel charge exchange analyzer.*

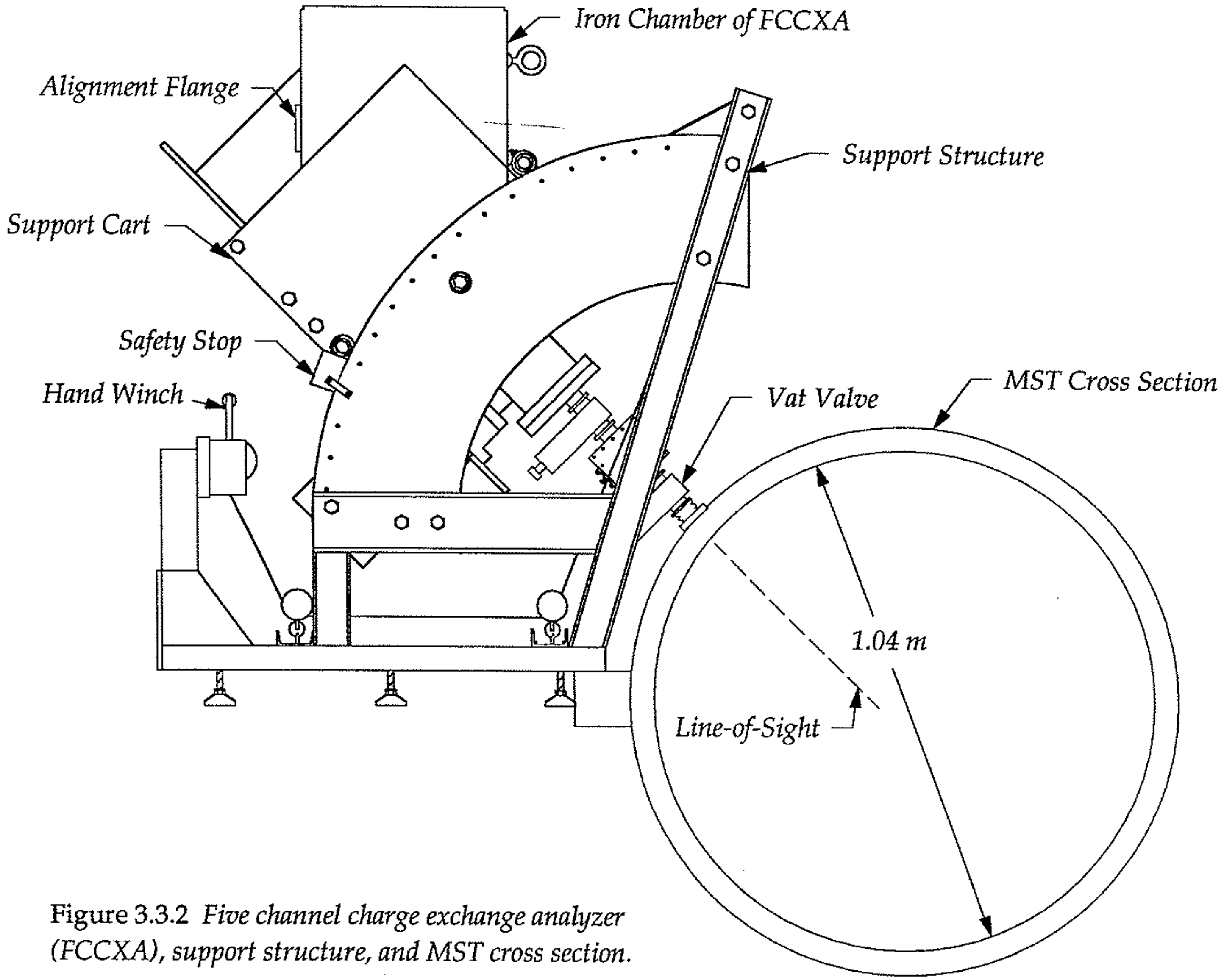

Figure 3.3.2 *Five channel charge exchange analyzer (FCCXA), support structure, and MST cross section.*

coverage to approximately 70%. Full coverage would require a completely different mounting scheme.

A soft iron vacuum chamber surrounds the energy analysis region of the FCCXA as a magnetic shield. The inch thick chamber was chemically plated with a .01″ thick layer of nickel by Pioneer Metals in Green Bay, Wisconsin to reduce outgassing and prevent oxidation. The base pressure in the iron chamber using a rotatable Varian 450 l/s grease turbo pump pumping through a conductance limited 1.5″ diameter 10″ long pipe (not shown in figure 3.3.1) was 1.5 X 10^{-8} Torr. Although the pump had a poor reliability record, it is rotatable to the point of being invertible and, when working, performed adequately. Two Bayard-Alpert ion gauges were used for general pressure measurements and a Shulz-Phelps[16] high pressure ion gauge was used to monitor the cylindrical stripping cell pressure.

3.4 Electrostatic optics and particle detectors for the five channel charge exchange analyzer.

The heart of the FCCXA is a parallel plate energy spectrometer (Fig. 3.4.1).[17,18,19,20] The rather old-fashioned, first order focusing, electrostatic parallel plate system was chosen because of its ease of construction and the potential for expansion to more channels. The optics of the parallel plate spectrometer are well understood,[20] electric fields are much easier to generate accurately than magnetic fields, and the required parts are relatively inexpensive. Before constructing the spectrometer, the electrostatics of the entire system were modeled with a Poisson's equation solving code and the ion trajectories calculated (Fig. 3.4.2).

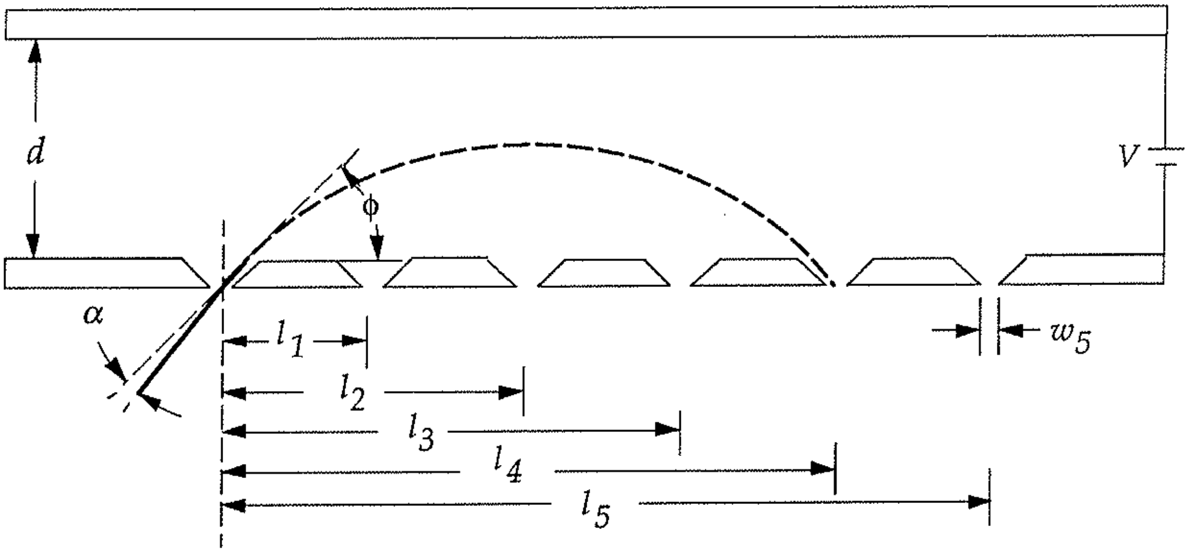

Figure 3.4.1 *The parallel plate energy spectrometer*

For particles of energy E entering at an angle ϕ, the constant electric field between two parallel plates a distance d apart with an applied potential V gives the analyzer equation

$$l_i \approx \left(\frac{2dE\sin 2\phi}{qV}\right)\left(1 - \frac{\sin^2\beta}{\sin^2\phi}\right)^{1/2}.$$

β is the entrance angle in the plane perpendicular to the direction of motion (Fig. 3.4.1). For β small, the maximum range occurs for $\phi = 45°$ and therefore first order focusing occurs for a 45° entrance angle.[20] Letting α represent the deviation from 45°, the analyzer equation to second order becomes (for small β and α)

$$l_i \approx \left(\frac{2dE}{qV}\right)(1 - 2\alpha^2 - \beta^2)$$

$$E_i \approx qV\left(\frac{2d}{l_i}\right).$$

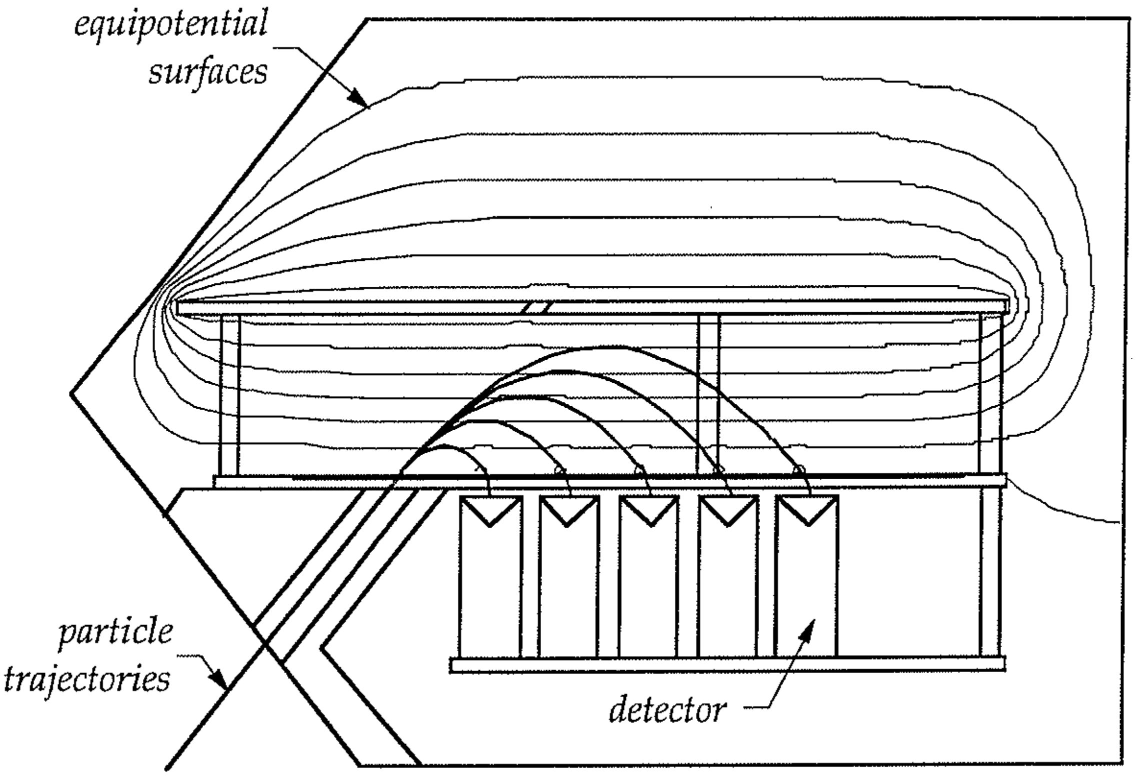

Figure 3.4.2 *Equipotential surfaces and ion trajectories in the FCCXA.*

The transmission function for this spectrometer including aberrations has been calculated and is shown in figure 3.4.3.[20] The area under the transmission function curve for the aberration case is unchanged from the aberration free case,[20] eliminating a complication that might arise during calibration of a multislit analyzer: uniform illumination of nearly identical slits with identical detector gains should produce the same signal regardless of any minor differences in construction or entrance angle.

The energy resolution of each channel in figure 3.4.1 is given by

$$\left(\frac{\Delta E}{E}\right)_i \approx \frac{w_o + w_i}{l_i}.$$

The FCCXA is currently configured with identical entrance and exit slits, yielding resolutions of 1.1% to 5.8%. An interesting alternative would be to construct a slit plate with constant $\Delta E/E$ by increasing the higher energy slit widths. This would result in more signal at the higher energies and permit all five detectors to be run at similar gains. The slit plate was designed to be easily replaced for just this reason. It is unfortunate that the parallel plate spectrometer only focuses in the direction along the particle trajectory. In fact, it defocuses the ions in the perpendicular plane and alternative spectrometer schemes that would prevent this loss of signal are discussed later in this section.

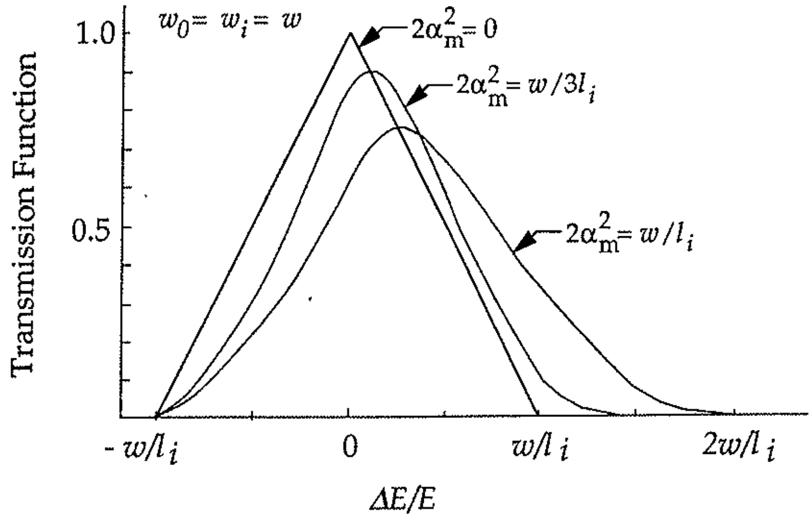

Figure 3.4.3 *Shape of the transmission function of an electrostatic analyzer with equal slit widths,* α_m *is the maximum deviation from the 45° injection angle (from Ref. 20).* $\alpha_m = 0$ *is the aberration free case.*

Each of the six slits was covered with a 90% transparent conductive mesh to maintain field uniformity across the slits. The slit width was kept less than 10% of the plate width to minimize edge effects, eliminating the need for guard plates. A Galileo Electro-Optics Corporation model 4720 continuous electron multiplier[21,22,23,24] (CEM) (Fig. 3.4.4) was mounted behind each exit slit so that ions passing through the slit at a 45° angle would strike the interior of the cone of each CEM. Each CEM was biased with its own high voltage Bertan power supply and the collected current measured with a three stage current-to-voltage amplifier.[25] The amplifiers were lowpass filtered with a single pole at 50 kHz to avoid aliasing the 100 kHz digitizers. The CEMs were operated at a current gain of approximately 5×10^5 and all five amplifiers were run at a gain of 2.24×10^6 V/A. The 4720 CEM was chosen because it is designed to run in the current mode, as opposed to the standard pulse counting mode of most CEM's. At a gain of 3 X 10^6 the 4720 has a dark current of 1 pA. Typical FCCXA signals were a few volts - over a 1000:1 intrinsic signal to noise ratio. Taking advantage of the current mode operation of the 4720 series CEM the neutral flux could be measured as rapidly as every 10 μs, fast enough to meet our design goal of measuring ion temperature fluctuations.

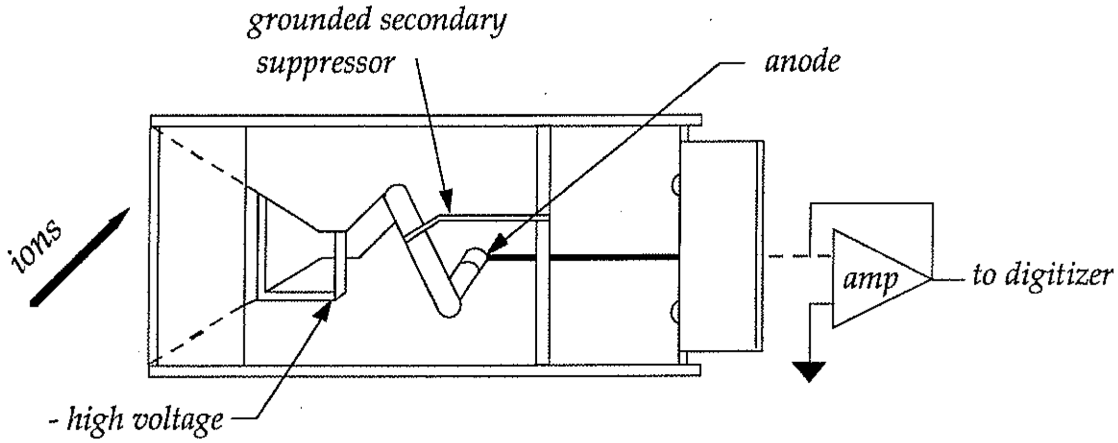

Figure 3.4.4 *The model 4720 Galileo continuous electron multiplier.*

A pulse counting detection system would be constrained to measure neutrals such that the flux was low enough to prevent simultaneous events (signal pileup). The time resolution for temperature calculations is then on the order of hundreds of microseconds, if not milliseconds.

It is possible that background light from the plasma can be reflected into the detectors by the deflector plate (Fig. 3.3.1). In fact, there is strong evidence that channels 1 and 2 are affected by plasma light during the formation of the discharge. To decrease the reflected light levels a conductive black paint has been obtained that is suitable for coating vacuum surfaces. Another source of background signal is escaping plasma ions. Some of the ions entering the stripping cell will not be neutralized, about 40% survive, and pass into the spectrometer where they are indistinguishable from the stripped neutrals.

To eliminate the ion background an electrostatic deflector was placed along the entrance path to the FCCXA (Fig. 3.3.1). However, the ion background decreases as the deflector voltage is increased until the deflector voltage exceeds approximately 500 volts. At this point the background ion signal begins to increase with increasing deflector voltage and quickly exceeds the zero deflector voltage background level. This effect occurs with both positive and negative bias voltages. Large positive voltages must reflect the plasma ions back towards the plasma. The only way for the background ion signal to increase is if ions are somehow being created upstream from the positive deflecting voltage and then enter the FCCXA. A plausible explanation is that ions (electrons) entering the deflector strike the cathode (anode) of the deflector and create an electron shower that in turn ionizes passing neutrals. In fact, this is the operating principal of many commercial ion sources. To test this hypothesis a large magnet was placed before and after the deflector region. The background ion signal was lower when the magnet was placed after the deflector, indicating that additional ions were being created in the deflector region. Large negative increases in the deflector bias current during MST discharges lend additional support for the conclusion that electron showers were being created in the deflector region.

Moving the FCCXA further away from the MST, thereby decreasing the needed deflection voltage, would permanently eliminate this source of background. In the meantime, a 2000 G magnet in conjunction with a modest deflection electric field is used to deflect the ions. The residual field due to the magnet does not create a significant additional deflection of the stripped neutrals.

The current configuration of the FCCXA may not be the optimum choice for the MST; there are certainly other neutral flux measurement techniques that have proven to be reliable and effective.[26,27,28,29,30] For example, replacing the present parallel plate optics with a spectrometer that focuses in both planes, e.g. a second order focusing cylindrical mirror analyzer (Fig. 3.4.5), will improve the low energy flux signal-to-noise. Extensive literature exists for a number of different spectrometer designs and is quite detailed.[31] The FCCXA should be viewed as the first stage in the development of a versatile charge exchange diagnostic that will play a pivotal role in all experiments on the MST in the coming years.

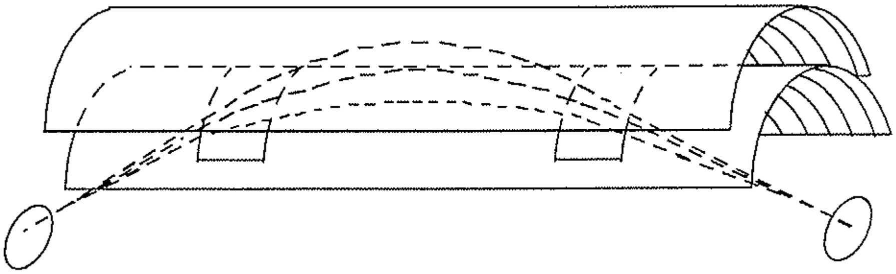

Figure 3.4.5 *The cylindrical mirror analyzer.*[31]

3.5 Calibration of the five channel charge exchange analyzer.

Many researchers have found the absolute calibration of a charge exchange analyzer to be a challenging task:

> "The analyser was found to be very useful, yet interpretation and calibration were much more difficult than anticipated."[32]

Even so warned, calibration of the FCCXA was much, *much more difficult than anticipated*. The output signal, B_i, of the FCCXA is given by

$$B_i = e\eta(E)G_i(E)F_i(E)\Delta_i(E) \qquad (3.5.1)$$

$\eta(E)$ = conversion efficiency of neutrals into ions
$G_i(E)$ = total gain of detector and amplifier (I → V)
$F_i(E)$ = neutral flux of energy E incident on conversion chamber
$\Delta_i(E)$ = energy width of channel.

As with the SCCXA, the FCCXA uses a nitrogen filled stripping cell to convert the neutral flux into an ion current. Typical stripping cells pressures used ranged from 0.1-5.0 mTorr. The cross section, for the reaction

$$H^o + N_2 \rightarrow H^+ + N_2^-$$

has been measured as a function of neutral energy[33] and the conversion efficiency, $\eta(E)$, of the FCCXA's stripping chamber versus nitrogen pressure is displayed in figure 3.5.1 for three energies. The stripping efficiency decreases sharply with decreasing energy. The extremely small nitrogen stripping efficiency below 100 eV limits charge exchange measurements to neutrals with energy above 100 eV. The linear dependence of the raw signal levels on the nitrogen pressure (Eq. 3.5.1) was verified with a series of measurements on reproducible discharges (Fig. 3.5.2).

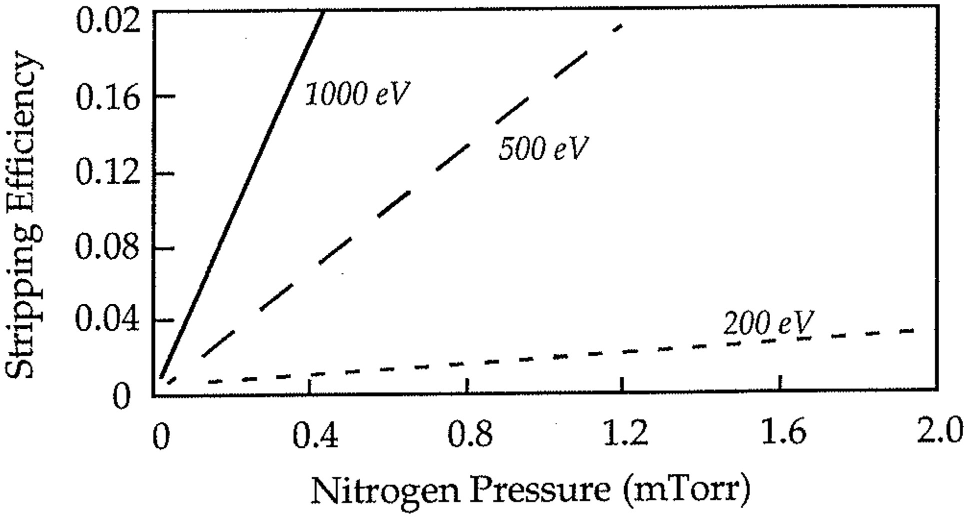

Figure 3.5.1 *Calculated conversion efficiency versus stripping pressure for three neutral energies.*

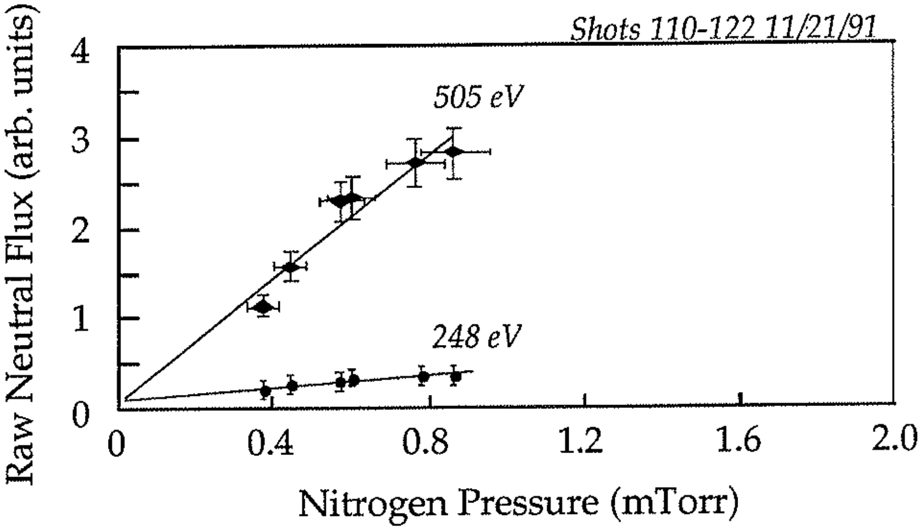

Figure 3.5.2 *Raw neutral flux versus stripping cell pressure for two energies. The solid lines are based on the calculated stripping efficiencies normalized to the 0.5 mTorr neutral flux.*

The neutral flux, $F_i(E)$, is given by equation 3.1.1 and the energy width of each channel, ΔE_i, was verified experimentally with the aid of a test ion beam. A Perkin-Elmer model #04-161 impact ionization ion gun was used as the source of the test beam. Attempts to measure the energy of the beam by varying the repelling potential on the gridded Faraday cup (Fig. 3.3.1) led to a surprising result: the collected current for a 500 eV ion beam began dropping at 450 V. After a period of considerable confusion, the problem was discovered to be one of misconception. One might naively expect that for a cold, $T \approx 1$ eV, ion beam of 500 eV a collected current versus repelling voltage plot would be flat nearly all the way out to 500 eV. In fact, a 500 eV beam with a 1 eV temperature produces the current versus repelling voltage curve of figure 3.5.3. The collected current begins to appreciably roll off at 425 eV because the distribution of even a very low temperature *beam* is actually quite broad in energy space (Fig. 3.5.4).

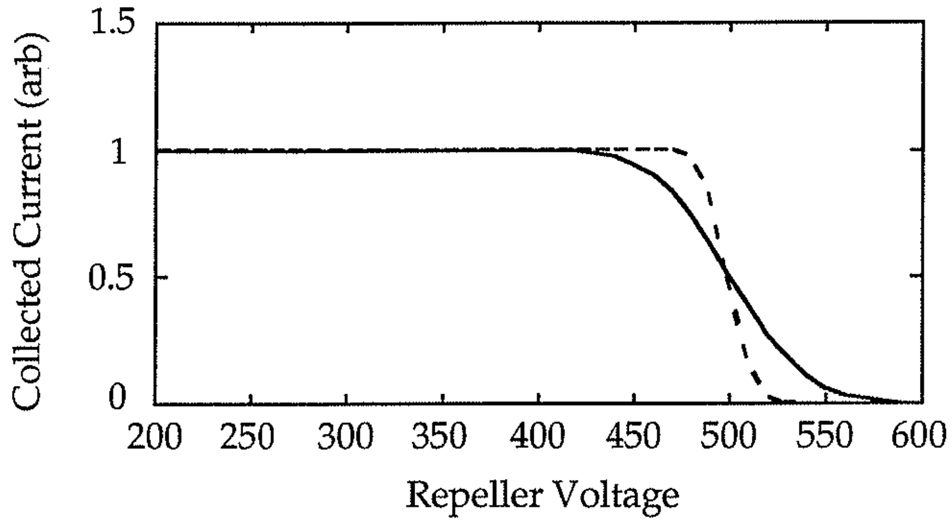

Figure 3.5.3 *Faraday cup collected current versus repeller voltage for a 500 eV beam with a 1 eV temperature (solid line). Current versus repeller voltage for a 0.1 eV beam temperature (dashed line).*

The current collected by the Faraday cup, as a function the repelling voltage V_R, is given by

$$I(V_R) = en\left(\frac{m}{2kT\pi}\right)^{1/2} \int_{V_R}^{\infty} v_Z \exp\left[-m(v_Z - u)^2/2kT\right] dv_Z ,$$

which can be analytically evaluated,

$$I(V_R) = en\left(\frac{1}{2m\pi}\right)^{1/2}\left[\sqrt{kT}\,\exp\left(-\frac{(\sqrt{eV_R} - \sqrt{E_B})^2}{kT}\right) + \sqrt{\pi E_B}\,\operatorname{erfc}\left(\frac{(\sqrt{eV_R} - \sqrt{E_B})}{\sqrt{kT}}\right)\right] ,$$

where E_B is the beam energy. Differentiating the collected current expression gives a function that peaks at the beam energy, the point of sharpest change in the slope

$$\frac{\partial I(V_R)}{\partial V_R} = -\,en\left(\frac{1}{2m\pi T}\right)^{1/2}\left[\exp\left(-\frac{(\sqrt{eV_R} - \sqrt{E_B})^2}{kT}\right)\right] .$$

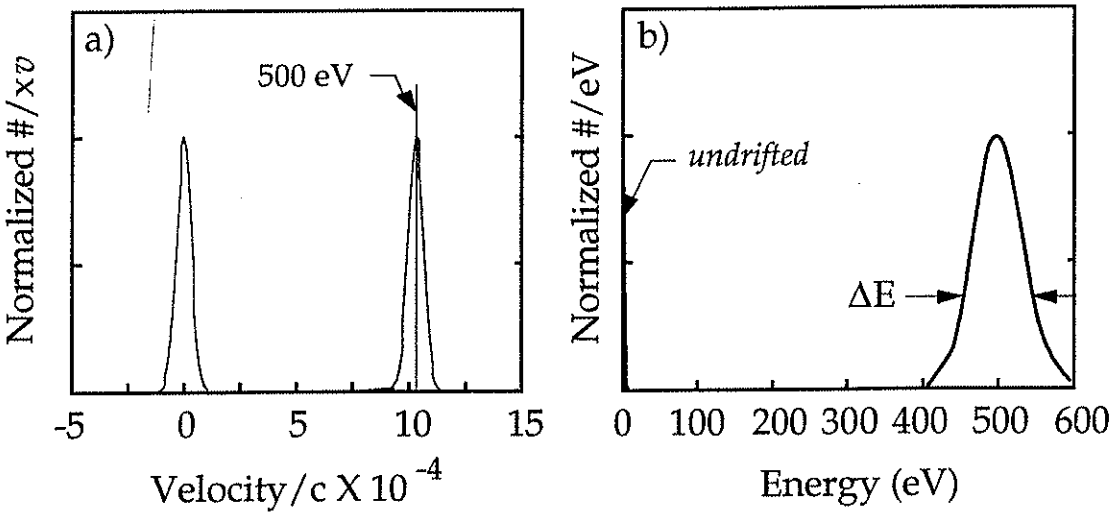

Figure 3.5.4 *a) Velocity space distributions for an undrifted ion population with a 1 eV temperature and for the same population moving with a 500 eV drift energy. b) Energy space distribution for ion populations of (a); note that the undrifted distribution width is barely visible on this scale.*

The 1/e width of this function indicates how far below the central beam energy the collected current will begin to decrease

$$\Delta V = 4\sqrt{kTE_B} \, .$$

This result reproduces the 1/e width in energy space of a drifted Maxwellian distribution,

$$\Delta E = 4\sqrt{kTE_B} \, .$$

So increasing the central energy of a beam increases its width in energy space.

The Faraday cup measurements for the 500 eV test beam, fit using the exact equations for the collected current, indicated that the beam energy was approximately 470 eV and that the beam temperature was .1 - .2 eV (1160° - 2320° C). Using these results, a ΔE of 30 - 40 eV (6.4% - 8.5%) for the beam is obtained. The manufacturer of the gun had claimed a ΔE of 10 - 20 eV in their literature, but Perkin-Elmer representatives conceded that a ΔE of 30 - 40 eV was more likely. The discrepancy in beam energy is due to space charge effects in the gun that partially shield the accelerating potential.[34]

An important side effect of using a cold beam for calibration is that the beam will not uniformly illuminate a given exit slit of the FCCXA if the ΔE of the beam is on the order of the ΔE_i of the slit pair. To compensate for partial illumination effects the response of each channel to the test beam was fit to a model function that included the beam characteristics and spectrometer transmission properties

$$S(V) \sim \int_{(1 - \frac{w}{l})E_c}^{(1 + \frac{w}{l})E_c} \exp\left[- \frac{(\sqrt{E} - \sqrt{E_B})^2}{kT}\right] \left(1 - \frac{l}{w}\left|\frac{E - E_c}{E_c}\right|\right) dE$$

E_B is the beam energy and E_c is the energy of the ions directed to the center of the slit by the applied voltage V. The second term of the integrand is the aberration free transmission function for the parallel slit spectrometer (Fig. 3.3.3) and the first term accounts for the nonuniformity of illumination by the Gaussian beam. To ensure that the beam energy was accurately known during the calibration, the beam was directed into the FCCXA with a spare 127° spectrometer. Using the curved plate spectrometer was an effective method for determining the beam energy, but the energy resolution of 127° spectrometer had the unfortunate side effect of reducing the energy spread of the beam down to about 8 eV, equivalent to a 0.007 eV beam temperature. It should be possible to substitute a Faraday cup that incorporates an energy resolving spectrometer for the existing cup; this would provide real-time measurements of the beam energy without the 127° spectrometer.

The transmission function of the 127° spectrometer is roughly triangular (actually it is trapezoidal[20]) and a Maxwellian beam with a 0.007 eV temperature is practically triangular for the energy range of interest. Therefore the calibration results were fit by the model function with the channel resolutions and analyzer constants as free parameters (Fig. 3.5.5), and a fixed *effective* beam temperature of 0.007 eV. The fit results are displayed in table 3.5.1. The measured analyzer constants are very close to the expected values. The obvious trend towards larger error for slits closer to the entrance slit is due to the larger optical aberration for those slits. As can been seen in figure 3.3.3, aberration shifts the peak of the transmission function towards higher energies.

The large discrepancy between the designed and fitted energy resolutions has two primary causes: the fitted width is very sensitive to the shape of the energy distribution of the beam after it passes through the 127° analyzer, and the resolution of each slit pair depends on the optical aberration (Fig. 3.3.3). Assuming the difference between the measured and expected analyzer constants is indicative of the true uncertainty in the resolutions, the error introduced into the temperature calculation is much less than one percent. Even if the difference between the fitted and expected resolutions is representative of the error in the resolution, the error in the calculated temperature is still less than one percent. Because the total transmitted flux is independent of aberration, and the fitted analyzer constant values are so close to the design values, the design values for the energy resolutions are used for the temperature calculations in this thesis and a relative error of 10% assumed for the resolution of each channel. If a truly monoenergetic beam, T ≤ 0.0001 eV, were available, the transmission function of the analyzer could be determined much more accurately.

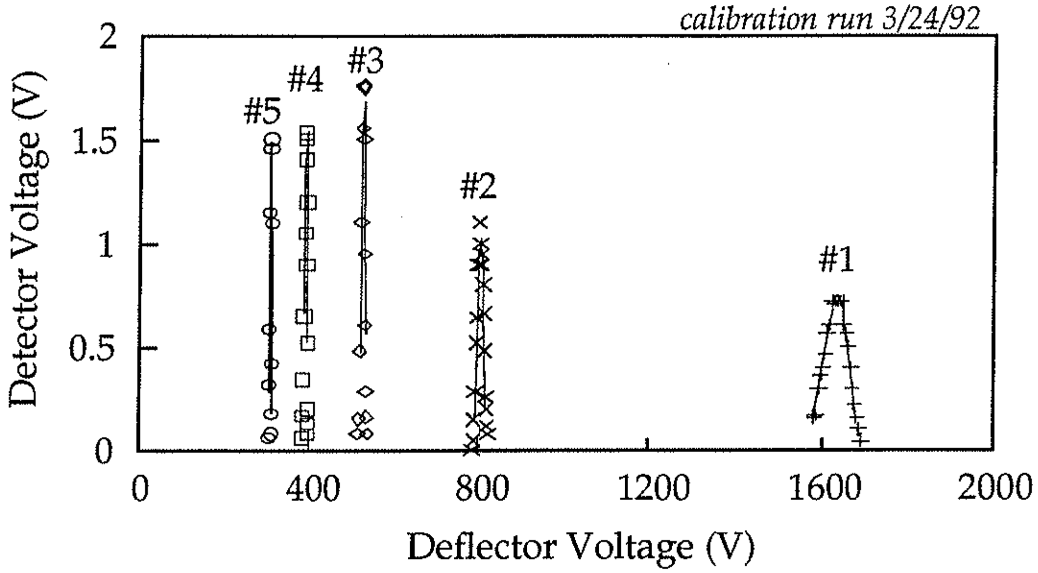

Figure 3.5.5 *Calibration results for all five exit slits. The solid lines are the fit to the model and the points are the raw data.*

Channel	*Analyzer constant from fit (eV/V)*	*% Error*	*Expected Resolution*	*Resolution from fit*	*% Error*
1	3.46	6.3	0.0580	0.0400	-31.0
2	1.70	4.4	0.0290	0.0202	-30.3
3	1.11	2.3	0.0194	0.0134	-30.9
4	0.82	0.7	0.0145	0.0084	-42.1
5	0.65	0.0	0.0116	0.0052	-55.2

Table 3.5.1 *Fitted analyzer coefficients and resolutions for the FCCXA - (calibration run 3/24/92)*

Only the total gain term, G_i, is needed to complete the calibration information. The gains of all the amplifiers were set to the same 2.24 X 10^6 V/A value and the relative gains of the detectors measured by two different methods. The first technique used reproducible plasmas as a broadband source of energetic stripped neutrals. The same region of the neutral flux distribution was used to illuminate each channel by changing the deflector voltage. The high temperature, $T_i > 50$ eV, of the plasma insured uniform illumination of each slit. The difference in resolution of each slit was accounted for, and the relative gain calculated. This method required many reproducible plasmas and calibration at different applied biases was too time consuming to be practical. Nevertheless, this method was used a number of times and the relative gains remained unchanged over a six month period.

The other technique provided not only a relative gain, but an absolute gain as well. Utilizing the built-in Faraday cup of the FCCXA, the test beam current was measured. Since $(\Delta E/E)_1$ is more than double $(\Delta E/E)_{beam}$, all of the test beam in energy space fits in channel #1 when the peak of the beam is centered in slit #1; the Faraday cup and slit pairs see the same geometric fraction of the ion beam. Using a beam temperature of 0.007 eV, the fraction of the beam entering the other channels can be calculated. In this manner, the output of each channel can be normalized to channel #1, yielding an absolute calibration of each channel (Fig. 3.5.6). The coefficients for third order polynomial fits to the detector gain results are given in Table 3.5.2. The typical gain response of 4720 CEM's operated in current mode to electron beams, provided by Galileo Electro-Optics Corporation,[35] is also shown in figure 3.5.6. The difference between ion and electron current gains is substantial at low and high bias voltages. Galileo was unable to provide any data on ion current gains for CEM's operated in current mode, although it is expected that the gain should be higher for ions than for electrons.[24]

The relative gains calculated by the two different methods are in excellent agreement (Fig. 3.5.7). The only difficulty with using the ion beam for absolute calibration was the tendency for the CEM gain to decrease if exposed to a continuous beam. This problem was solved by pulsing the ion beam on for only a few milliseconds while mapping each channel's response. Similar gain decreases do not occur during the plasma ion temperature measurements (which last much longer than a few milliseconds) because the measured ion current is much smaller than the test beam current.

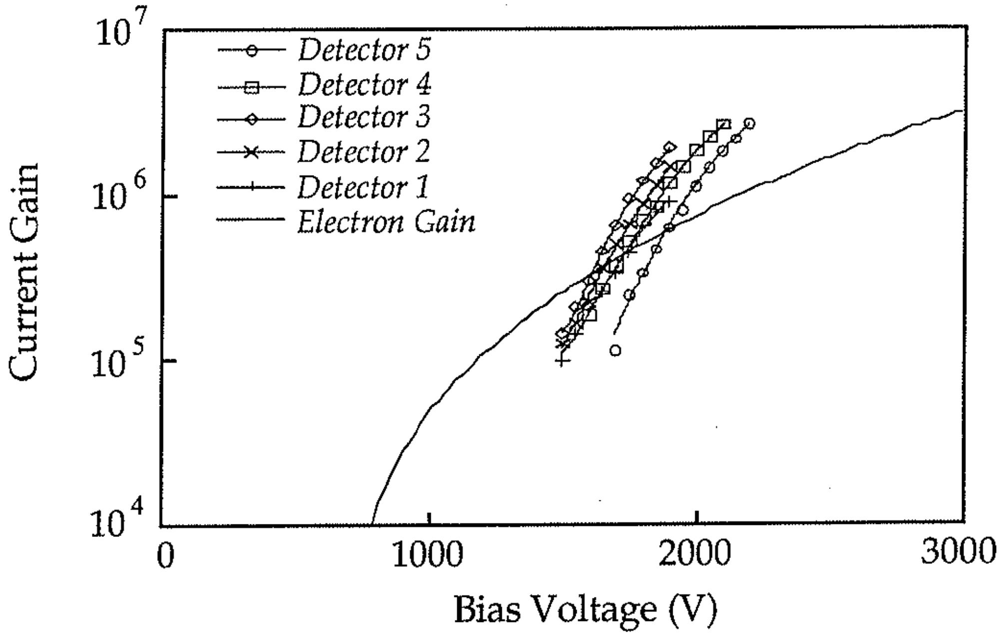

Figure 3.5.6 *Detector gain as a function of applied bias - corrected for effective bin width of each detector when non-uniformly illuminated by calibration ion beam. The solid lines are the polynomial fits.*

Detector	*A*	*B*	*C*	*D*
1	9.88×10^6	-2.62×10^7	1.77×10^7	0.0
2	-1.32×10^7	6.15×10^7	9.53×10^7	4.92×10^7
3	3.60×10^7	-1.14×10^8	1.10×10^8	-3.04×10^7
4	1.68×10^7	4.26×10^7	2.71×10^7	2.57×10^5
5	5.57×10^6	-1.76×10^6	-2.10×10^7	1.83×10^7

Table 3.5.2 *Detector gain fit coefficients for the polynomial*
Gain = $A + B(V/2000) + C(V/2000)^2 + D(V/2000)^3$.

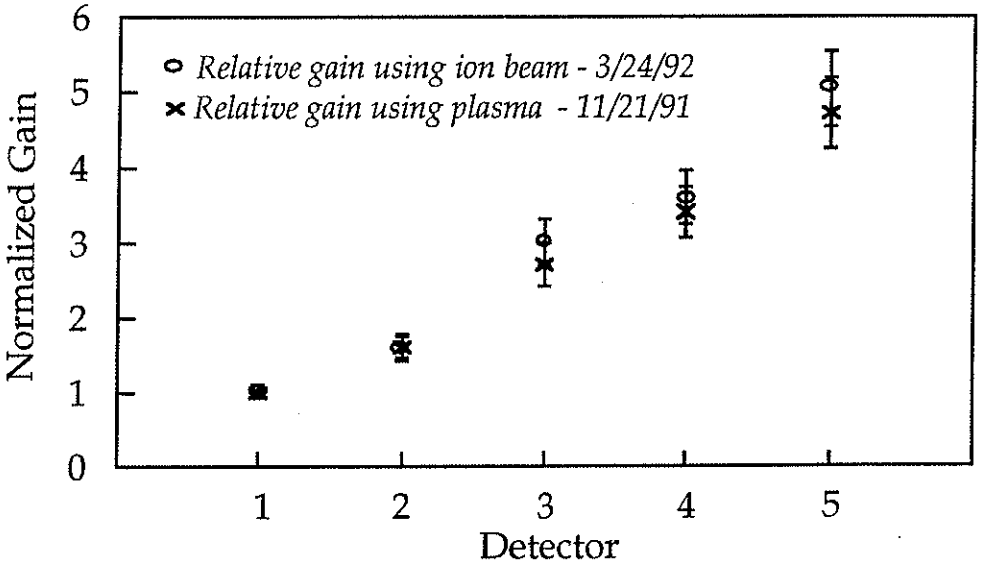

Figure 3.5.7 *Relative gains of all five detectors at different applied biases. Circles are the results from using the ion gun for the absolute calibration and crosses are the results from using the plasma for the relative calibration. Error bars are representative of the reproducibility of different calibration runs.*

3.6 Calculation of ion temperatures from the five channel charge exchange analyzer data.

Combing the neutral flux emission approximation, equation 3.1.1, and the analyzer response function, equation 3.5.1, yields,

$$\frac{B(E)}{e\eta(E)G_i(E)F_i(E)\Delta_i(E)A\Omega_s\xi\sigma_c(E)E} = \left(\frac{n_o(z^*)\,n_i(z^*)}{\sqrt{2m_i}(\pi T(z^*))^{3/2}}\right)\exp\left(-\frac{E}{T(z^*)}\right).$$

The solid angle, Ω_s, subtended by the FCCXA at the plasma edge is determined by the area of the entrance aperture at the plasma edge,

$$\Omega_s = 1.0 \times 10^{-3}\ \text{sr}.$$

The region viewed by the FCCXA in the plasma interior is also bounded by the collimation of the analyzer slits in the xy plane (see Figures 3.1.3 and 3.3.2),

$A = 8.1\ \text{cm}^2$.

For the temperature calculations a FORTRAN program fit the measured fluxes to this equation using either a nonlinear algorithm, or a linear routine that fit to the natural logarithm of the fluxes. The nonlinear fit was based on a Levenberg-Marquart minimization.[36] Although it was possible to try and fit the flux measurements to a double or triple Maxwellian distribution, satisfactory results were obtained with single temperature fits. The typical neutral energy range selected was 300 - 1500 eV and an example of a fit to a five point spectrum is shown in figure 3.6.1.

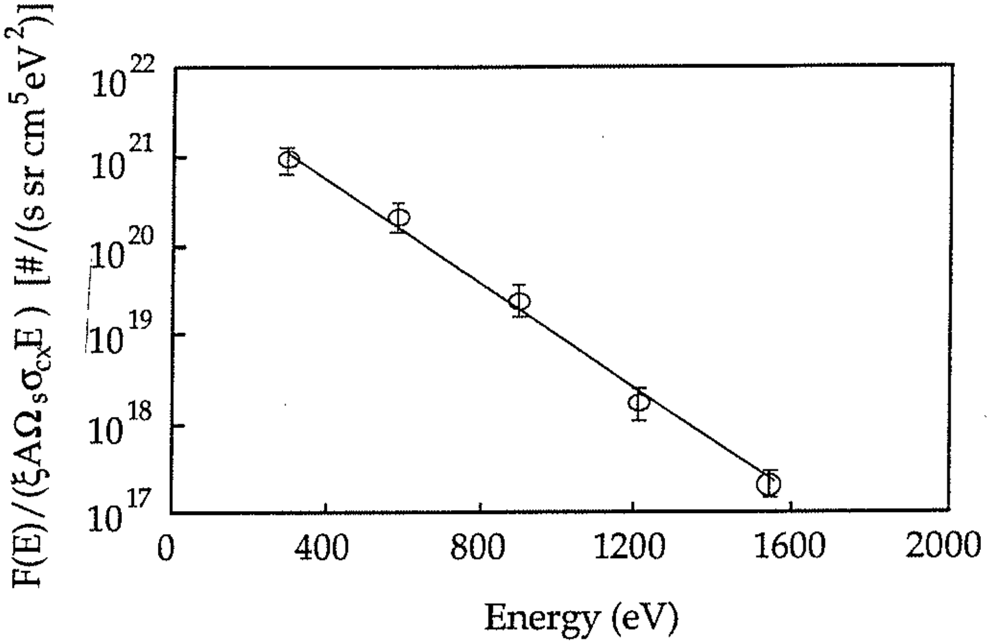

Figure 3.6.1 *Nonlinear fit to a five point neutral flux spectrum (T_i = 146 eV).*

This very simple interpretation of the neutral flux data ignores phenomena that could significantly alter the neutral flux distribution. Many of these phenomena have been shown to play an important role in neutral flux measurements on other devices. They include: fast ion losses,[37] mode-particle resonances,[38] and trapped particle effects.[39] For the most part, these effects distort the neutral flux distribution away from a simple Maxwellian and the fact that the observed distribution is well fit by a single Maxwellian distribution *suggests* that the phenomena can be ignored.

References

[1] N. R. Daly, *'Scintillation Type Mass Spectrometer Ion Detector,'* Rev. Sci. Instr. **31**, 264 (1960).

[2] A. P. Biddle, *'Ion heating in the Ion Cyclotron Range of Frequencies in the Wisconsin Tokapole II,'* Ph. D. Thesis, University of Wisconsin-Madison (1980).

[3] C. W. Erickson, *'An Experimental Study of the Ion Energy Distribution Functions in a Toroidal Octupole Magnetic Field,'* Ph. D. Thesis, University of Wisconsin-Madison (1967).

[4] Glenn Wesley Kuswa, *'Charged particle Distribution Function Measurement in a Toroidal Octupole and in a Streaming Plasma,'* Ph. D. Thesis, University of Wisconsin-Madison (1970).

[5] private communication, Samuel Hokin.

[6] R. L. Freeman and E. M. Jones, *'Atomic Collision Processes in Plasma Physics Experiments,'* Culham Laboratory Report CLM-R 137 (Culham Laboratory, Abingdon, Great Britain, 1974).

[7] I. H. Hutchinson, Principles of Plasma Diagnostics (Cambridge University Press, Cambridge 1987), pp. 284-294.

[8] K. H. Burrell, *'NEUCG: A Transport Code for Hydrogen Atoms in Cylindrical Hydrogenic Plasmas,'* J. Comp. Physics 27, **88** (1978).

[9] R. M. Mayo and L. S. Kirchenbaum, *'Neutral-particle energy analysis and charge exchange power loss in edge-dominated spheromaks,'* Phys. Fluids B **3**, 2096 (1991).

[10] Earl Scime, Samuel Hokin, Nathan Mattor, Christopher Watts, *'Ion heating and magnetohydrodynamic fluctuations in the reversed field pinch,'* Phys. Rev. Lett. **6**, 2165 (1992).

[11] Earl Scime, S. Hokin, N. Mattor, *'Dependence of Anomalous Ion Heating on the MHD Dynamo,'* Bulletin of the American Physical Society, Vol **36**, 9, (1991).

[12] M. Arnow and D. R. Jones, *'Reanalysis of the Trajectories of Electrons in 127° Cylindrical Spectrometers,'* Rev. Sci. Instrum. **43**, 72 (1971).

[13] A. LL. Hughes and V. Rojansky, *'On the Analysis of Electronic Velocities by Electrostatic Means,'* Phys. Rev. **34**, 284 (1929).

[14] John H. Moore, Christopher C. Davis, Michael A. Coplan, Building Scientific Apparatus (Addison-Wesley, 1989) pp. 305-344.

[15] S. Hokin, et al., *'Global Confinement in the MST reversed field pinch,'* Phys. Fluids B **3**, 2241 (1991).

[16] G. J. Schulz and A. V. Phelps, *'Ionization Gauges for Measuring Pressures up to the Millimeter Range,'* Rev. Sci. Instrum.. 28, 1051 (1957).

[17] G. D. Yarnold, M. A. , D. Phil. and H. C. Bolton, *'The Electrostatic Analysis of Ionic Beams,'* J. Sci. Instr. **26**, 38 (1949).

[18] H. Takeuchi, A. Funahashi, K. Takahashi, H. Shirakata and S. Yano,*'A 10-Channel Neutral Particle Analyzer for Measurements of Ion Temperatures on Tokamak Plasmas,'* Jap. J. App. Physics **16**, 139 (1977).

[19] V.S. Koidan,*'Multichannel Energy Analysis of Ions and Fast Charge-Exchange Atoms in the Investigation of a High Temperature Plasma,'* Sov. Tech. Phys. **3**, 63 (1971).

[20] Kenneth D. Sevier, Low Energy Electron Spectrometry (Wiley-Interscience, New York, 1972), p. 17-34.

[21] Edward A. Kurz,*'Effects of high current input pulses upon channeltrons,'* Rev. Sci. Instrum. **50**, 1492 (1979).

[22] D. H. Crandall, J. A. Ray, and Carmen Cisneros, *'Channeltron efficiency for counting* H^+ *and* H^- *at low energy,'* Rev. Sci. Instrum. **46**, 562 (1975).

[23] B. Hird, H. C. Suk, and A. Guilbaud, *'Channeltron entrance aperture gain variations for energetic heavy ions,'* Rev. Sci. Instrum. **47**, 139 (1976).

[24] Clifford N. Burrous, Albert J. Lieber, and Vladimir T. Zaviantseff, *'Detection Efficiency of a Continuous Channel electron Multiplier for Positive Ions,'* Rev. Sci. Instrum. **38**, 1477 (1967).

[25] PLP 1096, *'The CXA Workbook,'* Internal University of Wisconsin - Madison report.

[26] A. L. Roquemore, G. Gammel, G. W. Hammet, R. Kaita, and S. S, Medley, *'Application of an E||B spectrometer to PLT charge-exchange diagnostics,'* Rev. Sci. Instrum. **56**, 1120 (1985).

[27] M. P. Petrov,' *Particle diagnostics of a quasisteady thermonuclear plasma,'* Sov. J. Plasma Phys. **2**, 201 (1976).

[28] V. V. Afrosimov, E. L. Berezovskii, I. P. Gladkovskii, A. I. Kislyakov, M. P. Petrov, and V. A. Sadovnikov, ' *Multichannel energy and mass analyzer for atomic particles,'* Sov. Phys. Tech. Phys. **20**, 33 (1975).

[29] W. A. de Zeeuw, H. W. van der Ven, J. M. M. de Wit, and J. H. Donne, *'An electrostatic time-of-flight analyzer for simultaneous energy and mass determination of neutral particles,'* Rev. Sci. Instrum. **62**, 110 (1991).

[30] J. H. Foote, G. W. Coutts, L. R. Pedrotti, L. Schlander, and B. E. Wood, *'E||B end-loss-ion analyzer for Tandem-Mirror-Experiment-Upgrade,'* Rev. Sci. Instrum. **56**, 1116 (1985).

[31] John H. Moore, Christopher C. Davis, Michael A. Coplan, *Building Scientific Apparatus* (Addison-Wesley,1989) pp. 305-344.

[32] C. Wharton, P. Korn, D. Prono, S. Robertson, P. Auer, C. T. Dum, *'New Results in Turbulent Heating,'* in *Plasma Physics and Controlled Nuclear Fusion Research* (International Atomic Energy Energy Agency, Vienna, 1971), Vol. II, p. 25.

[33] K. Miethe, T. Dreiseidler and E. Salxborn, *'Charge transfer of hydrogen atoms in* N_2 *and in caesium vapour,'* J. Physics B **15**, 3069 (1982).

[34] private communication, Tom Rush, Perkin-Elmer Physical Electronics Division.

[35] Galileo Electro-Optics Corporation data sheet.

[36] William H. Press, Brian P. Flannery, Saul A. Teukolsky, and William T. Vetterling, *Numerical Recipes - The Art of Scientific Computing* (Cambridge University Press, New York, 1986) pp. 526-527.

[37] M.R. Wade, R. J. Colchin, A. C. England, R. H. Fowler, R. H. Goulding, M. Kwon, D. A. Rasmussen, J. A. Rome, T. D. Shepard, and C. E. Thomas, *' Fast Ion Behavior in ATF,'* Bulletin of the American Physical Society, Vol. 36, **9**, (1990).

[38] R. Kaita, R. B. White, A. W. Morris, E. D. Fredrickson, K. M. McGuire, S. S. Medley, T. J. Murphy, and S. D. Scott, *'Mode-particle resonances during near-tangential neutral beam injection in the Tokamak Fusion Test Reactor,'* Phys. Fluids B **2**, 1584 (1990).

[39] R. Kaita, R. J. Goldston, J. -P. Bussac, *'Observations of Effects of Banana Trapping on Neutral-Beam-Injected Ions in PLT,'* Nucl. Fusion **21**, 953 (1981).

CHAPTER 4

HIGH FREQUENCY MAGNETIC FLUCTUATION MEASUREMENTS IN THE MST

4.1 High Frequency Magnetic Fluctuation Probes.

Rugged magnetic fluctuation probes have been under development at the University of Wisconsin-Madison for many years.[1,2] The interior of the MST is lined with 86 sets of three-axis magnetic sense coils.[3] The magnetic fluctuation measurements undertaken for this thesis have extended the frequency range of the previous fluctuation measurements in the MST from 1-250 kHz to 0.5-5.0 MHz. To improve the frequency response of the probe a thin coating of a silver suspension was used as an electrostatic shield, instead of the normal stainless steel sheath (Fig. 4.1.1). The coil form itself was first designed by Saeed Assadi.[2] For these experiments nonconductive boron nitride was substituted for the original conductive graphite coil form. The coil was wound with approximately five turns of AWG #34 HML-coated magnetic wire, giving an effective area of about 10 mm^2. A detailed discussion of the response of small coils to short wavelength, high frequency fluctuations is given in reference 4.

Calibration of the probe in the .5-5 MHz frequency range was a tedious process. A thorough review of the calibration technique is also found in reference 4 and only a summary is given here. A Helmholtz coil with a resonant frequency of 10 MHz was used in conjunction with the Constant Current Calibrator (CCC) constructed by D. Kortbawi to provide the calibration magnetic field. The CCC was driven with a HP606A function generator and the current flowing through the Helmholtz coil measured with a Pearson Model 110 current monitor. Using the carefully measured on-axis Gauss per Ampere response of the Helmholtz coil as a function of frequency[4] the frequency response of the electrostatically shielded probe and amplifier combination was determined (Fig. 4.1.2).

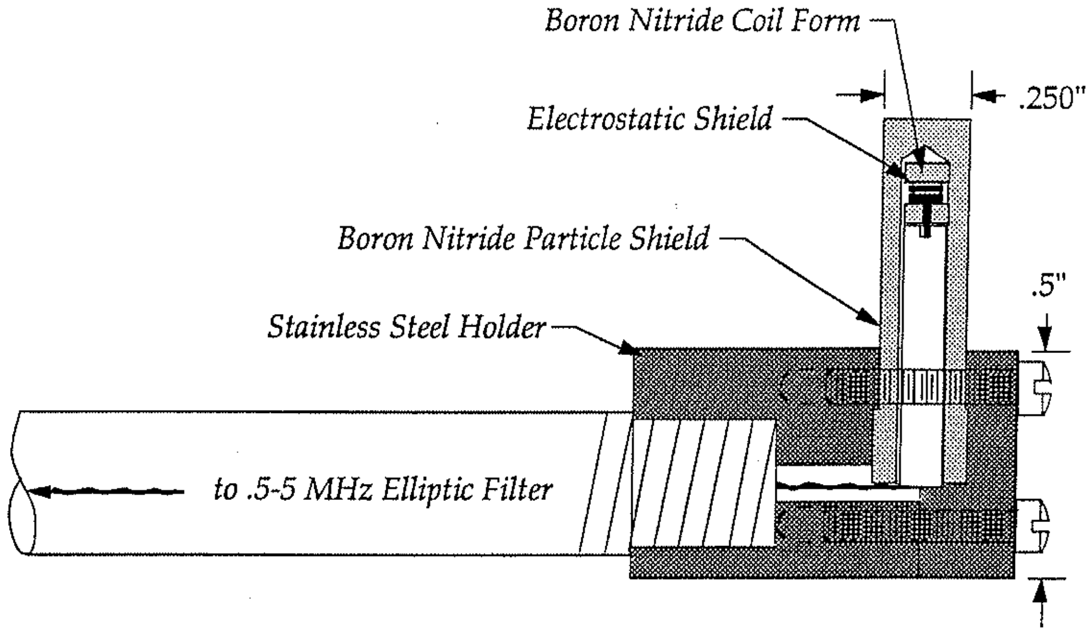

Figure 4.1.1 *The High Frequency Magnetic Probe*

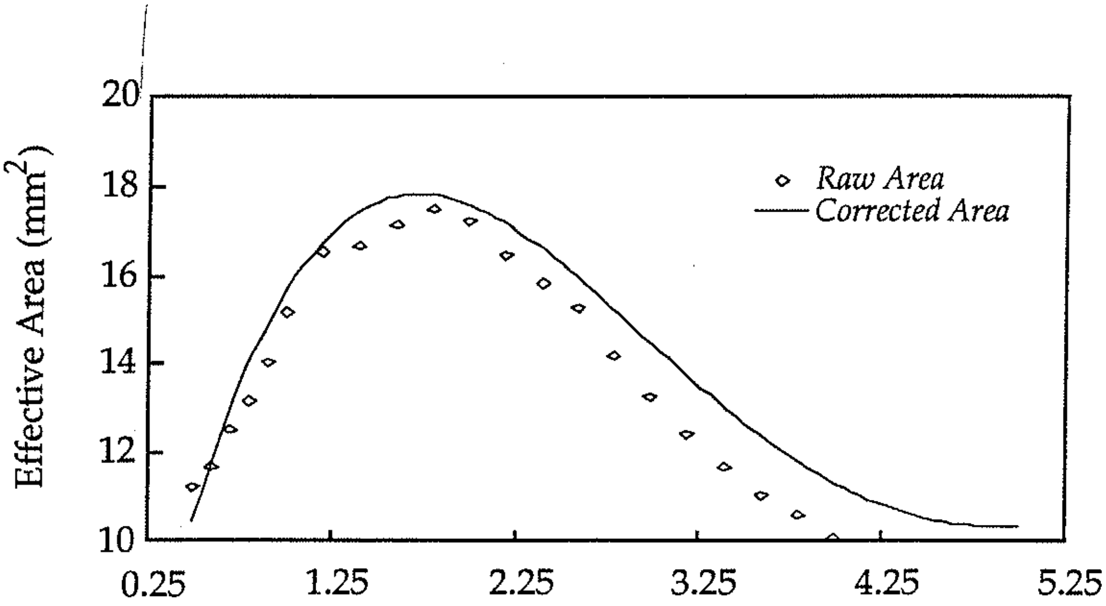

Figure 4.1.2 *Raw effective area of probe-amplifier combination and area corrected for Helmholtz coil response.*

4.2 High Frequency Amplifiers.

It is particularly important that the probe-amplifier combination be calibrated in the exact same configuration used for the actual measurements. Variations in grounding procedures and cable lengths will change the frequency response of the system. The high frequency amplifier used had a fixed gain of ~66 dB (~2000) with a variable 0-31 dB attenuator at the input to adjust the overall gain and dynamic range of the system. Two removable n=3 Cauer-Elliptic band-pass filters were used in the amplifier for frequency filtering.[5] The gain of the amplifier in the range .5-5 MHz was nearly constant, with sharp corners at .5 and 5 MHz. The effective area in figure 4.1.2 includes the amplifier response and the corrected area curve incorporates the known response of the Helmholtz coil.[4] The output of the amplifier was recorded with a DSP model 2001A digitizer sampling at 10 MHz. The noise level of the amplifier was approximately one bit of the eight bit 2001A digitizer. The relatively small dynamic range of the digitizer was a persistent problem during measurements of the dynamo bursts in MST. The change in fluctuation level during a burst was typically beyond the capacity of the digitizer if the amplifier was configured to detect the base fluctuation level in the plasma. This meant that the base fluctuation level was normally attenuated down to the noise level in order to track the burst phenomena.

One particularly helpful aspect of these measurements is that the goal was to detect *features* in the frequency spectrum of the fluctuations. Absolute measurements were helpful in calculating the power in the fluctuations, but the detection of *features* does not require an absolute calibration.

References

[1] J. S. Sarff, '*Studies of a Poloidal Divertor Reversed Field Pinch,*' Ph. D. Thesis, University of Wisconsin-Madison (1988).

[2] S. Assadi, Ph. D. Thesis, University of Wisconsin-Madison, in progress.

[3] J. A. Beckstead, '*Sawteeth in the MST Reversed Field Pinch,*' Ph. D. Thesis, University of Wisconsin-Madison (1990).

[4] E. J. Haines, '*Measurement of Magnetic Fluctuations at the Small Spatial Scales in the Tokapole II Tokamak,*' Ph. D. Thesis, University of Wisconsin-Madison (1991).

[5] D. Kortbawi, '*Alfven Wave Studies on a Tokamak,*' Ph. D. Thesis, University of Wisconsin-Madison (1988).

CHAPTER 5

EQUILIBRIUM ION TEMPERATURE MEASUREMENTS

5.1 History of anomalous ion heating in toroidal confinement devices.

As mentioned earlier, the high ion temperatures of RFP plasmas have been considered one of the major unexplained features of the RFP. It is remarkable that during the early stages of the development of the tokamak, anomalously high ion and electron temperatures were considered one of the pressing issues facing magnetic fusion research. In fact, more than a fourth of the 1971 International Atomic Energy Association Conference on Controlled Nuclear Fusion held in Madison, Wisconsin was devoted to discussions of anomalous electron and ion heating mechanisms.[1] At that time, almost all of the plasmas studied were Ohmically heated; i.e. resistive I^2R heating via the plasma current was used to heat the electrons. Using basic kinetic theory it can be shown that in a plasma with an externally applied electric field the current is carried almost entirely by the electrons.[2] Collisions with ions and other electrons deflect the current carrying electrons; converting some of their flow energy into thermal energy. This energy conversion process is quantified by a plasma *resistivity*, η, and the amount of energy converted into electron heat is given by $\int \eta J^2 dV$, just as in a current carrying wire.

In an Ohmic discharge, only the electrons are directly heated, so the ions can only be heated by ion-electron thermal equilibration. In many RFPs and early tokamaks, however, ion temperatures greater than electron temperatures have been observed.[3,4,5,6] Clearly plasmas cannot violate the Second Law of Thermodynamics and have thermal energy flow from the electrons to the hotter ions. Therefore, the ions must acquire energy through some channel that bypasses the electrons. Other magnetic confinement devices that internally generate magnetic fields, e.g. spheromaks and field reversed configurations, have also reported anomalously high ion temperatures.[7,8] Ion temperatures equal to and greater than the electron temperature have been observed in MST discharges. It will be shown in section 5.4 that enough energy is flowing into MST discharges to account for the measured ion and electron temperatures and it will be shown in section 5.5 that the ion temperature exceeds what could be reasonably expected from ion-electron collisional heating.

5.2 Ensemble averaged ion temperature measurements.

A number of diagnostics on the MST provide only a limited time record. Therefore, a series of 200 identical MST discharges were used to fully investigate the temporal evolution of plasma parameters relevant to the study of ion heating in the RFP. The equilibrium, shot averaged, ion temperature for nearly one hundred 360 kAmp discharges is shown in figure 5.2.1. Each temperature point in figure 5.2.1 is from a fit to the five point FCCXA neutral energy spectrum. Typical fits are shown in figure 5.2.2. The large, approximately 50%, error bars for the points used in the fit are due to statistical errors arising from the irreproducibility of the neutral flux emission at each energy. The large fluctuations in the neutral flux emission and plasma ion temperature are discussed in detail in chapter 7. Other relevant operational parameters are shown in figure 5.2.3, they are: plasma current, reversal parameter, pinch parameter, loop voltage, and toroidal magnetic field. Poor signal levels do not permit reliable FCCXA ion temperature measurements prior to 5 milliseconds into the discharge, however, by 5 milliseconds the ion temperature is already 150 eV. As can be seen from figure 5.2.2, the toroidal magnetic field does not reverse until 5 milliseconds. Thus, rapid and intense ion heating occurs in the strongly relaxing, ultra-low-q magnetic configuration that occurs before the magnetic field at the edge reverses direction, i.e. before the plasma becomes a RFP. An ultra-low-q device has a normalized toroidal to poloidal field ratio at the edge much less than unity,

$$q(r{=}a) = \frac{aB_\phi}{RB_\theta} = \frac{aF}{R\theta} \ll 1 .$$

This configuration is quite similar to some of those early toroidal confinement experiments that exhibited anomalous ion heating.[6,9]

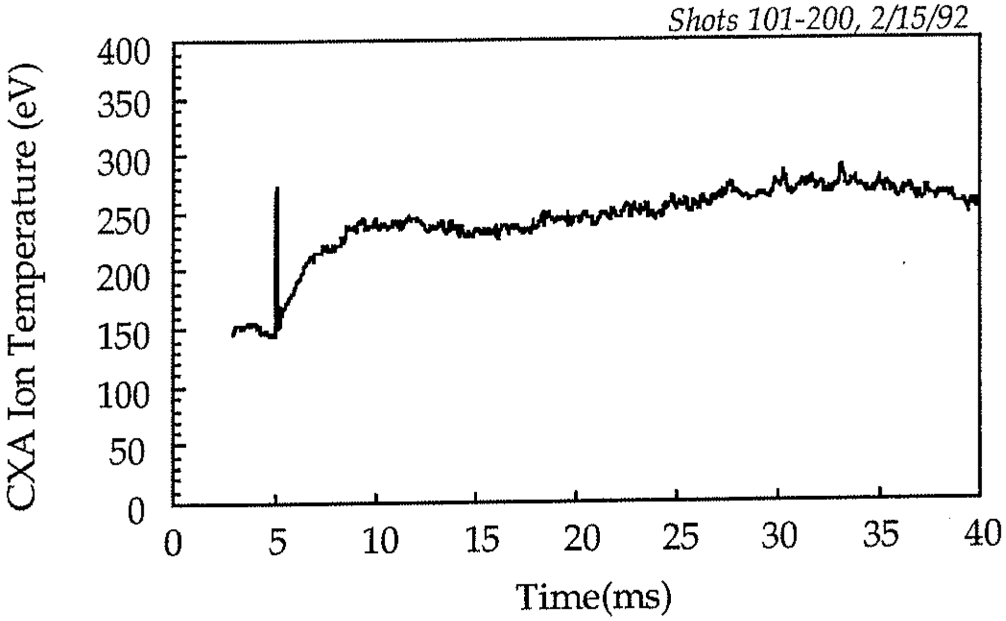

Figure 5.2.1 *Ensemble averaged ion temperature for 99 identical discharges.*

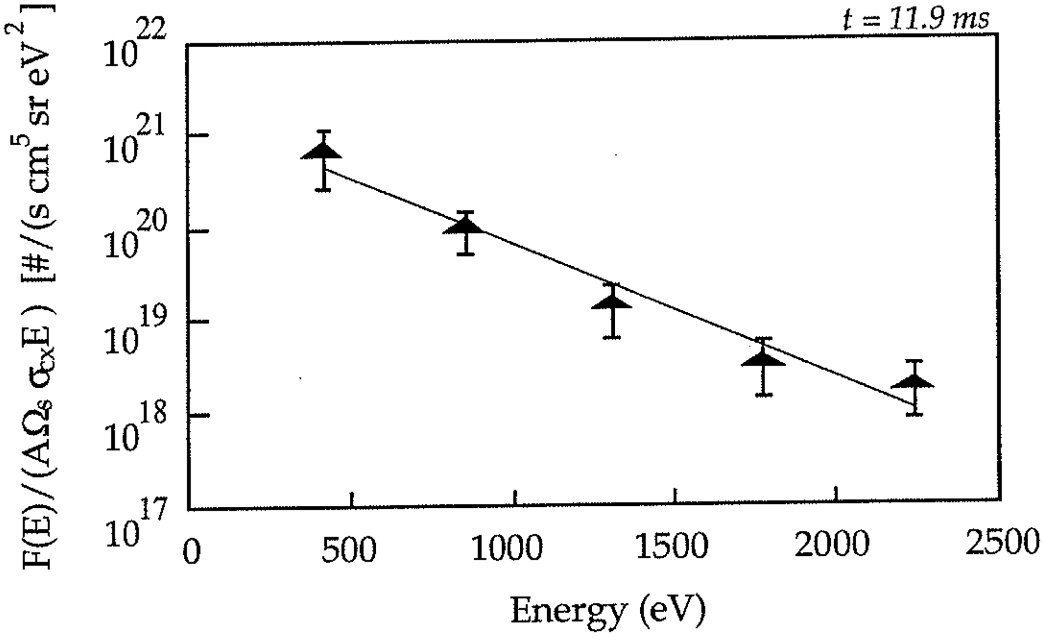

Figure 5.2.2 *Typical fit for temperature calculations of figure 5.2.1. Large statistical error in each point due to shot-to-shot variation in neutral flux. Note that spectrum is not always as well fit by a single Maxwellian as in Fig. 3.6.1.*

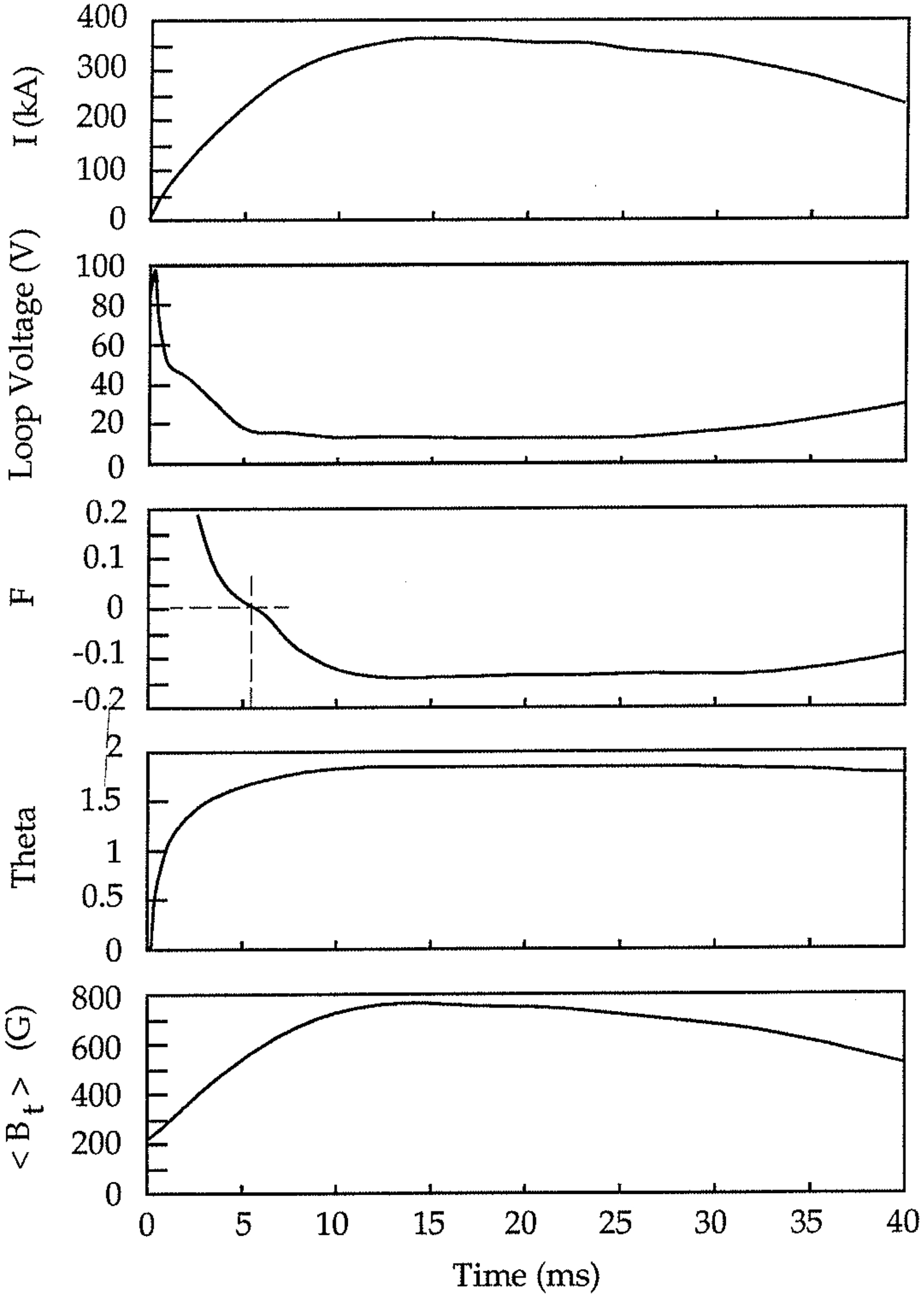

Figure 5.2.3 *Ensemble averaged operational parameters for the same discharges used for figure 5.2.1. Note that reversal occurs just after 5 ms.*

To corroborate the charge exchange derived ion temperature measurements, the Doppler broadened CV 227.1 nm line was used to calculate the impurity ion temperature. For the same discharges used in figure 5.2.1, the ensemble averaged Doppler ion temperature and FCCXA ion temperature are shown in figure 5.2.4. A typical fit to the Doppler measurements is shown in figure 5.2.5. The agreement, both in magnitude and early time evolution with the charge exchange ion temperature is evident. The charge exchange ion temperature increases as the discharge current begins to decay while the Doppler ion temperature decreases. During this same time period, as will be shown later, the plasma density is steadily decreasing. For a given ion heating power and constant energy confinement time a lower density would imply a higher temperature, and under such assumptions the charge exchange temperature rise seems plausible. The ion temperature calculated from CV emission reflects the local ion temperature, but the spatial distribution of C^{4+} ions is determined by the electron temperature magnitude and profile (Fig. 3.2.6). Therefore, if the electron temperature profile changes, changes in the CV ion temperature may simply reflect the character of the ion temperature profile as the location of the CV emission varies.

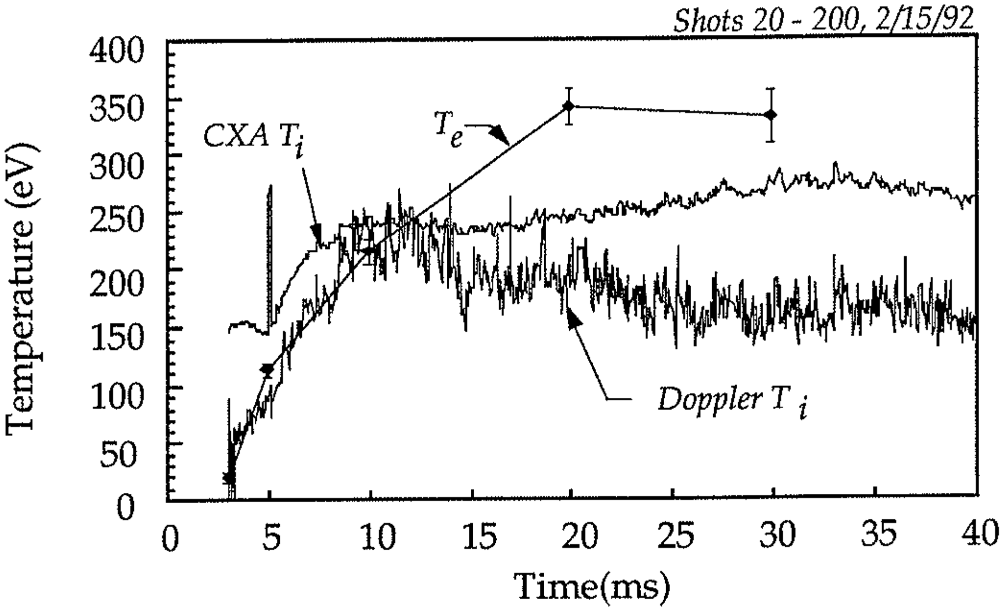

Figure 5.2.4 *Ensemble averaged CV Doppler and charge exchange ion temperatures and Thomson scattering electron temperature.*

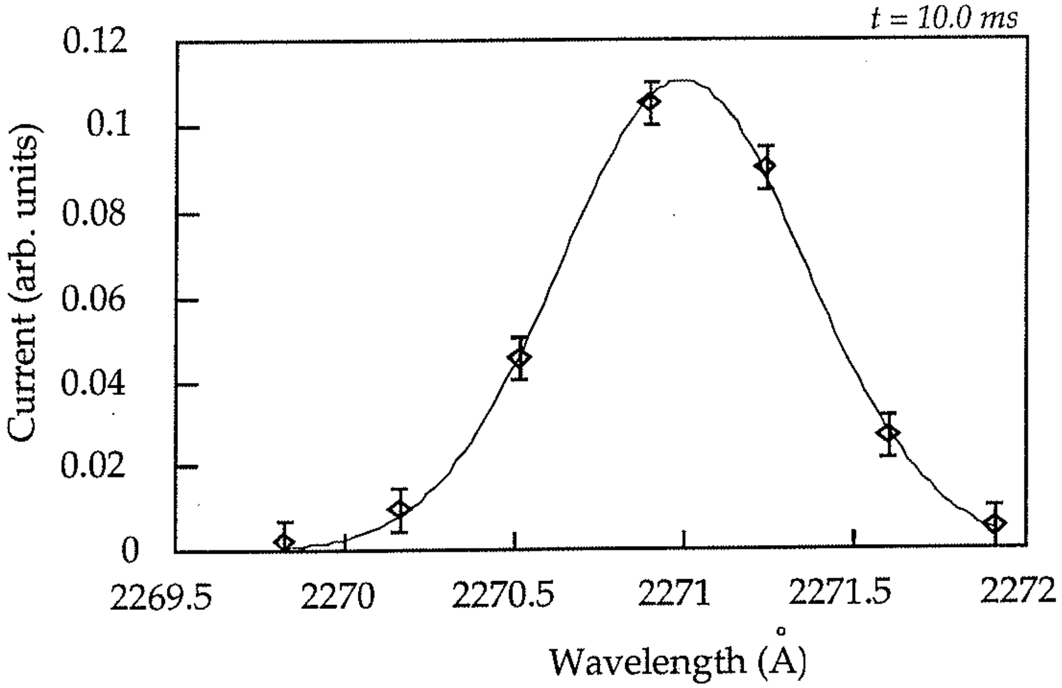

Figure 5.2.5 *Typical fit for Doppler ion temperature calculations of figure 5.2.4 - $T_i = 229$ eV.*

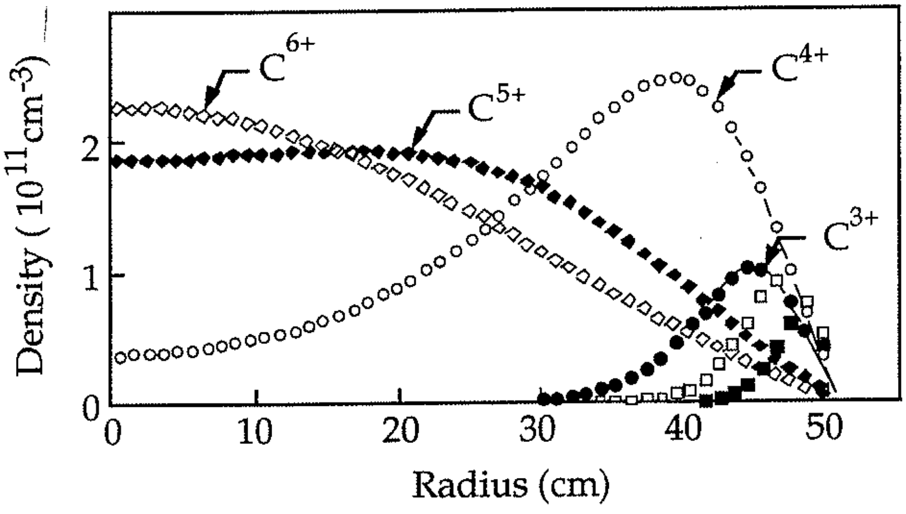

Figure 5.2.6 *Theoretical CV (C^{4+}) distribution in the MST, for a nearly parabolic electron density, fairly flat electron temperature profile, and a constant diffusion coefficient of 50 m^2/s ($n_{eo} = 4.5 \times 10^{13}$ cm^{-3}, T_{eo} = 350 eV).*[10]

The current Thomson scattering diagnostic laser fires a single pulse during each discharge. By changing the firing time every shot it was possible to measure the ensembled averaged evolution of the electron temperature (Fig. 5.2.4). This technique proved to be quite successful. Although individual shots may not have had sufficient signal levels to determine the electron temperature at 3 milliseconds, summing the raw signals over ten shots provided enough signal for respectable temperature calculations. The electron temperature is clearly lower than the ion temperature before 10 milliseconds and then rises above the ion temperature (Fig. 5.2.4).

5.3 Evolution of density and charge exchange power losses during a MST discharge.

The Thomson scattering diagnostic was used to determine the central electron temperature for each discharge. As the laser firing time was varied to determine the electron temperature evolution, the relative electron density evolution was measured as well (Fig. 5.3.1).

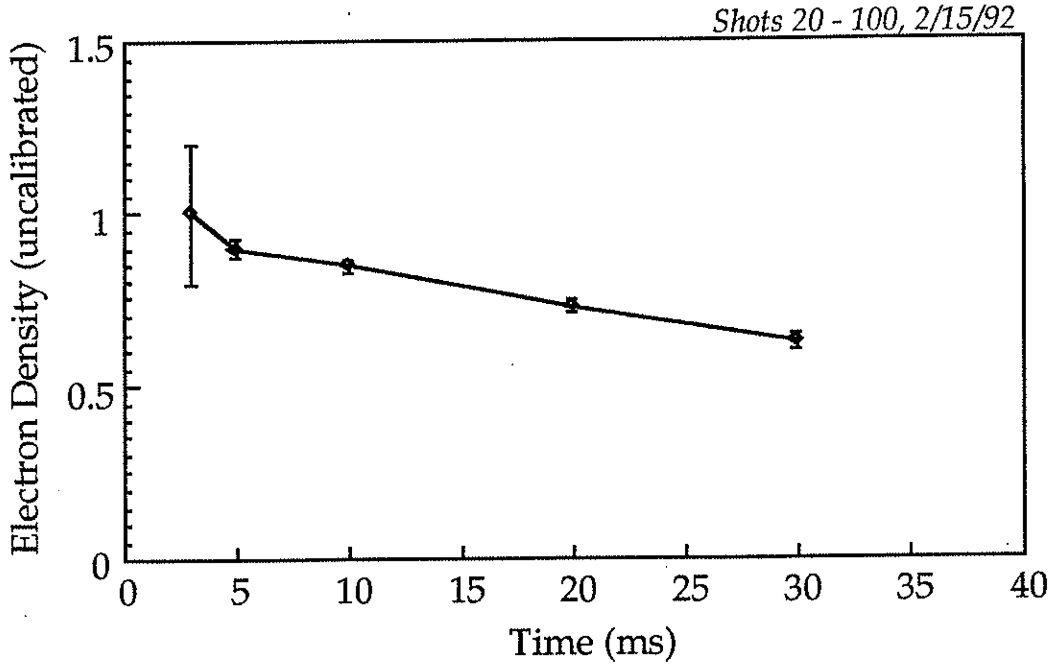

Figure 5.3.1 *Ensemble averaged relative electron density versus time.*

With an absolutely calibrated charge exchange diagnostic the central neutral density can be determined if the ion density is known. Assuming quasi-neutrality, $n_i = n_e$, and the approximation for the source integral described in section 3.1 (Fig. 3.1.4), the relative evolution of the central neutral density is given in figure 5.3.2. The absolute value of the calculated neutral density depends not only on the value used for the ion density, but also on the profile and neutral transport assumptions of section 3.1. Previous calculations of the central neutral density via H_α emission measurements place the central density in the range 1 X 10^9 - 1 X 10^{10} cm^{-3}, in good agreement with these results.[11]

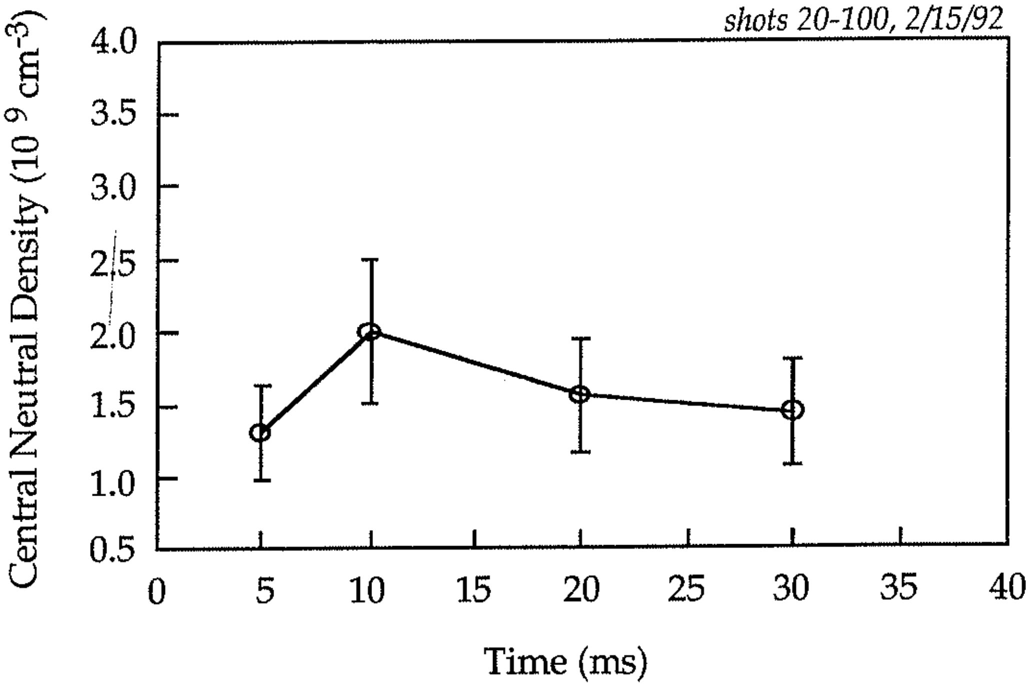

Figure 5.3.2 *Ensemble averaged neutral density assuming* n_{eo} = *1.0 X* 10^{13} cm^{-3} *at* t = *3 ms. Large error bars due to uncertainty in source integral approximation.*

In order to determine the charge exchange power loss, the neutral flux over the energy range 93 - 2371 eV was measured. This was accomplished by changing the deflection voltage of the FCCXA every 5 shots during the same series of identical shots used for the temperature measurements. The resultant neutral spectrum at 20 ms into the discharges is displayed in figure 5.3.3. An absolute conversion of the near-field, collimated neutral emission measured by the charge exchange analyzer into the total charge exchange power loss of the plasma requires complete density and temperature profile information and a full 3 dimensional calculation of the attenuation of neutrals born inside the plasma. Even if the theoretical profiles are used, the attenuation calculation is non-trivial. Neutrals that do not exit purely radially must be tracked laterally through the torus until they exit the plasma. With the added complication of multiple charge exchange collisions, keeping track of the neutral and ion densities along the trajectories of neutrals born everywhere within the plasma is quite challenging.

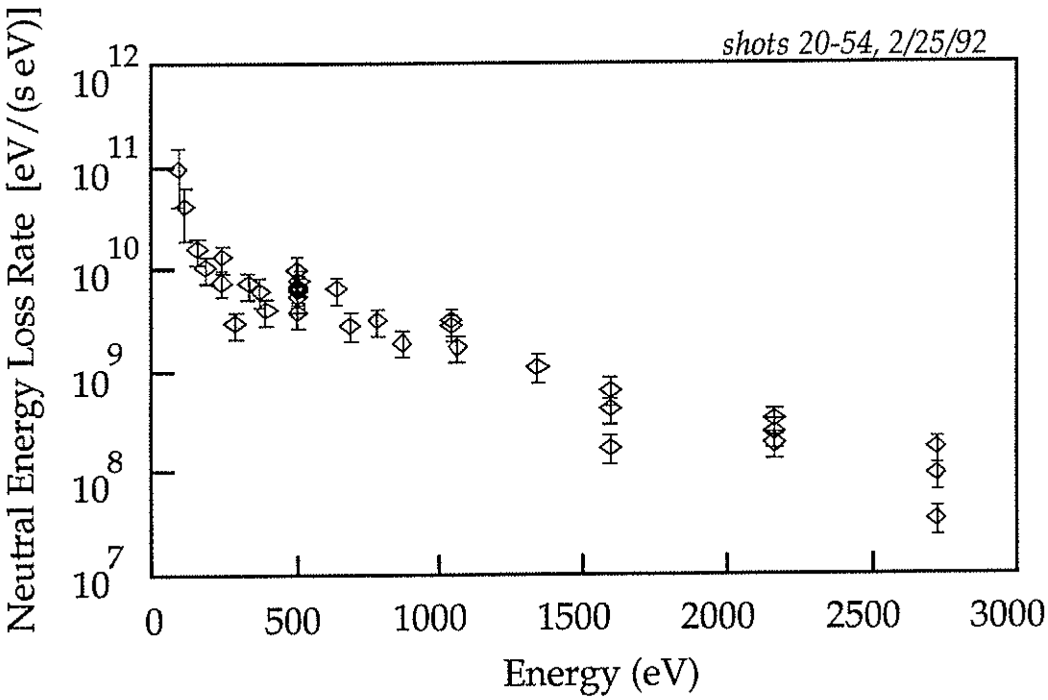

Figure 5.3.3 *Ensemble averaged neutral flux spectrum 20.0 ms into the discharges - low energy points have larger error due to larger uncertainty in the nitrogen stripping cross section at very low energies.*

Using the limiting cases of an optically thick (considerable neutral attenuation) and an optically thin (no neutral attenuation) plasma, upper and lower bounds for the total charge exchange power loss can be calculated from a single FCCXA central chord measurement, F(E). In the optically thick case. the emission from a source within the plasma is the least attenuated if it exits radially (a radial path is the shortest distance to the edge). Assuming then that all of the neutral emission is radial, the conversion to the total flux at a particular energy, H(E), is (see figure 5.3.4 for geometry),

$$H(E) = 4\pi^2 aR_o\, F(E)\, E/A_s\,,$$

where $A_s = 2.8\ \text{cm}^2$. This is a lower bound for the total charge exchange loss.

In the optically thin case, the neutral emission is more isotropic at the plasma surface. Thus, the FCCXA only measures a fraction of the neutral emission that passes through the collimation of the FCCXA (Fig. 5.3.4). The conversion to the total flux at particular energy becomes,

$$H(E) = (4\pi^2 aR_o\, F(E)\, E/A_s)\,(2\pi/\Omega_c),$$

where $\Omega_c = A/d^2 = 0.18/9159 = 2.0 \times 10^{-5}$ sr. This is an upper bound for the total charge exchange power loss.

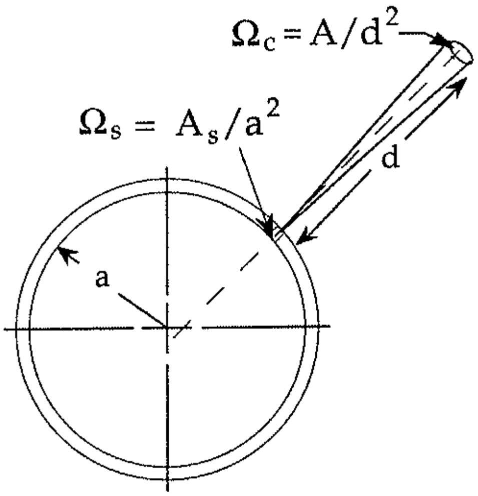

Figure 5.3.4 *Geometry used for total charge exchange loss calculations. "A" is the area subtended by the spectrometer slits.*

The total charge exchange power loss (93 to 2731 eV) for each case is shown versus time in figure 5.5.5. The lower bound obtained for the total charge exchange power loss is less than 1 Watt. In the upper bound case, the total charge exchange power is still less than 2% of the total input power (Fig. 5.4.1). It is possible that significant charge exchange power is lost by the plasmas at energies below 100 eV. This power is undetectable by the charge exchange analyzer because the nitrogen stripping cross section is extremely small for such low energy neutrals (Fig. 3.4.1). However, NEUCG[12] code calculations for a MST discharge with parabolic temperature and density profiles indicate that only 20-30% of the neutral emission along a central chord exits via low energy, less than 100 eV, neutrals.

The upper bound calculation also assumes that the neutral flux emission is toroidally symmetric. Regions of higher neutral density may exist near the MST fueling valves and it is possible that neutral losses are enhanced in those regions. For these particular experiments, the valves were shut at the start of the discharge. After 20 or 30 ms it is unlikely that large toroidal asymmetries in the edge neutral density could still exist in these discharges and the upper bound charge exchange power loss changes only slightly throughout the discharge (Fig. 5.3.4).

The small amount of measured charge exchange power loss (even if the CXA measured value is too low by a factor of 2) is supported by the results of bolometer measurements on hydrogen and helium plasmas. The bolometer is sensitive to neutral particles. If charge exchange is a significant loss mechanism for MST discharges, it is expected that the bolometer signal would be lower for helium than for hydrogen: production of energetic neutral helium atoms requires two successive charge exchange events, hydrogen only one. In fact, there is no significant difference between the bolometer signal levels for helium and hydrogen plasmas in MST.[13] It should be noted, however, that helium plasmas radiate more strongly than hydrogen plasmas and a drop in charge exchange loss could be obscured by an increase in the radiated power.

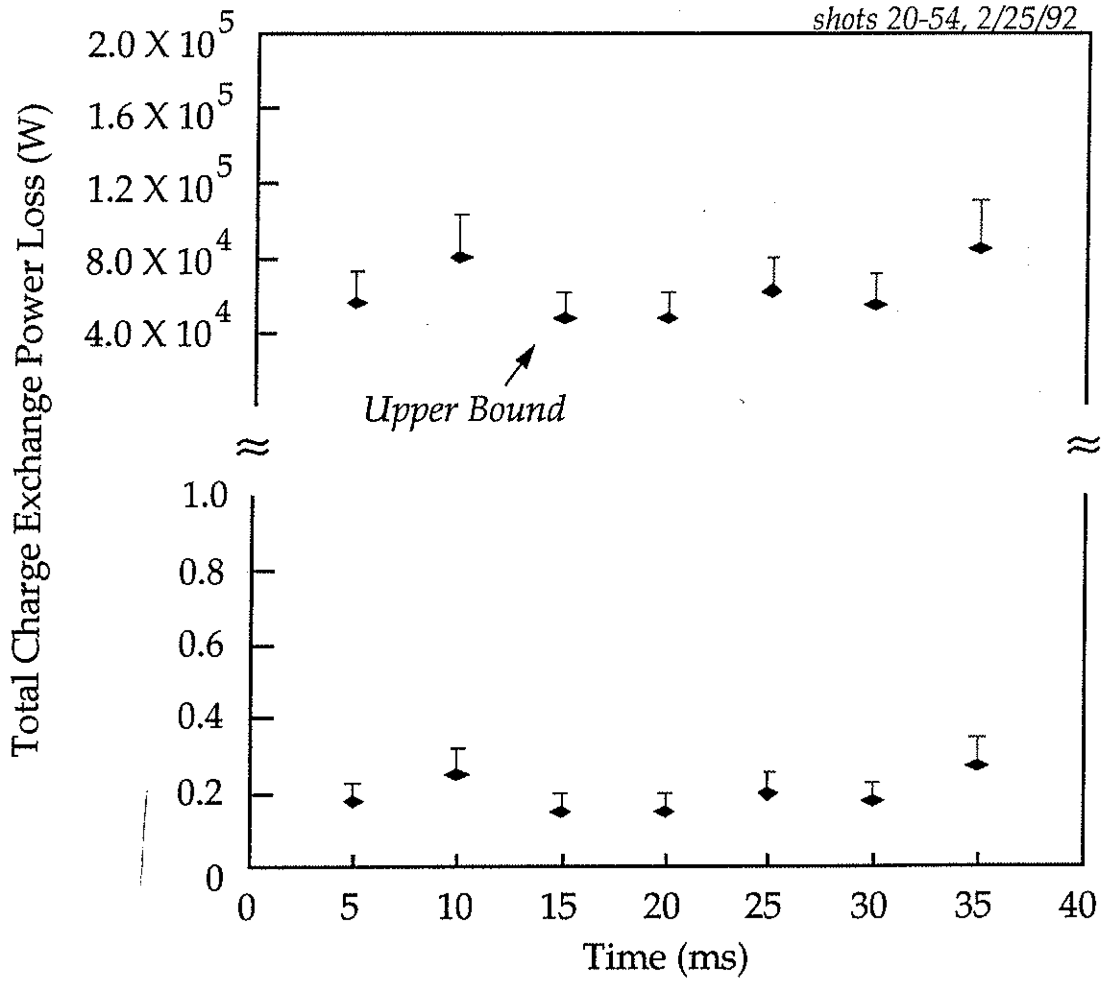

Figure 5.3.4 *Ensemble averaged charge exchange power loss from 93 to 2731 eV. Single sided 30% error bars represent additional contribution to total power loss due to neutrals with energy below 100 eV.*

5.4 Time dependent power balance calculations.

Typically the total power flowing into a plasma is obtained from measurements of the plasma current and the toroidal voltage. For MST, the measured toroidal voltage is converted into the Ohmic driving voltage by using model profiles from the Polynomial Function Model[14] (PFM) that account for the 'twistedness' of the current path. The mutual inductance of the magnetic field circuits and the effects of the changing plasma current, (dI/dt), are also taken into account. The product of the Ohmic driving voltage and the plasma current is the total input, Ohmic, power and is displayed in figure 5.4.1 for the same discharges used in previous figures. The input power calculation is most reliable at peak current as dI/dt is zero. Other than Ohmic electron heating, other energy sinks in the plasma include: charge exchange losses (small), ion and electron losses, thermal conduction to the wall, and radiation. The radiated power for this set of discharges was measured with a calibrated bolometer and is also shown in figure 5.4.1. The bolometer is calibrated for a particular emission profile and the calibration is not valid during the formation phase of the discharge (the first few milliseconds).[15]

Using the measured relative central electron density, electron temperature, and ***assuming*** parabolic temperature and density profiles and a 1 ms electron energy confinement time, τ_{Ee}, the power flowing into the electrons ensembled averaged over the same discharges used in the previous discussion can be calculated (Fig. 5.4.1);

$$\frac{d}{dt}\left(\frac{3}{2}n_eT_e\right) = P_{in} - P_{losses} \,.$$

The equilibrium condition,

$$\tau_{Ee} << \frac{n_eT_e}{\frac{d}{dt}(n_eT_e)}$$

is satisfied after the first 10 ms of these discharges. In equilibrium,

$$0 = P_E - \frac{\frac{3}{2}n_eT_e}{\tau_{Ee}} \,.$$

Integrating over the plasma volume,

$$P_E \approx \int_0^a \frac{\frac{3}{2}n_{eo}T_{eo}}{\tau_{Ee}}\left(1 - \left(\frac{r}{a}\right)^2\right)^2 4\pi^2R_o r dr \;,$$

$$P_E \approx (6.4 \times 10^{-10} \frac{\mathrm{J\,cm^3}}{\mathrm{s\,eV}}) n_{eo} T_{eo} \; .$$

Because the Thomson scattering diagnostic was not density calibrated, a central density of 1.0 X 10^{13} $\mathrm{cm^{-3}}$ at 3 ms was assumed to generate the electron heating power curve in figure 5.4.1. Assuming quasi-neutrality and quasi-equilibrium, a similar equation for the ion heating power was used to generate the ion heating power curve in figure 5.4.1.

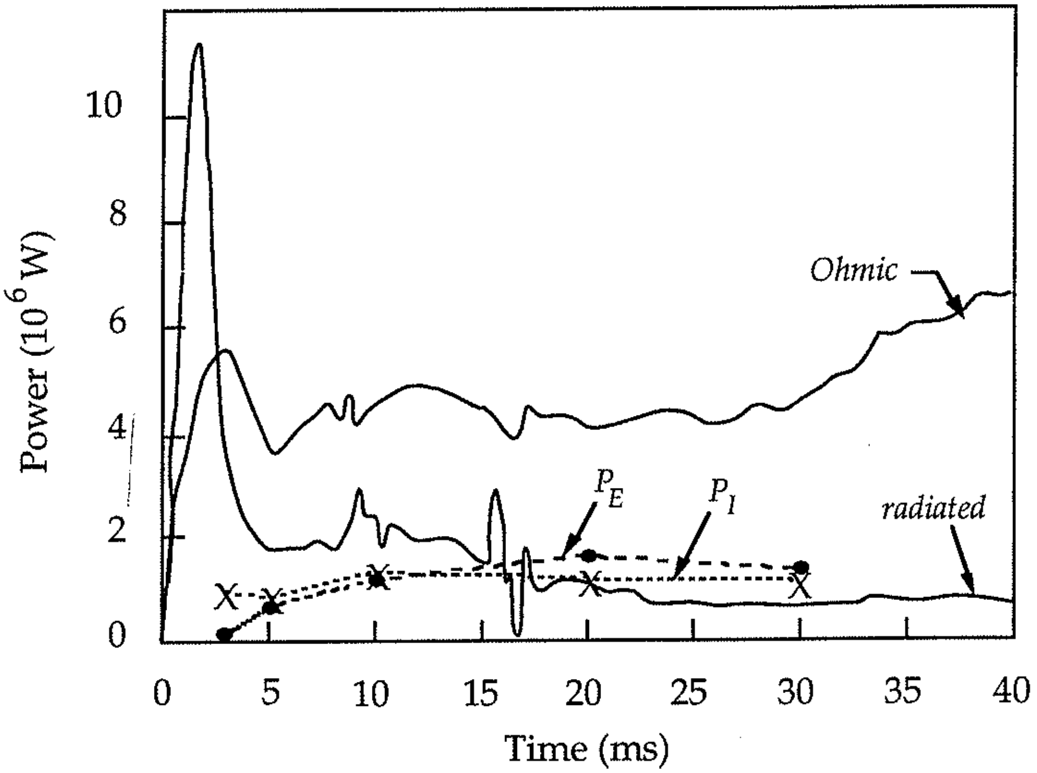

Figure 5.4.1 *Ensemble averaged Ohmic power, radiated power, electron heating power (solid circles), and ion heating power (crosses).*

Figure 5.4.1 suggests that if a 1 ms energy confinement time is assumed for the ions and electrons, the power transported by the ions and electrons and emitted as radiation balances all of the power flowing into the plasma. These calculations are strongly dependent upon the profile and energy confinement assumptions. For example, a perfectly flat density and electron temperature profile would increase the energy stored by the electrons by a factor of 3. Similarly, an electron energy confinement time of 0.2 ms could account for all of the Ohmic power via electron heating power requirements.

5.5 Comparison with expectations based on collisional ion heating.

Based on the results of the section 5.4, it appears that enough excess energy is available in the plasma to account for the observed ion temperature. If the energy is transferred to the ions from the electrons by classical ion-electron collisions, the expected central ion temperature can be calculated from a simple energy balance equation (all plasma parameters used are *central* values),

$$\frac{d}{dt}\left(\frac{3}{2}n_iT_i\right) = -n_i\nu_E^{i/e}\,(T_e - T_i) - \frac{\frac{3}{2}n_iT_i}{\tau_{Ei}}, \qquad (5.1)$$

$$\nu_E^{i/e} = \left(\frac{m_i}{m_e}\right)\left[\frac{4}{\sqrt{\pi}}\nu_0^{i/e}\right],$$

$$\nu_E^{i/e} \approx 7.5 \times 10^{-8}\left(\frac{n_e}{T_e^{3/2}}\right)\ s^{-1},$$

where ν_o is the ion-electron collision frequency.[16] If $T_i << T_e$ the energy balance equation can be written as a simple integral,

$$T_i = \int_{t1}^{t2} \left[\, 7.5 \times 10^{-8}\left(\frac{n_en_i(T_e - T_i)}{T_e^{3/2}}\right) - \frac{3n_i\,T_i}{2\tau_{Ei}}\right]dt\ + T_{io}\,.$$

The results of using the measured T_e and relative n_e (n_e = 1.0 X 10^{13} cm^{-3} at t = 3 ms assumed again) to step through this integral are shown in figure 5.5.1 for a range of ion energy confinement times, 1 - 10 ms. The ion temperature quickly rises up to the electron temperature until the electron temperature levels off, and then losses overcome the collisional heating (Fig. 5.2.4 and Fig. 5.5.1). From the data presented in section 5.2 it is clear that $T_i \approx T_e$, and early in the discharge $T_i > T_e$. Therefore, it is not surprising that this expression cannot accurately reproduce the measured ion temperatures.

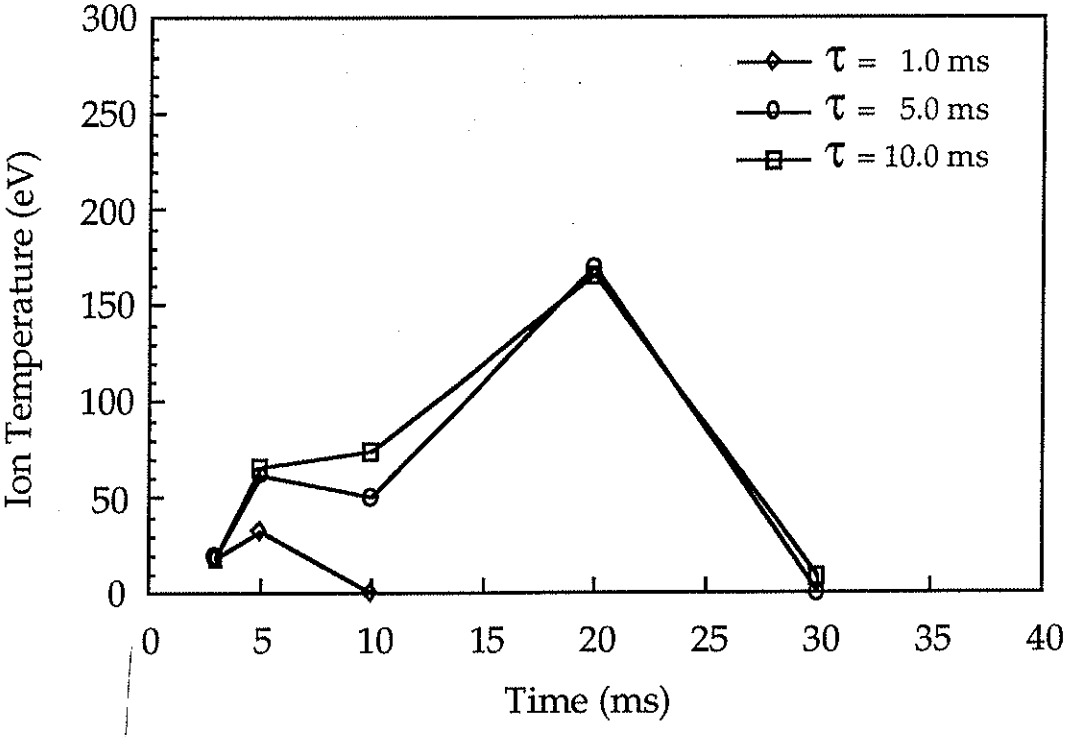

Figure 5.5.1 *Expected central ion temperature evolution for a non-equilibrium plasma using measured central electron temperatures and relative electron densities.*

Since the ion temperature and density, assuming constant Z_{eff} (average charge of the ions), is actually quite stable throughout the discharge (Fig. 5.2.4), some quasi-equilibrium must exist. In equilibrium equation 5.1 becomes

$$T_i = 7.5 \times 10^{-8} \left(\frac{n_e}{\sqrt{T_e}\,[7.5 \times 10^{-8} \frac{n_e}{T_e^{3/2}} + \frac{3}{2\tau_{Ei}}]} \right) . \qquad (5.2)$$

Stepping through time using this expression and the measured electron temperatures and densities figure 5.5.2 is obtained. To reproduce the measured ion temperature at 20 ms, a central density of 5×10^{13} cm^{-3} and an ion energy confinement of 10 ms is required. Although no density measurements were available for these discharges, central densities of 5×10^{13} cm^{-3} have never been obtained in the MST. Operational experience, based on the fueling levels, Thomson scattering signal levels, and neutral flux emission, suggests that a central electron density of $1\text{-}2 \times 10^{13}$ cm^{-3} is more appropriate. A ion energy confinement time of 1 ms is in agreement with calculations of the electron energy confinement time[17] and calculations of the ion energy confinement time based on measurements of the decay rate of the ion temperature after ion heating bursts (see section 7.2). A confinement time of 10 ms is beyond reasonable expectations for the MST.

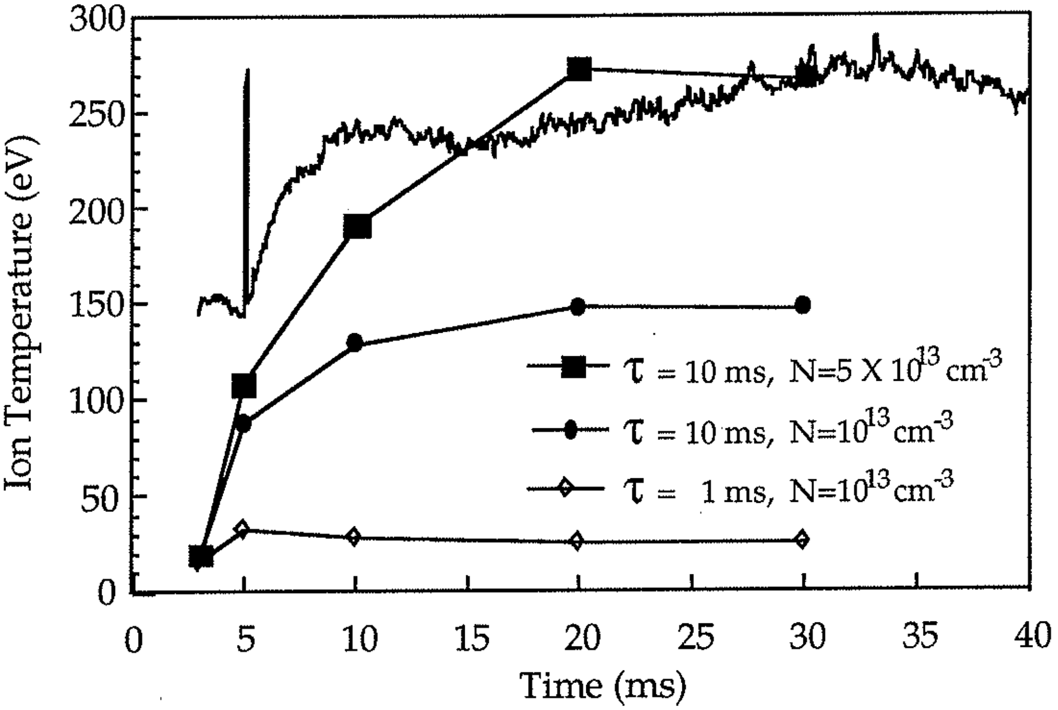

Figure 5.5.2 *Expected central ion temperature evolution for a quasi-equilibrium plasma using measured central electron temperatures and densities.*

Neither of these two equations (5.1 and 5.2) can explain the early time $T_i > T_e$. Energy flowing from the colder electrons to the hotter ions would violate the Second Law of Thermodynamics and both equations include only classical collisional energy transfer via Coulomb collisions. These results unquestionably corroborate the non-collisional character of ion heating in the RFP as reported by other experiments.[5,18-20] It is possible that some non-collisional mechanism exists that can transfer energy from the electrons to the ions in excess of collisional transfer rates. Nevertheless, $T_i > T_e$ is compelling evidence that energy is flowing from the external circuit into the ions, bypassing the electrons.

References

[1] S. H. Hamberger, J. Jancarik, L. E. Sharp, D. A. Aldcroft, and A. Wetherell, *'Experiments on Plasma Heating by the Dissipation of Current-Driven Turbulence,'* in Plasma Physics and Controlled Nuclear Fusion Research (International Atomic Energy Agency, Vienna, 1971), Vol. II, 37.

[2] see for example, F. F. Chen, Introduction to Plasma Physics and Controlled Fusion (Plenum Press, New York 1984) pp. 225-274.

[3] Robert B. Howell, and Yoshio Nagayama,' *Ion energy measurements on a reversed-field pinch experiment using Doppler broadening,'* Phys. Fluids **28**, 734 (1985).

[4] T. Fujita, K. Saito, J. Matusi, Y. Kamada, H. Morimoto, Z. Yoshida, and N. Inoue,*'Anomalous Ion Heating in Repute-1 Ultra-Low q and Reversed Field Pinch Plasmas,' Nucl. Fusion* **31**, 3 (1991).

[5] G. A. Wurden, P. G. Weber, K. F. Schoenberg, A. E. Schofield, J. A. Phillips, C. P. Munson, G. Miller, J. C. Ingraham, R. B. Howell, J. N. Downing, R. R. Chrien, T. E. Cayton, L. C. Burkhardt, R. J. Bastasz, S. E. Walker, A. M. Prezler, P. G. Carolan, and C. A. Bunting, *'Ion heating studies in the ZT-40M Reversed Field Pinch'*, in Proceedings of the 15th European Conference on Controlled Fusion and Plasma Physics, Dubrovnik (European Physical Society, 1988), 533.

[6] Roger D. Bengtson, K. W. Gentle, J. Jancarik, S. S. Medley, P. Nielsen, and P. Phillips, *'Observations of plasma heating in a turbulent torus,'* Phys. Fluids **18**, 710 (1975).

[7] R. M. Mayo and L. S. Kirschenbaum, *'Neutral particle energy analysis and charge exchange power loss in edge-dominated spheromaks,'* Phys. Fluids B **3**, 2096 (1991).

[8] H. De Kluiver, H. W. Piekaar, W. R. Rutgers, H. Schrijver, B. De Groot, *'Turbulent Heating of a Plasma Column in a Linear Discharge,'* in Plasma Physics and Controlled Nuclear Fusion Research (International Atomic Energy Agency, Vienna, 1971), Vol. II, 67.

[9] S. Q. Mah, H. M. Skarsgard, and A. R. Strilchuk, *'Current-Induced Ion Heating in a Toroidal Plasma,'* Phy. Rev. Lett. **25**, 1409 (1970).

[10] Ray Fonck, private communication.

[11] Sam Hokin, University of Wisconsin - Madison, PLP 1048.

[12] K. H. Burrell, J. Comp. Physics 27, **88** (1978).

[13] Daniel Den Hartog, private communication.

[14] J. C. Sprott, *'Polynomial Function Model for Reversed Field Pinches,'* Phys. Fluids **31**, 2266 (1988).

[15] Michael Cudzinovik, University of Wisconsin - Madison, PLP 1080.

[16] David L. Book, *NRL Plasma Formulary*, (Naval Research Laboratory, Washington D.C., 1987) pp. 31-34.

[17] D. J. Den Hartog, *'An Energy Confinement Study of the MST Reversed Field Pinch using a Thomson Scattering Diagnostic,'* Ph. D. Thesis, University of Wisconsin-Madison (1989).

[18] Robert B. Howell, and Yoshio Nagayama,*' Ion energy measurements on a reversed-field pinch experiment using Doppler broadening,'* Phys. Fluids **28**, 734 (1985).

[19] T. Fujita, K. Saito, J. Matusi, Y. Kamada, H. Morimoto, Z. Yoshida, and N. Inoue,*'Anomalous Ion Heating in Repute-1 Ultra-Low q and Reversed Field Pinch Plasmas,' Nucl. Fusion* **31**, 3 (1991).

[20] P. G. Carolan, A. R. Field, A. Lazaros, M. G. Rusbridge, H. Y. W. Tsui, and M. V. Bevir, in Proceedings of the 14th European Conference on Controlled Fusion and Plasma Physics, Madrid (European Physical Society, 1987) vol. II, 469.

CHAPTER 6

THE MHD DYNAMO, MAGNETIC ENERGY BALANCE AND HELICITY CONSERVATION IN THE RFP

6.1 The MHD dynamo.

The dynamo effect is defined as the generation of current by the motion of electrical conductors in magnetic fields.[1] In a plasma the moving electrical conductor is the convecting plasma and the generated currents can produce additional magnetic field. As long as energy is supplied to keep the plasma moving, the dynamo effect can enhance an existing magnetic field indefinitely. Intuitively, the energy stored in the plasma flow velocity must eventually be lost through some *dissipative* process. If this energy is lost directly to the ions, the ion temperature of the RFP should be coupled to the level of dynamo activity.

At the start of a typical MST RFP discharge the current in the toroidal

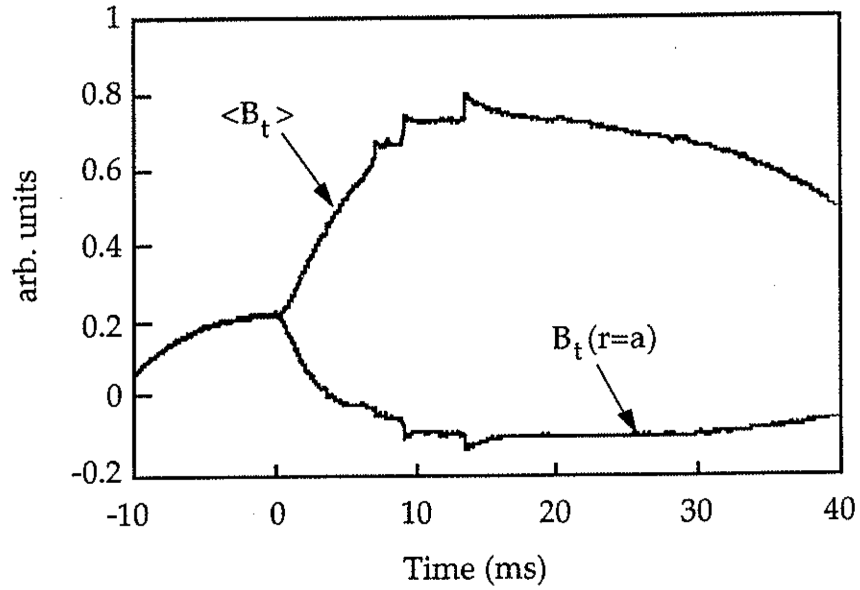

Figure 6.1.1 *Average and edge toroidal field in the MST. The discharge begins at t = 0.*

field coil has already begun to decay, yet after the plasma forms, the average toroidal field increases (Fig. 6.1.1). Therefore, the additional toroidal field must be internally generated. Shortly after the formation of the plasma, the magnetic field at the edge of the vacuum vessel spontaneously reverses direction (Fig. 6.1.1). This sustainment and reversal of the toroidal magnetic field in the RFP is widely believed to be a result of an internal dynamo mechanism. Throughout this thesis, dynamo activity has been and will be defined as the internal generation of toroidal field.

Over the last twenty years a number of theories have been proposed that claim to identify the physical mechanism responsible for the RFP dynamo. These include: the Tangled Discharge model,[2] the MHD dynamo model,[3,4] and the kinetic dynamo model.[5] The MHD dynamo model is an extension of Ohm's law in a plasma to include fluctuations:[6]

$$\vec{E} + \vec{u}\times\vec{B} = \eta\vec{J} + \frac{\vec{J}\times\vec{B} - \nabla P_e}{ne} .$$

Ignoring the diamagnetic term, the Hall effect term, and averaging over many fluctuation periods,

$$\langle\vec{E}\rangle + \langle\vec{u}\times\vec{B}\rangle = \langle\eta\vec{J}\rangle .$$

Assuming each quantity can be described by an equilibrium quantity and a first order fluctuating part, the average of each linear term vanishes and Ohm's law becomes

$$\vec{E}_o + \vec{u}_o\times\vec{B}_o + \langle\tilde{u}\times\tilde{B}\rangle = \eta\vec{J}_o .$$

In the poloidal direction the externally applied electric field is small enough to ignore. Assuming there is no steady-state radial or toroidal flow, the poloidal component of Ohm's law becomes

$$\langle\tilde{u}\times\tilde{B}\rangle_\theta = \langle\tilde{u}_r\times\tilde{B}_t\rangle_\theta + \langle\tilde{u}_t\times\tilde{B}_r\rangle_\theta = \eta\vec{J}_\theta \rightarrow \vec{B}_t .$$

An upper bound for the steady-state radial flow velocity can be estimated by noting that the plasma would need to travel at approximately 20 m/s to move from r/a = 0.5 to the edge during the discharge. Crossing this radial flow with the toroidal field yields a poloidal current which is comparable to the equilibrium poloidal current. However, the toroidal field vanishes at the reversal surface and the poloidal current is still a few hundred kA/m^2. This suggests that the steady-state, radial plasma flow contribution to the poloidal current is negligible. The toroidal flow is estimated to be 300 m/s or less[7] and is crossed into a very small, if not zero, steady-state radial magnetic field.

So in this MHD model, the large equilibrium poloidal current, and thus the equilibrium toroidal field, must arise from correlated flow velocity and magnetic field fluctuations. As long as the flow and magnetic field fluctuations continue unabated, toroidal magnetic field can be produced indefinitely.

In a number of extensive numerical simulations the MHD dynamo mechanism has been observed to generate reversed toroidal field and sustain the total toroidal field.[8,9,10] As the plasma in the simulations relaxes to a minimum energy state similar to the predictions of the Taylor model,[6,11] tearing mode instabilities develop.[6] These instabilities supply the flow and magnetic fluctuations needed to drive the dynamo action. Unfortunately, experimental evidence that the MHD dynamo is responsible for toroidal field sustainment in laboratory plasmas is difficult to obtain. Simultaneous measurements of flow velocity and magnetic field fluctuations must be made, and the relative phase of the fluctuations determined. It is hoped that in the next few years a diagnostic capable of measuring the flow velocity of impurity ions in the MST will be completed. It is unclear, however, that measurement of impurity flows will provide sufficient information to confirm or refute the MHD dynamo picture.

Although Rusbridge's Tangled Discharge model is often cited as an example of the important role resistivity can play in the alteration of magnetic topology,[6] the model's predictions of reversal and pinch parameter are at considerable odds with experiment.[6]

The flow of energetic electrons along stochastically wandering magnetic field lines in the RFP forms the foundation of the kinetic dynamo model. The existence of these supra-thermal electrons in the RFP edge has been investigated during recent experiments in the MST.[12] Preliminary results indicate that the average energy of the supra-thermal edge electrons is smaller than previously thought, making them more collisionally coupled to the plasma.[13] The original kinetic dynamo model required very non-collisional, very hot, electrons to transfer momentum, current, from the core to the plasma edge.[5] At the lower energies, the electrons can no longer easily travel from the core to the edge.[13] Recently it has been hypothesized that the MHD dynamo induced magnetic fluctuations may produce the supra-thermal electrons near the reversal surface, which then carry the current needed to sustain the toroidal magnetic field.[14] Such a scenario would couple the kinetic and MHD effects emphasized by each model.

At this time the most plausible mechanism for toroidal field sustainment and reversal in the RFP is the MHD dynamo. The required fluctuation level also provides a vehicle for the energy relaxation process needed by Taylor's minimum energy state paradigm. If the fluctuation energy is lost directly to the ions, the ion temperature of the RFP should be coupled to the fluctuations, and thereby to the level of dynamo activity.

6.2 Magnetic energy balance and helicity conservation in the RFP.

The role of fluctuations in the magnetic energy balance of the RFP is illustrative of the relationship between external parameters and internal fluctuations in the RFP. Assuming a steady state plasma and magnetic energy conservation

$$\langle \dot{W} \rangle = \frac{d}{dt}\int_V \langle \frac{B^2}{2\mu_o} \rangle \, d^3x = 0 \, ,$$

the conservation equation can be divided into volume and surface integrals,

$$= -\int_V \langle \vec{E} \cdot \vec{J} \rangle \, d^3x \;-\frac{1}{\mu_o}\int_S \langle \vec{E} \times \vec{B} \rangle \, d\vec{S} \;-\int_{V_b} \nabla\chi_o \cdot \vec{J}_o \, d^3x \;.$$

resistive losses *surface losses* *losses via non-zero surface potentials* (χ)

In terms of equilibrium and fluctuating quantities this becomes

$$0 = V_\phi I_\phi - V_\theta I_\theta - \int_V \vec{E}_o \cdot \vec{J}_o \, d^3x \;-\int_V \langle \tilde{E} \cdot \tilde{J} \rangle \, d^3x \;-\frac{1}{\mu_o}\int_S \langle \tilde{E} \cdot \tilde{B} \rangle \cdot d\vec{S} \;.$$

Assuming the equilibrium flow vanishes, the fluid momentum equation is given by

$$\int_V \rho \frac{d}{dt}\langle \frac{\tilde{u}^2}{2} \rangle \, d^3x = \int_V \langle \tilde{J} \times \vec{B}_o \cdot \tilde{u} \rangle \, d^3x + \int_V \langle \vec{J}_o \times \tilde{B} \cdot \tilde{u} \rangle \, d^3x - \int_V \langle \nabla P \cdot \tilde{u} \rangle d^3x$$
$$- [\text{ dissipative losses}].$$

Using Ohm's law including fluctuations, assuming the external poloidal electric field, E_θ, is zero, and ignoring the surface potential term the magnetic energy equation becomes

$$V_\phi I_\phi = \int_V \eta \, \vec{J}_o^{\,2} \, d^3x + \int_V \eta \, \tilde{J}_o^{\,2} \, d^3x + U(r) + [\text{dissipative losses}] \,,$$

$$U(r) = \frac{1}{\mu_o}\int_S \langle \tilde{E} \times \tilde{B} \rangle \cdot d\vec{S} + \int_S \langle \tilde{p} \;\; \tilde{u} \rangle \cdot d\vec{S} \quad ,$$

where U(r) describes the transport of magnetic energy through the plasma surface by the fluctuations and the loss term includes all dissipative processes: viscosity, resonances, etc.

The externally supplied power, $V_\phi I_\phi$, must balance the resistive and fluctuation losses while driving the toroidal current and sustaining the dynamo generated toroidal field (included since the full Ohm's law expression was used). If the ions are heated by fluctuation dissipation, the measured input power should exceed what is required to balance the resistive losses for a particular current. This is exactly what is seen in the results presented in chapter 5. These quantities have also been measured for a number of other RFP's and all have shown a excessive input power requirement, even after corrections for the helical RFP current path and impurities.[15,16,17,18] These large input, Ohmic, powers have reinforced the RFP community's *assumption* that the dissipation of fluctuations is responsible for heating the ions in the RFP. This chain of reasoning is quite compelling, but without direct measurements of correlated ion heating and fluctuations there is not enough information to support this conclusion. *Simultaneous* ion heating and dynamo fluctuation measurements are presented in chapter 7 of this thesis.

The excessive input power requirements of RFP's have also been associated with magnetic helicity dissipation. To constrain his relaxation model for the RFP, Taylor postulated that the global magnetic helicity of a plasma is conserved.[19] Physical interpretations of magnetic helicity abound. In the basest sense, magnetic helicity is a quantification of the knotedness of magnetic flux tubes (figure 6.2.1).

$$K = \int_V \vec{A} \cdot \vec{B} \cdot d^3x$$

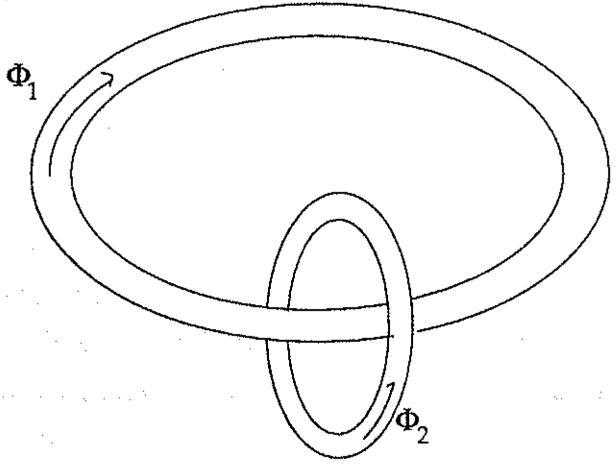

$$K = \Phi_1 \Phi_2$$

Figure 6.2.1 *Linked flux tubes in a plasma.*

If the resistivity of a plasma is zero, helicity is perfectly conserved. For non-zero plasma resistivity the plasma and magnetic field are no longer completely coupled and the magnetic field can diffuse and also "tear" in relation to the plasma.[20] This tearing dissipates helicity. Taylor postulated that on a local scale helicity is not conserved in the RFP, but that the total helicity is conserved for a plasma in a perfectly conducting shell. The gauge invariant global helicity of a toroidal plasma is given by

$$K = \int_V \vec{A} \cdot \vec{B} \cdot d^3x \;\; - \int_C \vec{A} \cdot \; d\alpha \int_C \vec{A} \; d\beta \quad ,$$

where the second term is the product of the toroidal flux and the poloidal flux passing the hole in the center of the torus. After considerable algebra, an equation similar to the energy balance equation can be written for the global helicity balance,

$$V_\phi \Phi_\phi = \int_V \eta \, \vec{J}_o \cdot \vec{B}_o \, d^3x \; + H(r) + \int_S \chi \cdot \vec{B}_o \, d\vec{S} \quad ,$$

$$H(r) = \langle \widetilde{\Phi}_\theta \widetilde{\Phi}_\phi \rangle + \frac{1}{2} \int_S \langle \widetilde{A}' \times \dot{\widetilde{A}} \rangle \cdot d\vec{S} \; + \int_S \langle \widetilde{\chi} \; \widetilde{B} \rangle \cdot d\vec{S} \quad ,$$

where H(r) is the loss of helicity through the plasma surface due to fluctuations and is identically zero if the plasma is bounded by a perfectly conducting shell. The first term is the resistive dissipation of helicity. The third term quantifies the helicity losses due to magnetic field lines passing through obstructions with an electric potential between the point of entry and exit of the field line. For a given toroidal flux the loop voltage must balance resistive helicity dissipation and this obstruction loss term. Some RFP's have reported increases in loop voltage when limiters or tiles are inserted in the plasma edge.[21,22]

But how is helicity conservation relevant to ion heating? A comparison of the magnetic energy and helicity equations yields an interesting relationship. For a given plasma current and magnetic field, the loop voltage must increase if helicity dissipation is increased through insertion of a limiter or some other obstruction into the plasma. The additional loop voltage increases the power input to the plasma and to maintain the energy balance the plasma must self-consistently increase the level of energy dissipation:

$$\text{losses} = \frac{I_\phi}{\Phi_\phi}\left(\int_V \eta\,\vec{J}_o\cdot\vec{B}_o\,d^3x + \int_S \chi\cdot\vec{B}_o\,d\vec{S}\right) - \int_V \left(\eta\,\vec{J}_o^{\,2} + \eta\,\tilde{J}_o^{\,2}\right) d^3x\ .$$

Assuming that fluctuation dissipation heats the ions, these statements imply that both the loop voltage and ion heating should increase if extra helicity is dissipated. In fact, HBTX reported an ion temperature increases after insertion of a graphite paddle in the plasma edge.[21] It should be noted, however, that using the same paddle in a similar experiment ZT-40 saw an increase in the loop voltage but no increase in the ion temperature.[22]

In order to investigate whether fluctuations, specifically dynamo fluctuations, are responsible for the ion heating in the RFP, ion temperatures and dynamo fluctuations were simultaneously measured in the MST. The question of the identity of the physical mechanism that transfers the fluctuation energy to the ions has only been seriously addressed by recent RFP ion heating models.[22] Some attempt has been made to discern how the ions get their energy in the MST and the experimental results, along with a short theory discussion, are presented in Chapter 7.

References

[1] H. R. Strauss, *'The dynamo effect in fusion plasmas'*, Phys. Fluids **28**, 2786 (1985).

[2] M. G. Rusbridge, *'A model of field reversal in the diffuse pinch,'* Plasma Phys. **19**, 499 (1977).

[3] C. G. Gimblett and M. W. Watkins, in Controlled Fusion and Plasma Physics (Proc. 7th Europ. Conf. Lausanne, 1975) Vol. 1 (1975) 103.

[4] A. Bhattacharjee and Eliexer Hameiri, *'Self-Consistent Dynamolike Activity in Turbulent Plasma,'* Phy. Rev. Lett. **57**, 206 (1986).

[5] Abram R. Jacobson and Ronald W. Moses, *'Nonlocal dc electrical conductivity of a Lorentz plasma in a stochastic magnetic field,'* Phy. Rev. A. **29**, 3335 (1984).

[6] H. A. Bodin and A. A. Newton, 'Reversed-*Field-Pinch Research,'* Nuclear Fusion **20**, 1255 (1980).

[7] private communication, Daniel Den Hartog.

[8] E. J. Caramana, R. A. Nebel and D. D.. Schnack, *'Nonlinear, single-helicity magnetic reconnection in the reversed-field pinch,'* Phys. Fluids **26**, 1305 (1983).

[9] R. A. Nebel, E. J. Caramana and D. D. Schnack, *'The role of m=0 modal components in the reversed-field pinch dynamo effect in the single fluid magnetohydrodynamics model,'* Phys. Fluids B **1**,1671 (1989).

[10] K. Kusano and T. Sato, *'Non-Linear Coupling Effects on the Relaxation Process in the Reversed Field Pinch,'* Nucl. Fus. **27**, 821 (1987).

[11] J. B. Taylor, *'Relaxation and magnetic reconnection in plasmas,'* Rev. Mod. Phys. **58,** 741 (1986).

[12] S. Hokin, et al., *'Global Confinement in the MST Reversed Field Pinch,'* Phys. Fluids B **3**, 2241 (1991).

[13] private communication, Matt Stoneking.

[14] private communication, Sam Hokin and Sergio Ortolani.

[15] P. G. Carolan, A. R. Field, A. Lazaros, M. G. Rusbridge, H. Y. W. Tsui, and M. V. Bevir, in Proceedings of the 14th European Conference on Controlled Fusion and Plasma Physics, Madrid (European Physical Society, 1987) vol. II, 469.

[16] M. Giubbilei, P. Martin, and S. Ortolani, *'A Mechanism for Plasma heating in Driven Relaxing Magnetic Field Configurations,'* Plasma Phys. and Cont. Fusion **32**, 405 (1990).

[17] G. A. Wurden, P. G. Weber, K. F. Schoenberg, A. E. Schofield, J. A. Phillips, C. P. Munson, G. Miller, J. C. Ingraham, R. B. Howell, J. N. Downing, R. R.

Chrien, T. E. Cayton, L. C. Burkhardt, R. J. Bastasz, S. E. Walker, A. M. Prezler, P. G. Carolan, and C. A. Bunting, in Proceedings of the 15th European Conference on Controlled Fusion and Plasma Physics, Dubrovnik (European Physical Society, 1988), 533.

[18] A. Fujisawa, H. Ji, K. Yamagishi, S. Shinohara, H. Toyama, K. Miyamoto, *'Anomalous Ion Temperature and Plasma Resistance Due to MHD Fluctuations in Repute-1 Reversed Field Pinch Plasmas,'* Nucl. Fusion **31**, 1443 (1991).

[19] J. B. Taylor, *'Relaxation of Toroidal Plasma and Generation of Reverse Magnetic Fields,'* Phys. Rev. Lett. **33**, 1139 (1974).

[20] see for example, George Schmidt, Physics of High Temperature Plasmas (Academic Press, New York 1979) pp. 146-150.

[21] B. Alper, H. A. Bodin, C. A. Bunting, P. G. Carolan, J. Cunnane, D. E. Evans, A. R. Field, R. J. Hayden, A. Lazaros, A. A. Newton, P. G. Noonan, A. Patel, H. Y. W. Tsui and P. D. Wilcock, *'Improved confinement in HBTX with removal of tile limiters,'* Plasma Phys. and Contr. Nucl. Fusion **30**, 843 (1988).

[22] P. G. Weber, J. C. Ingraham, R. F. Ellis, G. A Wurden, C. P. Munson, and J. N. Downing, *'Effects of limiters on reversed-field pinch confinement,'* Phys. Fluids B **3**, 1701 (1991).

[22] N. Mattor, P. Terry, S. C. Prager, *'Anomalous Ion Heating from the Dynamo in a Reversed Field Pinch,'* submitted to Phys. Rev. Lett.

CHAPTER 7

FLUCTUATING ION TEMPERATURE MEASUREMENTS

7.1 Ion temperature changes during discrete dynamo activity.

During an individual discharge in the MST, sharp increases in the level of dynamo activity have been observed, described as dynamo bursts in chapters 1 and 2 (Fig. 2.1.3.). Coincident with each dynamo burst, the ion temperature is observed to increase sharply (Fig. 7.1.1). The change in ion temperature was measured with the charge exchange analyzer and corroborated with CV Doppler measurements for a number of discharges (Fig. 7.1.1). The correlation of the dynamo bursts and ion temperature increases appeared in every discharge examined. An expanded view of the dynamo burst at 14 ms in figure 7.1.1 is shown in figure 7.1.2. On both scales there is a clear correlation between the dynamo bursts and the onset of intense ion heating. In the expanded view, both ion temperatures even show the same sharp initial temperature rise just before 14 ms, a short cooling period, and a second increase in temperature as the decay rate of the dynamo burst suddenly slows around 14.25 ms.

The amplitude obtained from each temperature fit (Eq. 3.1.1) of figure 7.1.1 is shown versus time in figure 7.1.3. The fit amplitude (neutral and ion density product) does not demonstrate any correlation with dynamo activity. The frequency spectrum of the 420 eV neutral flux used in figures 7.1.1 through 7.1.3 is shown in figure 7.1.4 and indicates that the neutral flux emission is dominated by low frequency, less than 10 kHz, activity.

The neutral energy spectrum often deviates from a simple Maxwellian during periods of rapid ion temperature change (Fig. 7.1.2) and a clearly non-Maxwellian energy spectrum is shown in figure 7.1.5.

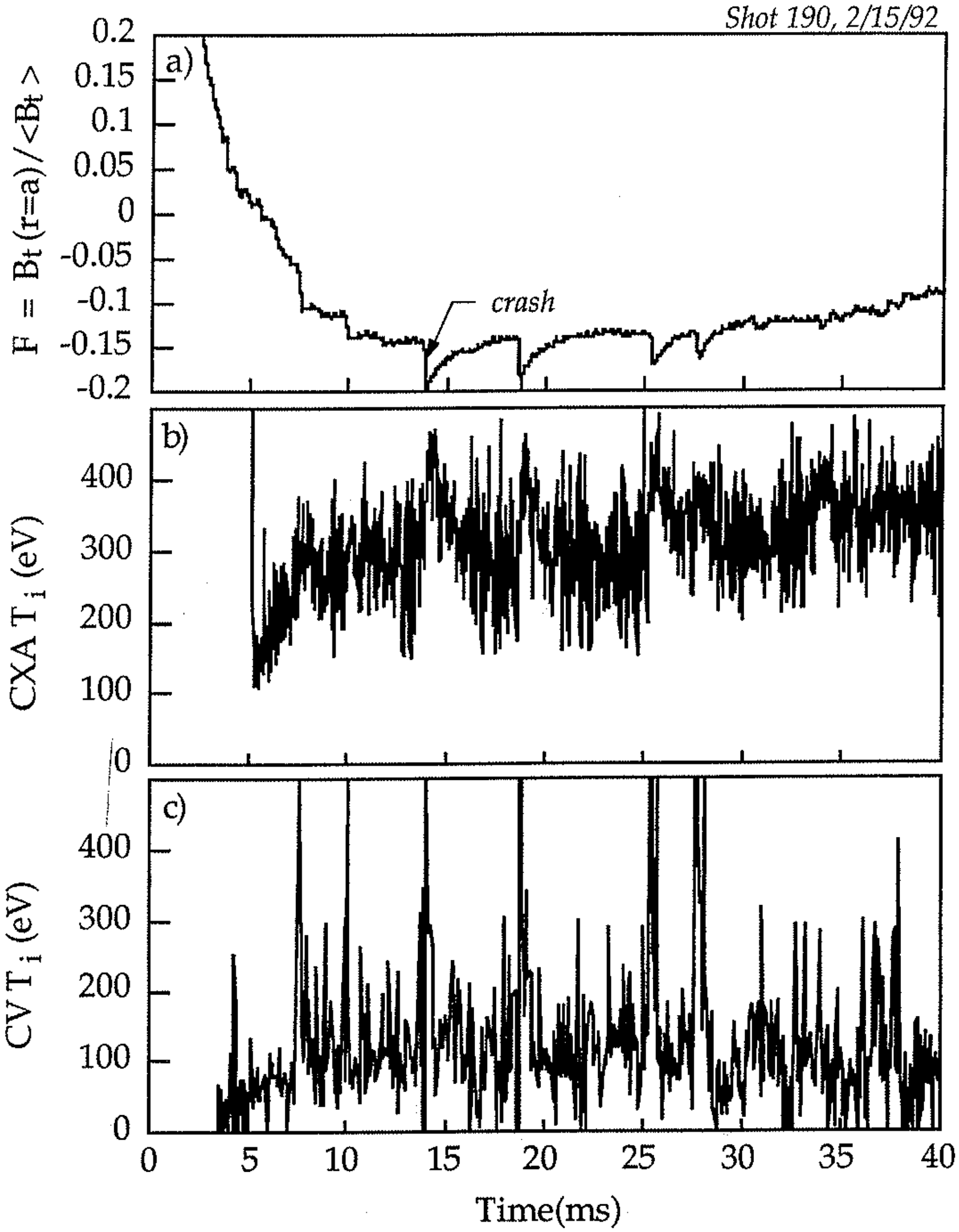

Figure 7.1.1 a) *Reversal parameter b) Charge exchange ion temperature c) Doppler ion temperature.*

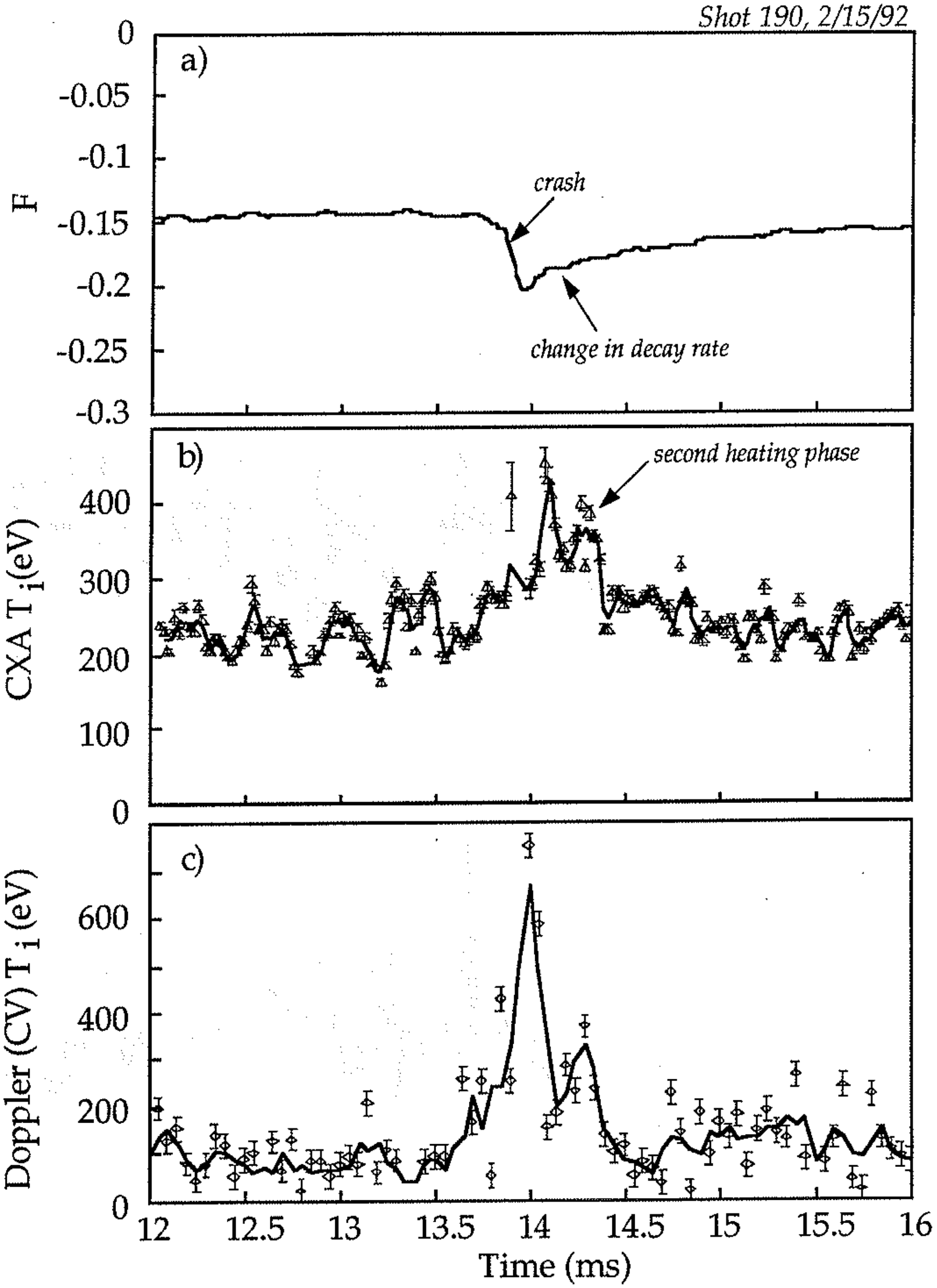

Figure 7.1.2 *Expanded view of the dynamo burst near t = 14 ms for the shot shown in figure 7.2.1* a) *Reversal parameter b) Charge exchange ion temperature c) Doppler ion temperature. Solid lines in (b) and (c) are the same data with 3 point smoothing.*

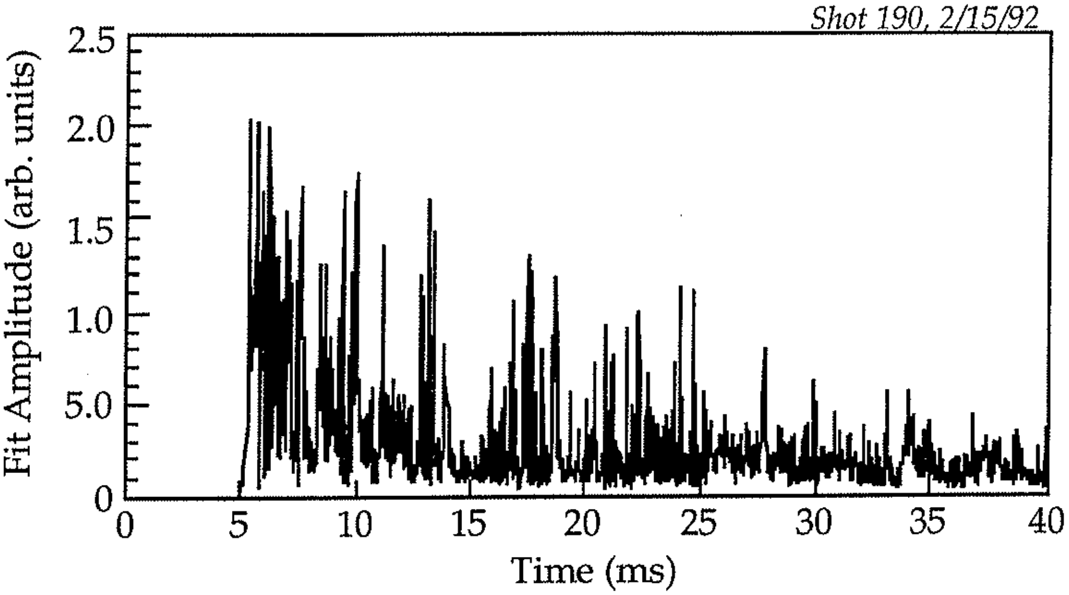

Figure 7.1.3 *Amplitude from temperature fits versus time, no noticeable correlation with dynamo activity.*

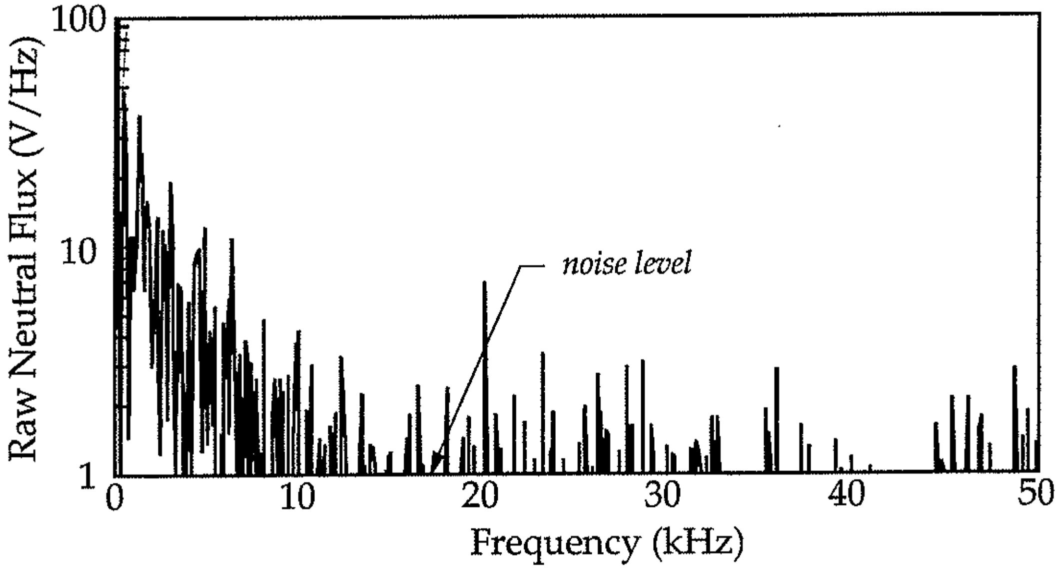

Figure 7.1.4 *Frequency spectrum of raw neutral flux signal. The detector amplifiers have a corner frequency of 50 kHz (section 3.4).*

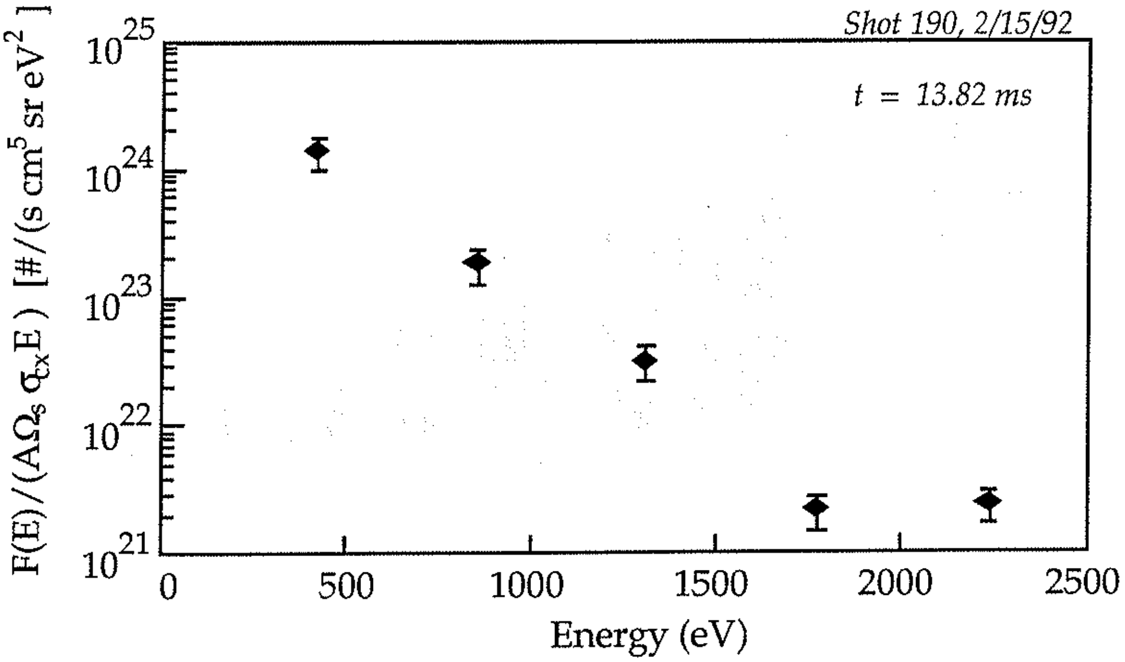

Figure 7.1.5 *Example of a non-Maxwellian neutral energy spectrum during rapid ion heating (t = 13.82 ms in figure 7.1.2).*

7.2 Examination of plasma parameters versus time from dynamo burst crash via a series of identical discharges.

Using the crash phase of a dynamo burst as a reference (Fig. 7.2.1), the single point electron temperature for a series of identical 360 kAmp discharges is plotted versus time from crash in figure 7.2.2-(b) (same discharges as used in chapter 5). When multiple shots fell into the same time bin (when the Thomson scattering firing times were the same length of time away from a dynamo crash), the raw Thomson scattering signals were ensemble averaged to generate a single point electron temperature and density value. This analysis indicates that the electron temperature drops slightly, approximately 25%, just after a dynamo burst, and is relatively constant beforehand. The average toroidal field, also analyzed in the same manner as the Thomson scattering data, is shown in figure 7.2.2-(a) to indicate the ensemble averaged, dynamo burst amplitude versus time from crash.

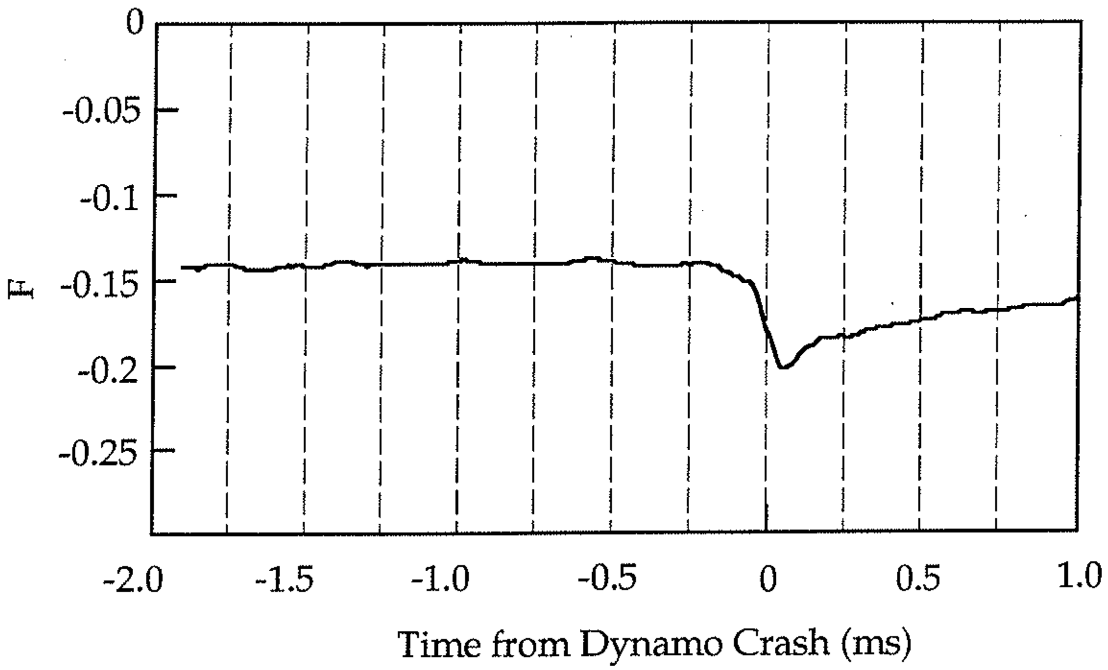

Figure 7.2.2 *a) Average toroidal field b) central ion and electron temperature c) central electron density d) relative central β_0 versus time from dynamo burst crash.*

The charge exchange ion temperatures were analyzed in the same fashion and are displayed in figure 7.2.2-(b) The ion temperature not only increases by more than 50%, it exceeds the electron temperature after the crash of the dynamo burst. The phase and decay rate of the ion temperature relative to the dynamo activity in the toroidal magnetic field is the same as for the single shot data (Fig. 7.1.2). The rise in the ion temperature is clearly correlated with the increase in toroidal magnetic field generation.

Assuming that no additional energy is flowing into the ions during the crash phase of the ion temperature, a rough estimate of the ion energy confinement time can be obtained from the decay rate of the ion temperature (Eq. 5.1). While the central density remains fairly constant (Fig. 7.2.2 - c), the ion temperature falls from approximately 300 eV to 200 eV in 0.5 ms. An exponential fit to the decay yields an **ion energy confinement time** of **1.0 ms**.

The relative central density measured by Thomson scattering rises until the crash and then drops sharply. During one of the brief intervals when an far-infrared interferometer was available on the MST, [2] it was found that the line averaged electron density also decreased during a dynamo burst (Fig. 7.2.3). However, the ratio of line averaged electron density to the relative central density increases by approximately 30% after the dynamo crash (Fig. 7.2.3). This ratio is a rough measure of the flatness of the density profile. The larger the value, the flatter the profile. Therefore, the density profile ***flattens*** just after a dynamo burst. With absolutely calibrated density diagnostics a perfectly flat density profile would have a line averaged to central ratio of 1. It should be noted that the data used for this analysis comes from **two different** experiments. To make a definitive statement about the density profile during dynamo bursts, an experiment with simultaneous Thomson scattering and interferometer density measurements is required.

During relaxation to a minimum energy state in the MHD dynamo model, the current profile of an RFP will flatten because a flat current profile is more stable to the current driven tearing instabilities.[1] If tearing instabilities supply the fluctuations necessary to drive the MHD dynamo, it is conceivable that density profile flattening will accompany the dynamo bursts.

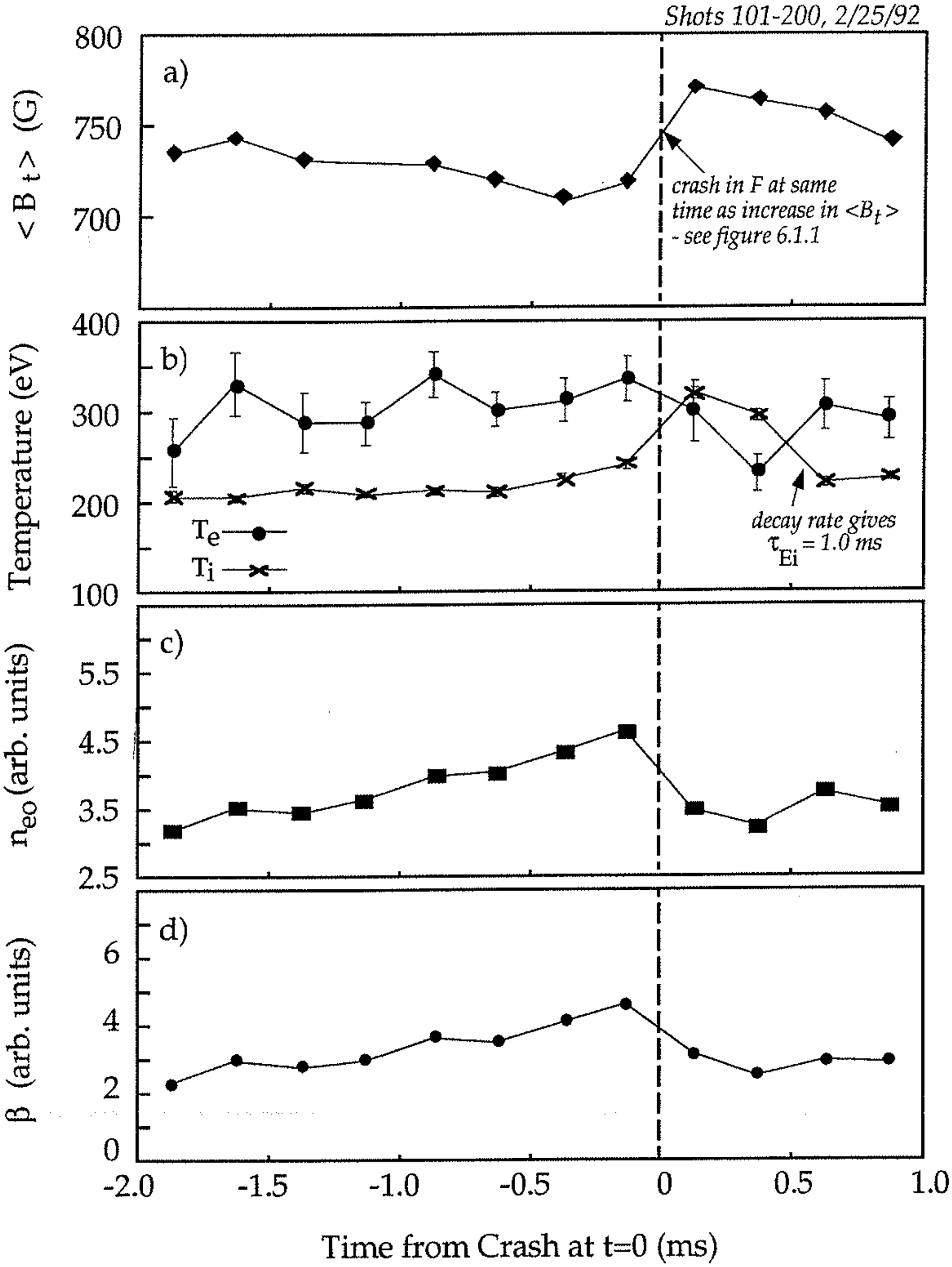

Figure 7.2.2 *a) Average toroidal field b) central ion and electron temperature c) central electron density d) relative central* β_0 *versus time from dynamo burst crash.*

The central, relative plasma pressure, $\beta_o \propto n_o(T_{io} + T_{eo})/B_o^2$, is also plotted versus time from crash in figure 7.2.2-(d). β_o drops sharply, more than 50%, at the dynamo burst crash. It appears that both particle and energy confinement in the core decrease during the dynamo burst, even though the ion temperature increases.

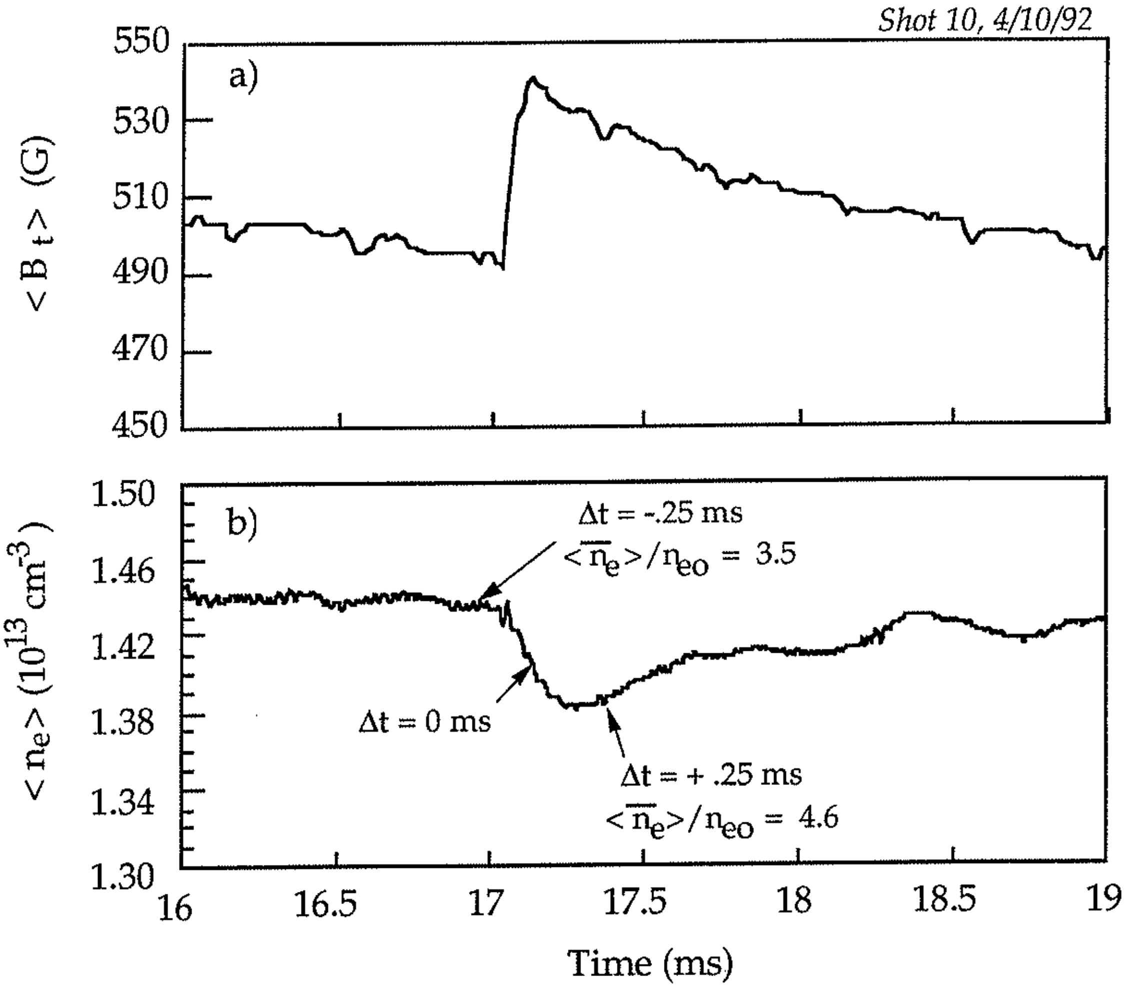

Figure 7.2.3 *a) Average toroidal field b) line averaged electron density from a far-infrared interferometer.*[2] *The ratio of line averaged to relative central density is shown for just before and just after the dynamo burst.*

7.3 Summary of ion heating and dynamo bursts results.

The results presented in sections 7.1-7.2 and chapter 5 clearly indicate that the ion heating process in the RFP cannot be explained by collisional energy transfer from the electrons to the ions. They also confirm the hypothesis that dynamo fluctuations and ion heating are correlated in the RFP. The remaining, and perhaps most important, unanswered question concerning ion heating in RFP's is: what is the physical mechanism that transfers the energy from the external circuit to the ions? If the correlation between the increases in ion temperature and dynamo bursts is assumed to be causal, i.e. the correlation is not coincidental but due to the fact that energy flows from the fluctuations to the ions, the next logical step is to examine the dynamo fluctuations more thoroughly.

Attempts to explain the anomalously high temperatures reported in the early tokamak devices (see section 5.1) focused upon instabilities as possible mechanisms for ion heating. Popular choices were electron cyclotron,[3] ion acoustic,[4] ion cyclotron,[5] and drift wave[6] instabilities. This line of investigation was continued by RFP researchers who examined ion cyclotron instabilities[7] and the viscous damping of turbulent fluctuations[8,9,10] in the RFP.

As it seemed likely that any of these mechanisms could be enhanced during intense dynamo activity, the magnetic fluctuations in the MST were examined over as wide a frequency range as possible. The expectation was that the correlation of a particular instability with ion heating might be determined by studying the magnetic fluctuation power at the instability's characteristic frequency during the dynamo bursts. Most the instabilities listed have high characteristic frequencies, so the first measurements were carried out in the frequency range .1 - 10 GHz. This range includes the electron cyclotron, electron plasma, and ion plasma frequencies for typical MST discharges (Fig. 7.3.1). The very high frequency magnetic fluctuations were measured with an antenna inserted into the plasma edge. The antenna signal was fed into a microwave power diode after being bandpass filtered to eliminate the low frequency fluctuations. The sensitivity of this instrument was approximately 5 X 10^{-7} G at 10 GHz. No measurable emissions were observed in this frequency range. The electron plasma frequency is higher than both the electron cyclotron and ion plasma frequencies in MST, which makes it highly unlikely that emission at either of those frequencies, if it existed, could escape the plasma.

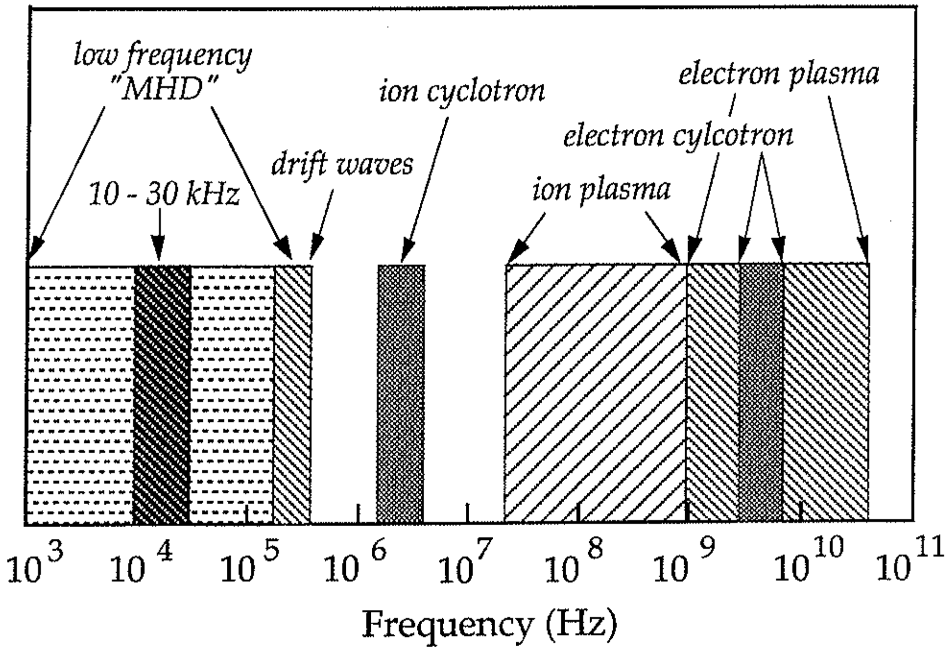

Figure 7.3.1 *Various frequency ranges for 350 kA MST discharges with plasma densities ranging from 1 X* 10^{10} *to 2 X* 10^{13} cm^{-3}.

The low frequency (Fig. 7.3.1), 1 - 250 kHz, magnetic fluctuations have been examined in considerable detail.[11] Their mode structure suggests that they are dominated by tearing instabilities of frequency 10-30 kHz.[11] Tearing mode fluctuations are not expected to directly transfer significant amounts of energy to ions, but they are a source of free energy that can drive other instabilities or wave-particle resonances (see section 7.5).[12] When the magnetic fluctuations in the frequency range 0.5 - 5.0 MHz were examined with the apparatus described in chapter 4, a clear correlation of fluctuation amplitude with the dynamo bursts was observed (Fig. 7.3.2). The fluctuation level begins to rise well before the toroidal field is generated. After the fluctuation level plummets, the toroidal field begins to decay.

The increase in fluctuation amplitude during a dynamo burst is so large that the base fluctuation level had to be attenuated below the 1 bit level of the digitizer to keep the digitizer from saturating. In fact, most dynamo bursts still saturated the digitizer. To successfully measure the high frequency fluctuations during all of the dynamo bursts, a new set of high frequency amplifiers with less gain must be built. The digitizer, a DSP 2001 8-bit digitizer with 32 kilobytes of memory, was operated at a sampling speed of 10 MHz, twice the 5 MHz cutoff of the bandpass filtered amplifiers. At this speed, only 3.2 ms of each discharge could be studied. The technical challenges of magnetic fluctuation measurements in this frequency range severely limited the quantity and quality of the data that could be obtained with the current apparatus.

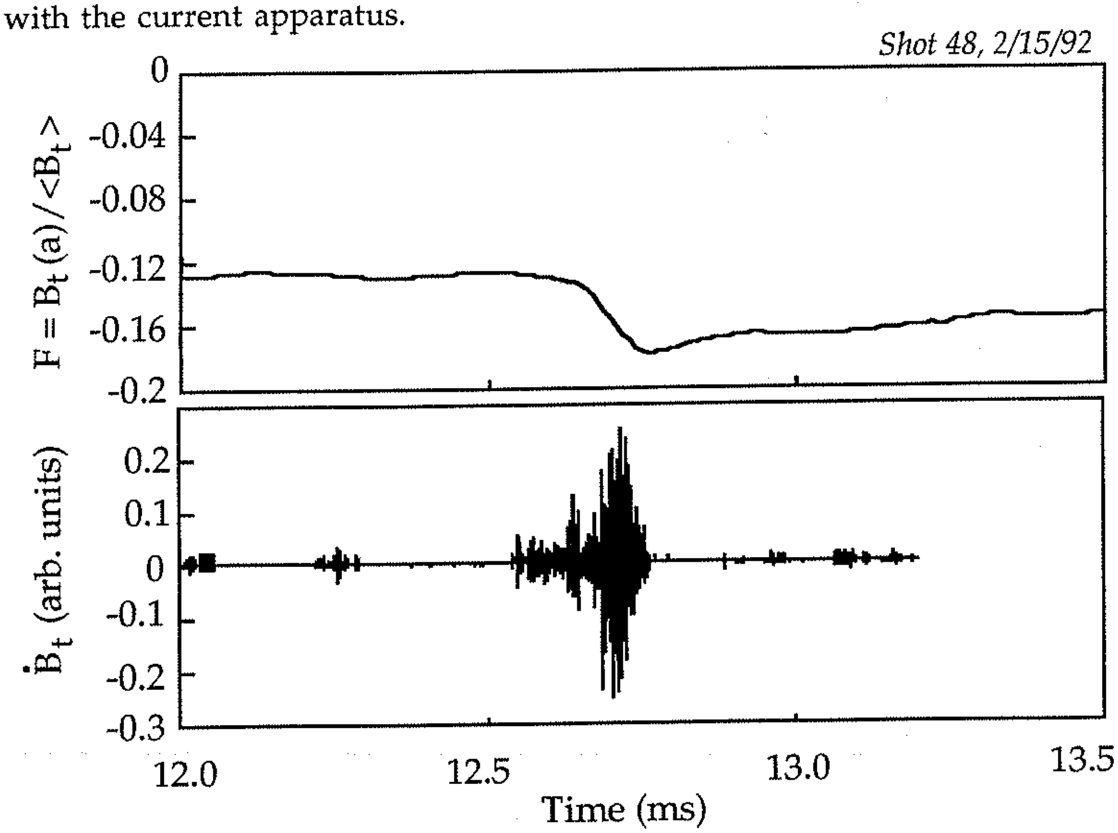

Figure 7.3.2 *Magnetic fluctuations (0.5-5.0 MHz) during a dynamo burst.*

7.4 Magnetic fluctuation power spectra changes during dynamo bursts.

The power spectrum of the 0.5-5.0 MHz magnetic fluctuations was calculated for data records of either 12.8 or 25.6 μs, 128 and 256 points respectively. Each record was preprocessed with a windowing function, usually a Hanning[13] window, to minimize finite record length effects. The built-in discrete fast Fourier transform function of IDL[14] was used to generate the power spectrum. Rather remarkable structures often appear in the power spectra of individual time records. Two of the more dramatic examples are shown in figure 7.4.1; both use the *same* record length.

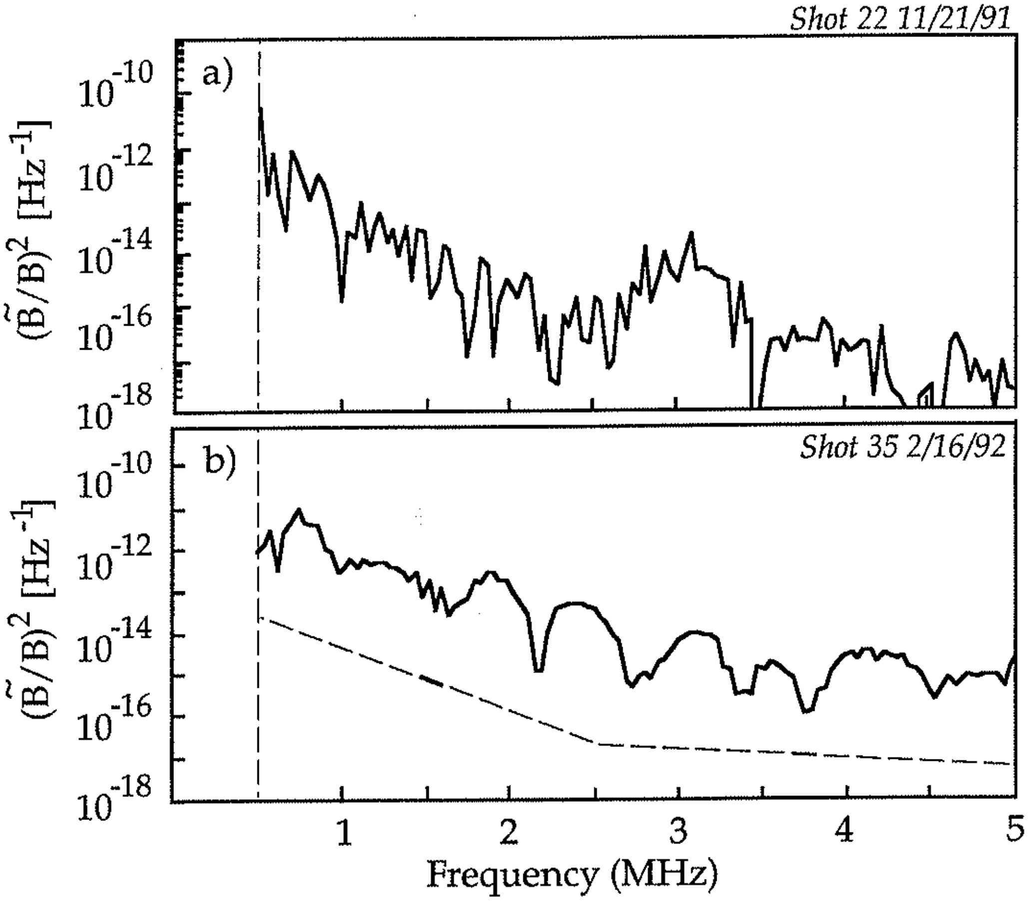

Figure 7.4.1 *Sample power spectrum features seen in 0.5-5.0 MHz magnetic fluctuations. Vertical line is the 0.5 MHz amplifier cutoff and the dotted line in (b) is the measured noise level.*

Dynamo bursts typically last 1 ms and the accompanying high frequency fluctuations last approximately .25 ms. Using 12.8 μs data records to obtain the best time resolution, the evolution of the power spectrum was examined for over 100 unsaturated dynamo bursts. A single dynamo burst and the corresponding change in ion temperature for a 360 kA discharge is shown in figure 7.4.2, along with the power spectra for the times indicated.

Note that the slope of the power spectrum in frame (ii) changes at approximately 2.6 MHz. This feature is often, but not always, seen in the data record analyzed near the peak of the ion temperature. Why this feature is not seen every time is unclear. It is usually seen in the largest amplitude fluctuation measurements. Unfortunately, the majority of the largest amplitude high frequency bursts saturate the digitizer and cannot be studied. It may be that only the strongest bursts retain information about core activity by the time they reach the MST edge. The weaker bursts may have their structure "washed out" before reaching the edge. This hypothesis could be tested by measuring the frequency spectrum of the high frequency toroidal magnetic field fluctuations at different radii. The proposed motional Stark effect diagnostic for MST[15] would be ideal for this investigation, if it has the necessary frequency response. Another explanation for the irreproducibility of the slope change feature might be that only the larger amplitude bursts have enough signal at the higher frequencies for the feature to be resolvable. At the expense of the lower frequency information, an amplifier with a narrower filter and more gain could be used to examine the frequency range of 2-4 MHz in more detail.

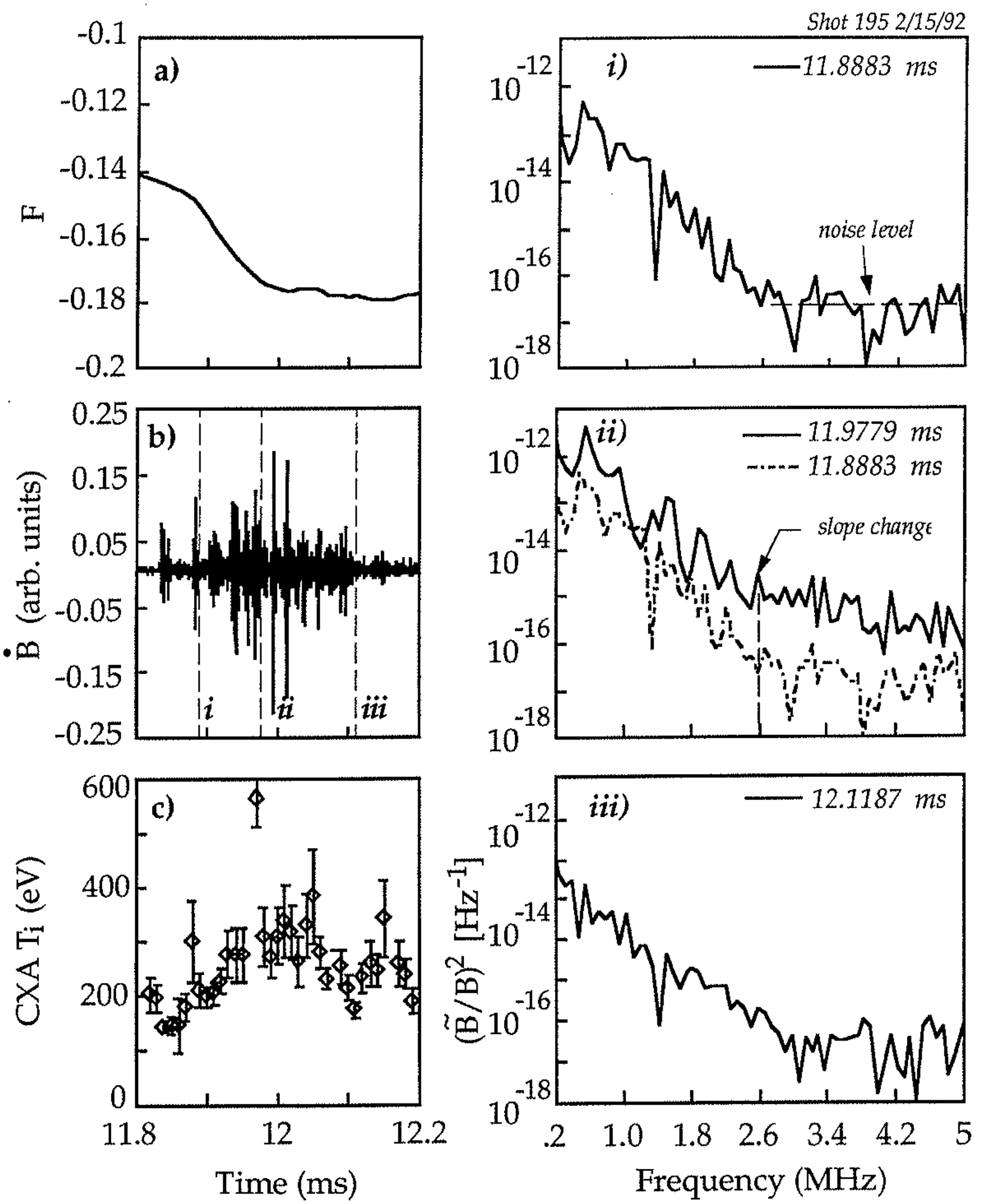

Figure 7.4.2 *a) Reversal parameter F during a dynamo burst b) high frequency magnetic fluctuations and c) charge exchange ion temperature during the same burst. i)- iii) Frequency spectrum of the high frequency magnetic fluctuations before, during, and after the dynamo burst. Change in slope feature indicated in frame (ii).*

The relationship between fluctuations in the edge of the RFP and activity in the core is not well understood. There is no *a priori* justification for comparing the spectral evolution of edge magnetic fluctuations to central ion temperatures. The clear correlation of the high frequency edge magnetic field bursts with the central ion temperature bursts is the only experimental evidence that links core and edge activity in the RFP.

Of the four frequencies plotted in figure 7.3.1, only the ion cyclotron frequency occurs near 2.5 MHz. The ion cyclotron frequency versus radius for three plasma currents in MST is plotted in figure 7.4.3. The total magnetic field needed for the cyclotron frequency determination was calculated using the Polynomial Function Model (PFM)[16] and the measured parameters F, Θ, and $B_t(r=a)$. For the 360 kAmp case, the ion cyclotron frequency decreases from 3.8 MHz on axis to 2.2 MHz at the plasma edge.

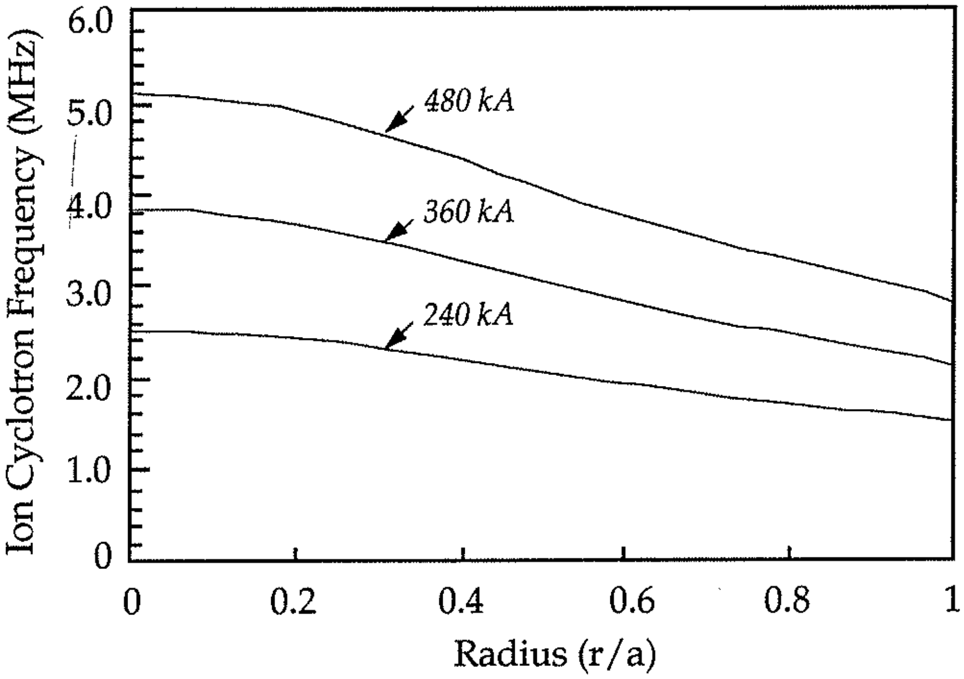

Figure 7.4.3 *Ion cyclotron frequency versus radius for different plasma currents in the MST.*

To investigate whether the frequency spectrum feature is a ion cyclotron feature, the fluctuations were measured while varying the plasma current and multiple shots ensemble averaged. The bursts used in each ensemble are as similar as possible, and the results of the analysis are displayed in figure 7.4.4.

The current scan results indicate a clear dependence of the frequency at which the power spectrum slope changes on the total edge magnetic field (Fig. 7.4.5). This analysis strongly supports the hypothesis that the slope change frequency is an ion cyclotron feature.

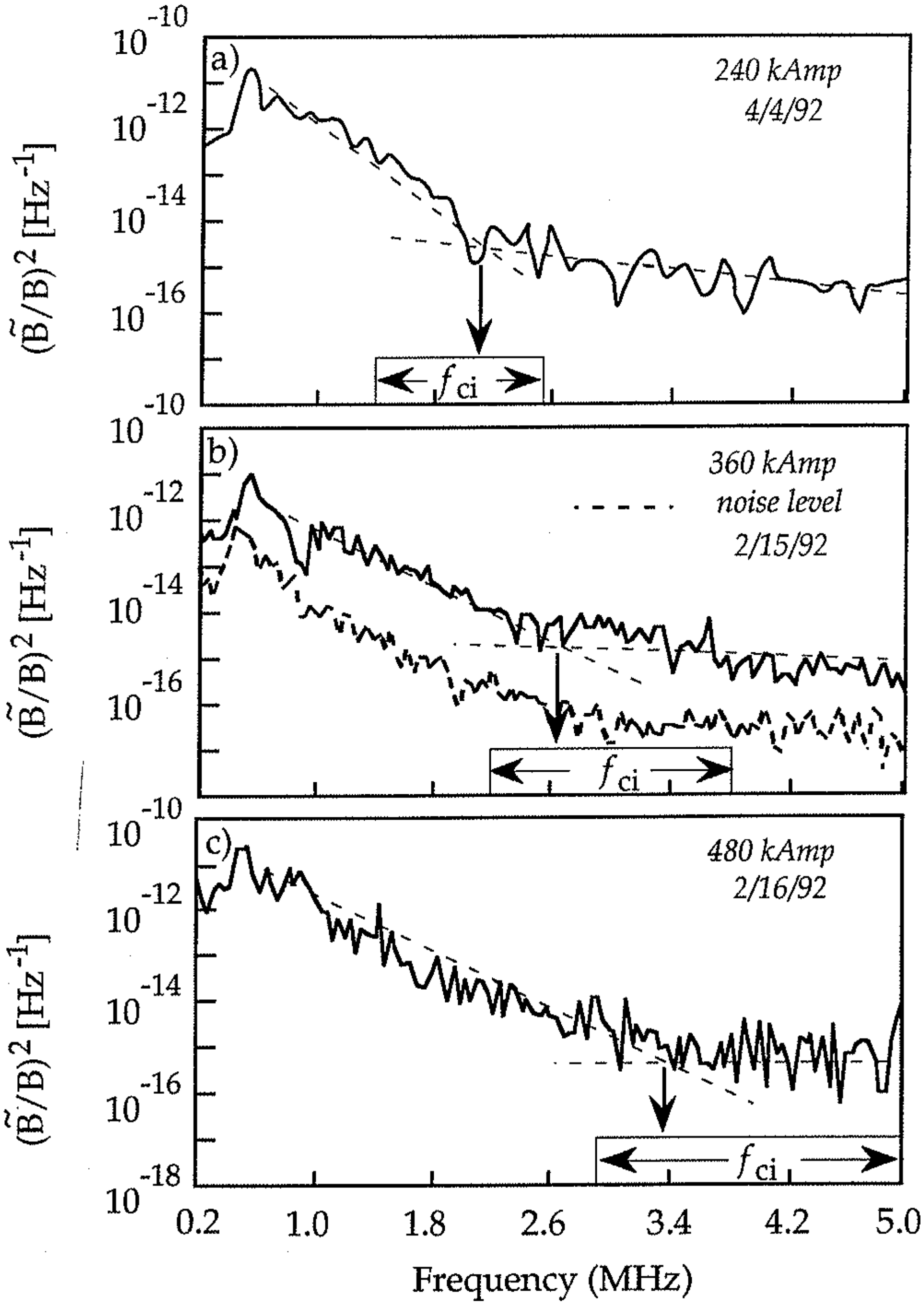

Figure 7.4.4 *Ensemble averaged frequency spectrum with dissipation feature for a) 240 kA discharges - 128 point records b) 360 kA discharges - 256 point records. c) 450 kA discharge- 256 point records.* ***Location of the slope change feature determined from the second derivative of the data after 5 point smoothing.***

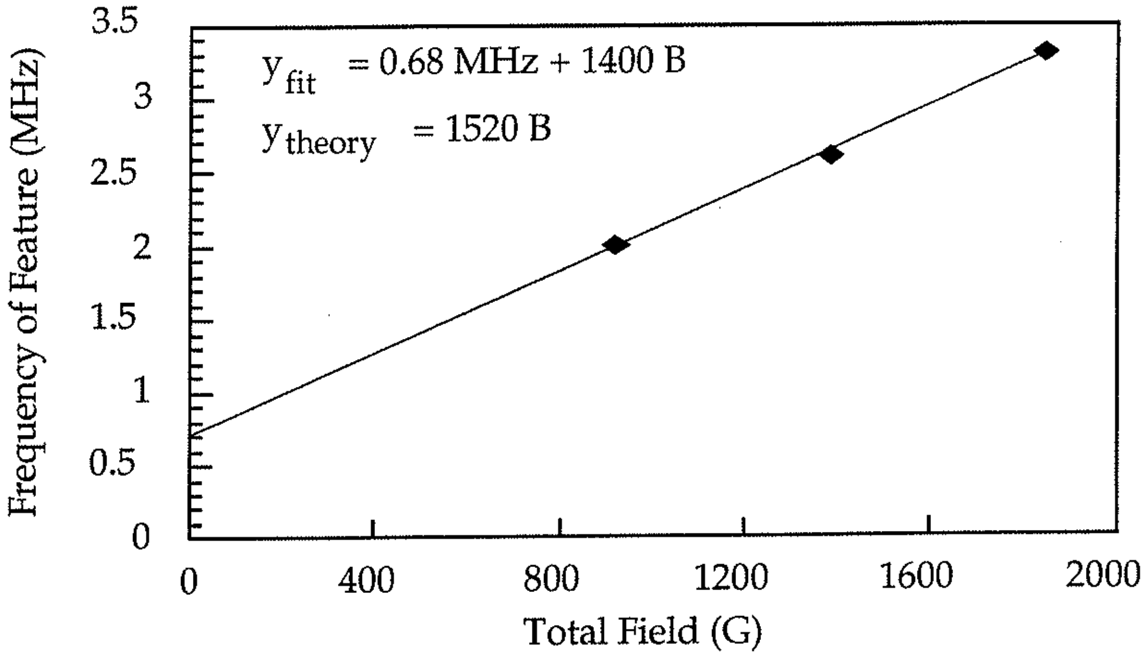

Figure 7.4.5 *Frequency of slope change power spectrum feature versus total edge magnetic field. The fit has an offset of 0.68 MHz and the slope of the linear fit is within 10% of the expected value for a ion cyclotron frequency feature.*

7.5 Dissipation of fluctuation energy in the RFP.

The distinctive change in slope of the power spectrum at a particular frequency is not well understood. In an inertial range cascade, the slope of the power spectrum is determined by a balance between the rate at which energy flows through the spectrum and the energy transfer rate to the smaller scale modes. At scales where dissipative effects are important (a non-inertial range), the power is expected to decrease rapidly to zero. When the slope of the measured spectrum does change, the power does not completely vanish (Fig. 7.4.4). If a dissipative effect does not absorb all of the available energy, a change in slope might result if the rate at which the remaining energy flows through the rest of the spectrum differs from the original rate.[17] The dominant processes for energy dissipation by ions are: ion cyclotron resonances, ion viscosity, and ion Landau damping.[18,19] Two of these, ion cyclotron resonances and ion viscosity, were the subject of a recent theoretical investigation into ion heating in the RFP.[18,19]

The refreshingly general and physical nature of the work described in reference 18 is an excellent starting point for a discussion of the energy flow in a RFP. The flow chart of figure 7.5.1 is adapted from reference 18 and shows the essential energy paths in the RFP. The energy originating in the inductive drive (IV_{loop}) encounters at least three branching points, labeled A, B, and C in figure 7.5.1.[18] Mattor, et. al. (hereafter referred to simply as Mattor) have calculated the branching ratio for the energy at each step and found that for step B,[18]

$$\frac{\varepsilon^{forward}}{\varepsilon^{inverse}} = \frac{\varepsilon}{\varepsilon^{inverse}} - 1 = \frac{E_{1,n}K_{0,0}}{E_{0,0}K_{1,n}},$$

where ε is the portion of the input energy that does not go to the equilibrium field generation. $\varepsilon^{inverse}$ is the portion of ε that cascades back into the equilibrium via the dynamo and $\varepsilon^{forward} = \varepsilon - \varepsilon^{inverse}$. This calculation assumes that all of the helicity flowing into the m=1 modes, $K_{1,n}$, inverse cascades to the equilibrium, $K_{0,0}$. The inverses helicity cascade carries a minimum of energy back to the equilibrium, the rest of the energy forward cascades to the higher m, smaller scale, modes.[18] After some additional

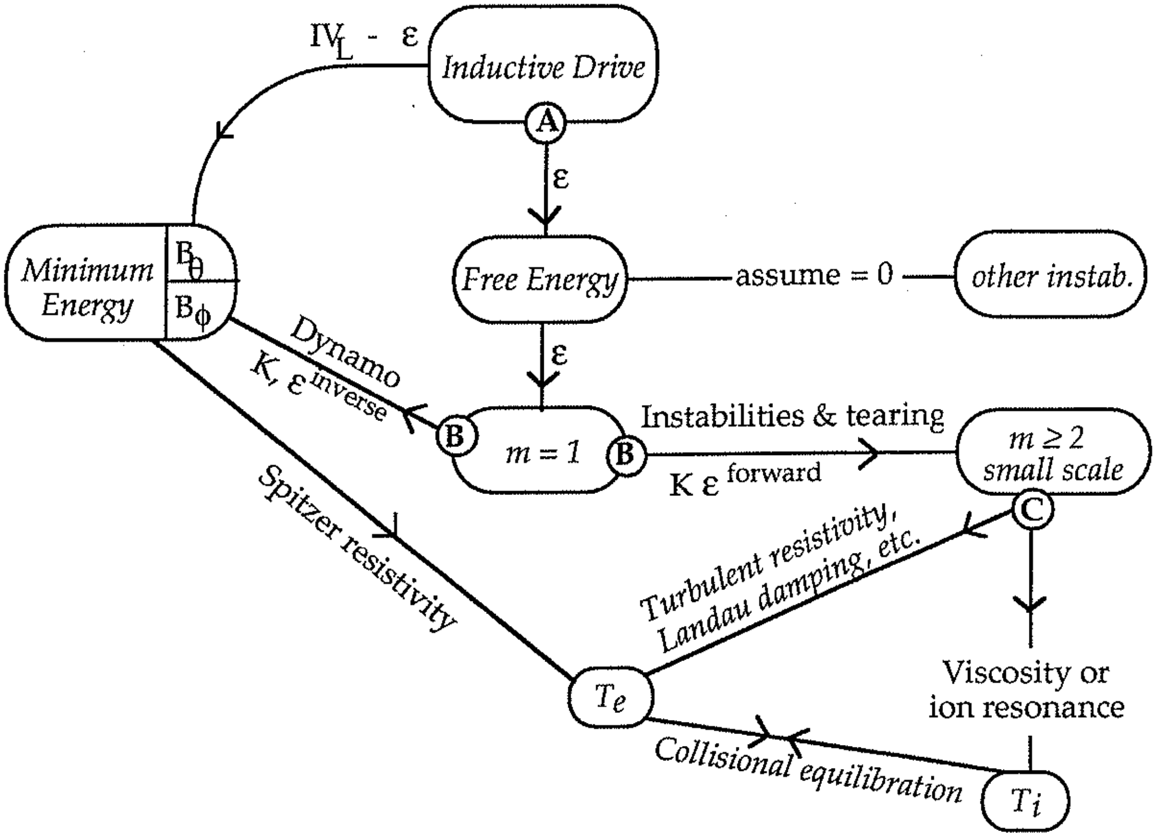

Figure 7.5.1 *Energy and helicity flows in an RFP.*[18]

assumptions about the equilibrium field structure of the RFP, Mattor arrives at an analytical expression for the cascade ratio for tearing modes,

$$\frac{\varepsilon^{\text{forward}}}{\varepsilon^{\text{inverse}}} = \frac{-2\pi\Delta'^{(0)}\left[(\psi_k^{(0)})^2 H\right]_{r_s}}{\mu K_k^{(0)}} ,$$

where Δ' is the jump derivative across the rational surface, ψ is the radial portion of the perturbed magnetic field, K_k is the helicity per unit length of the k^{th} mode, H is a simple function of the mode numbers, and μ is the normalized equilibrium parallel current.[18] This expression can be numerically evaluated for specific perturbed magnetic field profiles. A crude picture of the energy cascade through different scales based on this type of model is shown in figure 7.5.2.[19]

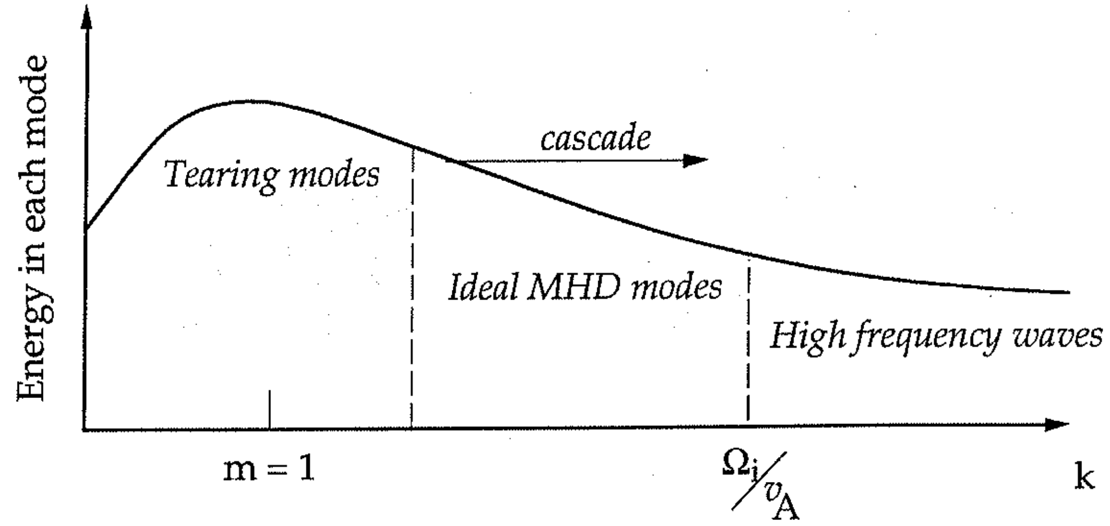

Figure 7.5.2 *Energy stored in modes, from reference 19.*

The cascade of energy to smaller scales (from m=1 to m ≥ 2) during the dynamo bursts at the same time equilibrium toroidal magnetic field is generated has been confirmed experimentally. Using the internal magnetic coil array described in chapter 4, the mode spectrum of the magnetic field fluctuations in the range 1-250 kHz was studied before, after and during the dynamo bursts. A bispectral analysis determined that the dynamo generated toroidal magnetic field is dominated by m=1,n=5,6,7 tearing modes that nonlinearly couple during the crash phase of the dynamo burst, generating modes with mode numbers in excess of n=30 and m ≥ 2 (Fig. 7.5.2).[11] This indicates that the energy stored in the magnetic fluctuations shifts from the larger scale n ~ 6 (l ~ 150 cm), to the smaller scale n ≥ 32 ($l \leq 29$ cm) modes during the crash of the dynamo burst.

The correlation of the dynamo bursts and the increases in the ion temperature certainly suggests that the energy cascading through the magnetic fluctuation ends up as ion thermal energy. The energy branching ratios at "C" in figure 7.5.1 determine how much of the cascade energy will end up in the ions, and how much in the electrons. As with neutral fluid turbulence, the energy will cascade to higher wavenumber, k, (and frequency) until dissipative effects become important.[18]

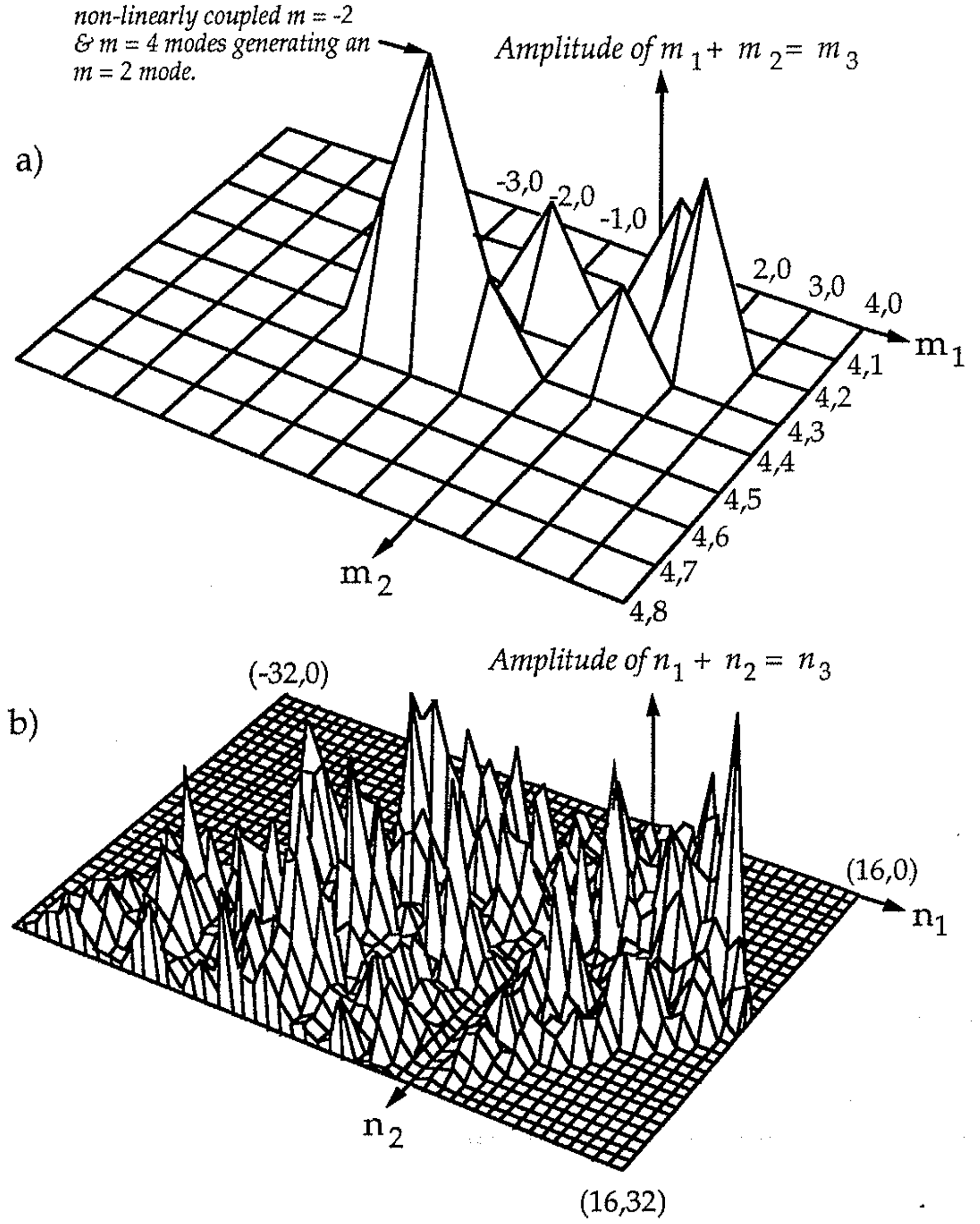

Figure 7.5.3 *Bispectral analysis of the magnetic field structure in the MST during a dynamo burst crash showing nonlinear generation of* $m \geq 2$ *and* $n \geq 20$ *modes: a) poloidal, m, modes, b) toroidal, n, modes. Before the crash, the mode spectrum is dominated by m=0,1 and n=5,6,7 modes.*[11]

7.5.1 Ion viscosity as an ion heating mechanism.

The most common explanation for the high ion temperatures of the RFP has been the viscous damping of fluctuations.[8,9,10,20,21,22] The fraction of the forward cascade energy dissipated by ion viscosity is calculated in reference 18 and found to be much smaller than the dissipation due to ion cyclotron resonances. This result contradicts those calculations which find viscosity to be a sufficient source of ion heating in the RFP.[8,9,10,20,21,22] Mattor's calculations show that ion viscosity effects occur at much smaller scales than ion cyclotron resonance (ICR) effects. Therefore, the forward cascade energy will damp to the ions by ICR long before viscous effects become important.

Simply put, viscosity is the parameter that describes the momentum transfer perpendicular to a flow in a fluid. In a thermally equilibrated fluid the ions have a much larger momentum than electrons and therefore ion viscosity plays a larger physical role in hot plasmas than electron viscosity. Electromagnetic and acoustic waves propagating through the plasma lose energy as momentum is transferred by the non-zero ion viscosity, converting flow energy into ion thermal energy The effective mass of the ions is dependent upon the ambient magnetic field, resulting in different parallel and perpendicular viscosities.

Often the energy stored in MHD fluctuations dissipated by ion viscosity is calculated using a isotropic flow velocity fluctuation level, a large parallel ion viscosity, and an estimated scale length,[19]

$$P_{\text{vis}} = \nu_{/\!/} \frac{\tilde{v}^2}{L^2},$$

where $\tilde{v}$ is the flow velocity fluctuation and L the scale length. The error in using this approach is pointed out in reference 18; *parallel flow velocity fluctuations* must be used with a parallel viscosity, and they are quite small for MHD activity. This can be see from the parallel momentum equation:

$$\vec{B} \cdot \frac{d\vec{v}}{dt} = \vec{B} \cdot \left[\frac{\vec{J} \times \vec{B}}{\rho_o c} + \frac{\nabla P}{\rho_o} + (\text{damping}) \right].$$

For $\vec{J}_0 = \lambda \vec{B}_0$ (often assumed for low β RFP's) all of the linear and nonlinear terms involving $\vec{J} \times \vec{B}$ vanish. The parallel pressure gradient term is negligible due to the weak parallel density and temperature gradients of a hot magnetized plasma. Thus parallel flow velocity fluctuations are not strongly driven by MHD modes. When the much smaller perpendicular viscosity is used in these simple calculations, the dissipated energy is quite small.

A more self-consistent approach is to calculate the fraction of the forward cascade energy dissipated by the perpendicular viscosity. The perpendicular viscous energy dissipation rate is a strong function of the scale of the fluctuations:

$$\frac{d\vec{v}_\perp^2}{dt} = \mathbf{V}_\perp \vec{v} \cdot \nabla^2 \vec{v}$$

is equivalent to

$$\frac{dE_\perp}{dt} \approx 2\mathbf{V}_\perp k^2 E_k \,.$$

For an MHD inertial range $E_k = E_{magnetic} = E_{total}/2$,[18] which gives

$$\gamma^{visc} = \text{dissipation rate} = \mathbf{V}_\perp k^2.$$

The Braginskii perpendicular ion viscosity is given by,[23]

$$\mathbf{V}_\perp = .3nkT_i/(\omega_{ci}^2\, \tau_i).$$

When the viscous dissipation rate is larger than the eddy turnover rate,

$$1/\tau = 1/(v_A/k\,\varepsilon)^{1/2},$$

(where, $v_A = B/\sqrt{4\pi n_i m_i}$, and ε is the power flowing through the spectrum [Energy/time]), ion viscosity becomes a significant energy loss mechanism.[24] This relationship determines at what scale viscosity is an important effect. Using the MST parameters for v_A = Alfvén velocity = $\sqrt{B^2/2\rho}$, ε, T_i = ion temperature, ω_{ci} = cyclotron frequency, n = plasma density, and τ_i = ion-ion collision time,

$$\frac{k_{\omega_{ci}}}{k_{v_\perp}} = \frac{\lambda_{v_\perp}}{\lambda_{\omega_{ci}}} \approx 0.03 .$$

Perpendicular viscosity effects become important at much ***smaller*** scales than ion cyclotron resonance effects. The energy would have to cascade past the ion cyclotron resonance region to reach the viscous dissipation region.

7.5.2 Ion cyclotron resonances as an ion heating mechanism.

The structure of the magnetic fluctuation power spectrum during peak ion heating encourages the hypothesis that ion cyclotron resonances are responsible for the energy transfer from the fluctuations to the ions. The resonance occurs when the frequency of the fluctuations is at a harmonic of the cyclotron frequency of the ions. The scale at which this occurs has already been shown to be much larger than the relevant viscosity scale.

Ion cyclotron resonances are fundamentally different from other dissipation mechanisms. The energy transfer cannot be written as a dissipation rate. If the fluctuations are Alfvén waves ($\tilde{k} \parallel \tilde{B}$),[25] a cyclotron resonance will absorb all of the energy that reaches the ICR scale. If they are magnetosonic waves ($\tilde{k} \perp \tilde{B}$), they continually exchange energy with Alfvén waves in a turbulent cascade and all the energy is still absorbed.[25] For MST parameters, only the general magnetosonic and Alfvén wave dispersion functions yield non-imaginary solutions for k at $\omega \approx 1.0$ MHz.[26] At the ICR scale ($k = \Omega_i / v_A$), the viscous energy dissipation can be compared to the energy absorbed by ICR effects.

Assuming all of the excess input energy (see section 5.4) flows into the m=1 modes and then forward cascades,

$$\varepsilon^{\text{forward}} = \frac{I V_L^{\text{anom}}}{n_0 m 2\pi^2 R a^2},$$

the viscous dissipation relative to the ICR absorption at the ICR scale is:

$$\frac{\varepsilon_{\nu_\perp}}{\varepsilon}\left(k=\frac{\omega_{ci}}{v_A}\right) = \frac{\nu_\perp {\omega_{ci}}^{3/2}}{v_A \varepsilon^{1/2}} \approx 5 \times 10^{-3}.$$

This calculation assumes the same perpendicular flow velocity fluctuation used in reference 18,

$$v_\perp \approx (v_A \varepsilon)^{1/2} k^{-3/2}.$$

Other parameters used are:

$a = 50$ cm
$T_e \approx T_i = 200$ eV
$n_o \approx 10^{13}$ cm^{-3}
$I = 500$ kAmp
$v_A = 6.9 \times 10^7$ cm/s
$\nu_\perp = 6.2 \times 10^3$ cm^2/sec

$R = 150$ cm
$B_o = 1000$ G
V_L^{anom} = excess voltage ≈ 7 V
$\Omega_i = 9.6 \times 10^6$ rad/sec
$\tau_i = 2 \times 10^{-4}$ sec
$\varepsilon^{forward} = 3.0 \times 10^{17}$ cm^2/sec^3

Therefore, the forward cascade energy will encounter a negligible amount of viscous dissipation before being heavily damped by the ion cyclotron resonance.

7.6 Predicted magnetic fluctuation amplitudes and ion temperatures.

Under the assumption that all of the excess input energy flows into the forward cascade, Mattor has calculated a ideal fluctuation power spectrum using Kraichman's MHD turbulence model.[19,24] He calculates the fluctuation spectral amplitude, $(\tilde{B}/B)^2$, at 1 MHz to be on the order of 8×10^{-8} Hz^{-1}. The measured amplitude is roughly 5×10^{-12} Hz^{-1}. Because of the stringent and somewhat unphysical assumptions of this model, there are many possible explanations for the discrepancy. If the fluctuations are being damped by ICR effects, the amplitude near f_{ci} *should* be much lower than expected for an ideal cascade. The fluctuations are measured at the plasma edge - is this a physically relevant location to measure them? Damping of the fluctuations via electron Landau damping and other electron effects has also been ignored.

If all of the excess input energy goes into ion heating during the dynamo bursts, and the transfer time is much faster than the ion energy confinement time, the expected ion temperature change for the ensemble averaged dynamo burst of figure 7.2.1 can be estimated:

$$\int_0^{\Delta t} IV_L^{anom} dt = \Delta \int \frac{3}{2} n_i T_i dV ,$$

$$\int_0^{\Delta t} IV_L^{anom} dt = \frac{3}{2} \Delta (n_{io} T_{io}) \, V \, f ,$$

where V is the volume of the MST and f accounts for the integral over the assumed density and temperature profiles (f = 1 if both profiles are flat and f = 1/3 if both profiles are parabolic). Solving for the stored ion energy change,

$$\Delta(n_{io} T_{io}) = \frac{\frac{2}{3}\int_0^{\Delta t} IV_L^{anom} dt}{V f} ,$$

using the same assumptions for the Thomson scattering measured central electron density at 10 ms as used in chapter 5, and assuming quasi-neutrality, the expected ion temperature at the peak of the ensemble averaged dynamo burst of figure 7.2.1 is given by,

$$(T_{io})_{peak} = 250 \text{ eV} + \frac{41 \text{ eV}}{f} .$$

The peak ion temperature in figure 7.2.1 is 320 eV, resulting in a very reasonable profile factor of f = 0.6. As this calculation assumed that ***all*** of the excess energy goes into ion heating, it is likely that the true profiles are more peaked than f = 0.6 implies . If some of the excess energy does not end up in the ions, a smaller f (a more peaked profile) would be required to match the calculations of this model with the measured ion temperatures.

References

[1] E. J. Caramana, R. A. Nebel, and D. D. Schnack, *'Nonlinear, single-helicity magnetic reconnection in the reversed-field pinch,'* Phys. Fluids 26, 1305 (1983).

[2] S. R. Burns, W. A. Peebles, D. Holly, T. Lovell, *'Madison Symmetric Torus Far-Infrared Interferometer,'* to be published in Rev. Sci. Instrum. October (1992).

[3] D. Forslund, R. Morse, C. Nielson, *'Theory of Turbulent Heating and Anomalous Diffusion in Pinch Plasmas,,'* in Plasma Physics and Controlled Nuclear Fusion Research (International Atomic Energy Agency, Vienna, 1971), Vol. II, 277.

[4] C. T. Dum, R. Chodura, and D. Biskamp, *'Turbulent Heating and Quenching of the Ion Sound Instability,'* Phys. Rev. Lett. **32**, 1231 (1974).

[5] B. D. Fried, et. al., *'Turbulent Resistivity, Diffusion and Heating,'* in Plasma Physics and Controlled Nuclear Fusion Research (International Atomic Energy Agency, Vienna, 1971), Vol. II, 55.

[6] P. L. Similon and P. H. Diamond, *'Nonlinear interaction of toroidicity-induced drift modes,'* Phys. Fluids **27**, 916 (1984).

[7] Robert B. Howell, and Yoshio Nagayama,*' Ion energy measurements on a reversed-field pinch experiment using Doppler broadening,'* Phys. Fluids **28**, 734 (1985).

[8] Z. Yoshida, *'Direct Ion Heating Through MHD Relaxation,'* Nucl. Fusion **31**, 386 (1991).

[9] A. Lazaros, *'The Effect of the Velocity Fluctuations on the Ion and Electron Temperature and the Energy Confinement in the Reversed Field Pinch,'* Plasma Phys. and Contr. Fusion **31**, 1995 (1989).

[10] C. G. Gimblett, *'Ion Heating Due to Parallel Viscosity,'* Europhys. Lett. **11**, 541 (1990).

[11] Saeed Assadi, Ph. D. Thesis, University of Wisconsin - Madison, in progress.

[12] Nathan Mattor, private communication.

[13] William H. Press, Brian P. Flannery, Saul A. Teukolsky, and William T. Vetterling, Numerical Recipes - The Art of Scientific Computing (Cambridge University Press, New York, 1986) pp. 425.

[14] Interactive Data Language, Research Systems, Inc. , 777 25th St. Suite 302, Boulder, Colorado 80303 (1988).

[15] Daniel Den Hartog, private communication.

[16] J. C. Sprott, *'Polynomial Function Model for Reversed Field Pinches,'* Phys. Fluids **31**, 2266 (1988).

[17] Paul Terry, private communication.

[18] N. Mattor, P. Terry, and S. C. Prager, submitted to Phys. Rev. Lett.

[19] Nathan Mattor, unpublished calculations.

[20] P. Martin, S. Ortolani, and A. Rossi, *'Plasma Heating and Power Balance in the Reversed Field Pinch,'* in Proceedings of the International School of Plasma Physics Workshop on Alternative Confinement Schemes, Varenna, Italy, 1037 (1990).

[21] A. Fujisawa, H. Ji, K. Yamagishi, S. Shinohara, H. Toyama, K. Miyamoto, *'Anomalous Ion Temperature and Plasma Resistance Due to MHD Fluctuations in Repute-1 Reversed Field Pinch Plasmas,'* Nucl. Fusion **31**, 1443 (1991).

[22] G. A. Wurden, P. G. Weber, K. F. Schoenberg, A. E. Schofield, J. A. Phillips, C. P. Munson, G. Miller, J. C. Ingraham, R. B. Howell, J. N. Downing, R. R. Chrien, T. E. Cayton, L. C. Burkhardt, R. J. Bastasz, S. E. Walker, A. M. Prezler, P. G. Carolan, and C. A. Bunting, *'Ion heating studies in the ZT-40M Reversed Field Pinch'*, in Proceedings of the 15th European Conference on Controlled Fusion and Plasma Physics, Dubrovnik (European Physical Society, 1988), 533.

[23] David L. Book, NRL Plasma Formulary, (Naval Research Laboratory, Washington D.C., 1987) pp. 31-34.

[24] R. H. Kraichnan, *'Inertial-Range Spectrum of Hydromagnetic Turbulence,'* Phys. Fluids **8** 1385, (1965).

[25] A. G. Sitenko, Electromagnetic Fluctuations in Plasmas, translated by M. D. Friedman (Academic Press, New York 1967), pp. 110-118.

[26] F. F. Chen, Introduction to Plasma Physics and Controlled Fusion (Plenum Press, New York 1984) pp. 145.

CHAPTER 8

CONCLUSIONS, COMMENTS, AND SUGGESTIONS FOR FURTHER WORK

No longer must a correlation between dynamo activity and high ion temperatures in the RFP be assumed. The experiments described in this thesis provide overwhelming evidence that these two characteristics of the reversed field pinch are closely coupled. The equilibrium ion temperature has been shown to be unexplainable by simple ion-electron collisional heating. The fluctuating ion and electron temperatures confirm the lack of collisional coupling between the ions and electrons in the RFP. The correlation of the ion temperature and dynamo fluctuations suggests that a fluctuation dissipation mechanism is responsible for the bulk of the ion heating in the RFP and the frequency spectrum of the high frequency magnetic fluctuations indicates enhanced energy dissipation near the ion cyclotron frequency.

Considerable progress has been made in understanding the nature of the energy transfer mechanisms from fluctuations to ions in a RFP, and recent theoretical studies[1] have finally begun to examine the ion heating question in terms of the total energy budget of the RFP. Measurements of the total energy budget of the RFP may very well be the best way to fully understand anomalous ion heating and determine if the ions obtain their energy from the fluctuations. These measurements would have to include full profile measurements of the temperatures, densities, and fluctuations in the RFP. Of course, it is not likely that the facilities to make such measurements will exist on the MST in the near future and a more realistic set of possible measurements is discussed at the end of this chapter.

8.1 Anomalous electron heating?

In almost all discussions of RFP's the measured plasma resistance of a RFP discharge is compared to a Spitzer resistivity based on the measured electron temperature, density, and effective proton number (Z_{eff}),[2]

$$\eta_\perp = \frac{Z_{eff}\, 1.03 \times 10^{-2}\, \ln\Lambda}{T^{3/2}}\, \Omega\,\mathrm{cm}\,.$$

The measured resistance is always much larger than the Spitzer resistance and the point is often made that the excess input energy is lost in the RFP, giving the RFP the reputation of an energy inefficient device. It has been shown in this thesis that at least part of the excess energy goes into ion heating -- an unexpected benefit from an Ohmically heated device. The remaining energy, if any, may still go into electron heating. One aspect of Mattor's work[1] not mentioned in chapter 7 was that the calculated dissipation of fluctuations by the electrons via electron Landau damping is of the same magnitude as the ion cyclotron dissipation by the ions. This implies that the electrons in the RFP may be heated as strongly by non-Ohmic effects as by collisional, Ohmic, effects. Spitzer resistivities calculated from electron temperatures due to such effects would not accurately reflect the flow of energy into the electrons. The lack of an electron temperature increase during the dynamo bursts (Fig. 7.2.1) appears to contradict the electron Landau damping hypothesis. A possible explanation for the lack of an electron temperature increase is that the electron transport may also increase during a dynamo burst, negating the effect of the additional heating. Of course, the same argument can be used for the ions, yet they do heat up.

In other words, for a given Ohmic resistance in a RFP discharge, the electrons are heated much more than expected. That RFP Ohmic resistivities are excessive cannot be ignored, but if the resistivity is dominated by turbulence effects, comparisons with the Spitzer resistivity may not be appropriate. Calculations for turbulent resistivities are plentiful[2] and most scale strongly with fluctuation amplitude. Perhaps a tearing mode resistivity could be calculated and compared to measured MST resistivities.

8.2 Suggestions for further experiments.

The five channel charge exchange analyzer constructed for these experiments satisfied all of its operational goals: fast time response, absolute calibration, and reliable operation. However, many experiments involving global parameter scaling remain incomplete. These experiments are **crucial** if any progress is to made in understanding the final distribution of energy in the RFP. There can be no substitute for controlled and well diagnosed experiments.

The form of the energy cascade in wavenumber, k space, is still unknown over a broad frequency range. Thorough measurements in the frequency range 1 - 250 kHz have provided extremely useful information about the dynamo bursts.[3] Further measurements of the k spectrum for fluctuations up to 5 MHz and down to the ion gyroradius scale, ~ 1 cm, could easily provide a conclusive indentification of the ion heating mechanism. Similar measurements were carried out on the Tokapole device[4] and most of the equipment still exists; the magnetic probes would have to be hardened to survive in the MST.

Another unanswered question is the similarity of proton and carbon temperatures in the MST. Many RFP's have reported impurity ion temperatures much greater than hydrogen temperatures, yet the impurity temperature is often lower than the hydrogen temperature in the MST (Fig. 5.2.4). It has been assumed that this is an electron temperature profile effect in the MST, but what makes MST different from the other devices ? Could flatter density profiles in those other devices artificially lower the effective charge exchange ion temperature (see section 3.1) ? An impurity ion temperature profile might shed some light (pun intended) on this question.

The swiveling feature of the charge exchange analyzer has yet to be used to measure the ion temperature profile. The current single point Thomson scattering diagnostic can be moved to (r/a) = 0.6 and, if used in conjunction with the charge exchange analyzer, a rough measurement of the plasma pressure profile might be obtained.

These are just a few of the fundamental experiments that can be attempted with the current complement of MST diagnostics. The quest for an understanding of the physics of RFP plasmas is just beginning !

References

[1] N. Mattor, P. Terry, and S. C. Prager, submitted to Phys. Rev. Lett.

[2] David L. Book, NRL Plasma Formulary, (Naval Research Laboratory, Washington D.C., 1987) pp. 29.

[3] Saeed Assadi, Ph. D. Thesis, University of Wisconsin - Madison, in progress.

[4] E. J. Haines, *'Measurement of Magnetic Fluctuations at the Small Spatial Scales in the Tokapole II Tokamak,'* Ph. D. Thesis, University of Wisconsin-Madison (1991).